



Deliverable D3.31

Converter designs tailored to SC and PDD concepts

Aalborg University (AAU), Denmark

Leibniz University Hannover (LUH), Germany

University of Strathclyde (USTRAT), United Kingdom

Agreement n.:	308974
Duration	November 2012 – October 2017
Co-ordinator:	DTU Wind



The research leading to these results has received funding from the European Community's Seventh Framework Programme FP7-ENERGY-2012-1-2STAGE under grant agreement No. 308974 (INNWIND.EU).

PROPRIETARY RIGHTS STATEMENT

This document contains information, which is proprietary to the "INNWIND.EU" Consortium. Neither this document nor the information contained herein shall be used, duplicated or communicated by any means to any third party, in whole or in parts, except with prior written consent of the "INNWIND.EU" consortium.

Document information

Document Name:	Converter Designs tailored to SC and PDD concepts
Document Number:	Deliverable D 3.31
Author:	Dr. Fujin Deng, Prof. Zhe Chen, Aalborg University (AAU), Denmark, Mr. Dennis Karwatzki, Prof. Dr. -Ing. Axel Mertens, Leibniz University Hannover (LUH), Germany, Dr. Max Parker, Prof. Stephen Finney, University of Strathclyde (USTRAT), United Kingdom
Document Type	Report
Dissemination level	PU
Review:	Henk Polinder and Asger Bech Abrahamsen
Date:	2015/8/31
WP:	WP 3
Task:	Task 3.3
Approval:	Approved by WP Leader

Preface

This report is prepared for Deliverable D3.31 “Converter Design tailored to SC and PDD concepts” of the Task 3.3 Power Electronics in the WP 3 “Electro-Mechanical Conversion” of EU INNWIND project (FP7 “Innovative Wind Conversion System (10-20 MW) for Offshore Applications”).

The members of Task 3.3 Power Electronics team include:

Dr. Fujin Deng, Prof. Zhe Chen, Aalborg University (AAU), Denmark; Mr Dennis Karwatzki, Prof., Dr.-Ing. Axel Mertens, Leibniz University Hannover (LUH), Germany; Dr. Max Parker, Prof. Stephen Finney, University of Strathclyde (USTRAT), United Kingdom.

The contributions to the project report are made by the following chapters:

- 1) Introduction: AAU, LUH, and USTRAT
- 2) Voltage Source Converter Design Tailored to SCG: AAU
- 3) Voltage Source Converter Design Tailored to PDDG: LUH
- 4) Current Source Converter Design Tailored to SCG AND PDDG: USTRAT
- 5) Conclusions: AAU, LUH, and USTRAT

The Task 3.3 Power Electronics team wishes to thank Henk Polinder, Asger Bech Abrahamsen, other WP3 colleagues and partners of EU INNWIND, for their contributions of discussions, suggestions, comments and, data collection.

TABLE OF CONTENTS

1	INTRODUCTION.....	6
1.1	Introduction	6
1.2	Performance index for evaluation and energy capture calculation.....	7
1.3	Design specifications, power converter topologies and segmented generators.....	7
1.4	References.....	9
2	VOLTAGE SOURCE CONVERTER DESIGN TAILORED TO SCG.....	10
2.1	Introduction	10
2.2	Voltage Source Converter Topologies for SCG.....	10
2.2.1	Power Converter Type I for SCG based on Non-segmented Generator.....	10
2.2.2	Power Converter Type II for SCG based on 4-Segmented Generator.....	11
2.3	Costs	11
2.3.1	Semiconductors Costs	11
2.3.2	Passive Components Costs	15
2.3.3	Cooling System Costs.....	17
2.3.4	Conclusions	18
2.4	Size and Weight.....	19
2.4.1	Converter Size	19
2.4.2	Converter Weight.....	20
2.5	Efficiency, Energy Capture and Wind Energy Cost.....	21
2.5.1	Efficiency for 10 MW Power Converters.....	22
2.5.2	Efficiency for 20 MW Power Converters.....	22
2.5.3	Energy Capture and Wind Energy Cost	23
2.6	Control Strategy Design	28
2.6.1	Control for Normal Operation	28
2.6.2	Fault Ride-Through Control.....	31
2.7	Simulation Studies	33
2.7.1	Case I: Under variable wind speed.....	33
2.7.2	Case II: Grid fault situation	35
2.7.3	Case III: Circulating current control.....	43
2.8	Discussion and Conclusions.....	45
2.9	Appendix	46
2.10	References.....	46
3	VOLTAGE SOURCE CONVERTER DESIGN TAILORED TO PDDG	48
3.1	Introduction	48
3.2	Topologies for the PDDG.....	48
3.3	Component Design for Neutral Pointed Clamped Converter	54
3.3.1	DC Link Capacitor Design	54
3.3.2	Semiconductor Choice.....	55

3.3.3	Grid Filter Design.....	59
3.3.4	Generator Side Inductor	62
3.4	Efficiency.....	62
3.5	Costs and CoE due to PE	64
3.6	Size and Weight.....	66
3.7	Control.....	67
3.8	Simulation.....	68
3.9	Conclusions	74
3.10	References.....	74
4	CURRENT SOURCE CONVERTER DESIGN TAILORED TO SCG AND PDDG.....	76
4.1	Introduction	76
4.2	Current Source Converters Topologies	76
4.3	Costs	79
4.3.1	Active Filter Costs.....	79
4.3.2	Semiconductor Costs	81
4.3.3	Passive Components Costs	81
4.3.4	Cooling System Costs.....	83
4.3.5	Conclusions	84
4.4	Converter Size	84
4.4.1	Active Filter	85
4.4.2	Main converter switching devices	87
4.4.3	DC-link inductors	88
4.4.4	Cooling and other ancillary systems	88
4.4.5	Overall size	88
4.5	Converter Weight.....	89
4.6	Efficiency, Energy capture and wind energy cost	92
4.7	Control Design	94
4.7.1	Control for Normal Operation – SCG.....	94
4.7.2	Control for Normal Operation – PDDG	97
4.7.3	Fault Ride-Through Control.....	97
4.7.4	Series operation of converters for segmented generators.....	99
4.8	Modelling and Simulation Studies	99
4.9	Discussion and Conclusions.....	104
4.10	References.....	106
5	CONCLUSIONS.....	107

1 INTRODUCTION

1.1 Introduction

Over the last twenty years, renewable energy sources have been attracting great attention due to the cost increase, limited reserves, and adverse environmental impact of fossil fuels. In the meantime, technological advancements, cost reduction, and governmental incentives have made some renewable energy sources more competitive. Among them, wind energy is one of the fastest growing renewable energy sources [1-1~1-9].

So far, a variety of wind power technologies have been developed, which have improved the conversion efficiency and reduced the costs for wind energy production. The size of wind turbines has increased from a few kilowatts to several megawatts each [1-1~1-3]. The most recent finding of the wind energy development is that the high-power wind turbine provides some key innovations. Larger wind turbines often result in reduced cost since their production, installation, and maintenance costs are lower than the sum of smaller wind turbines achieving the same power output [1-4~1-6]. Today, multi-MW size wind turbines are being developed and installed. The steady growth of installed wind power together with the upscaling of the wind turbine power capability has pushed the research and development of wind turbine systems, since they are converting the full power production of the turbine in contrast to classical designs where the generator is connected directly to the grid.

The Power electronic converter is an enabling technology for renewable energy power generation system, which is used to convert electrical power from one form into another so as to efficiently match the application characteristics. In the wind turbine system, the power electronic converter is used to provide the connection/conversion between the generator and the grid to achieve high efficiency and meet the grid requirements, including frequency, voltage, active and reactive power, flickers, harmonics, and ride-through capabilities, etc. On the generator side, the ideal conversion system would enable the optimal energy to be captured, reducing the system power loss and stress; on the grid side, it would convert the power into the required frequency and voltage with the desired waveform. Power electronic converters are playing an increasingly significant role in the development of modern wind turbines and wind farms [1-2~1-9].

In recent years, power electronic technology, including semiconductor devices, circuit topologies, modulation, and control methods, has been rapid developed. The performances of the power electronic converters are continuously being improved and more and more power electronics have been incorporated into wind turbine systems to improve wind turbine control and to improve the interconnection to the grid system [1-2], [1-3].

The objective of this report is to design the power electronic converters for the 10 MW and 20 MW INNWIND. EU reference wind turbines based on SC and PDD concepts, respectively. In this report, the power electronic converters will be designed based on the INNWIND EU M22 report, the designed power electronic converters will be assessed in view of costs, efficiency, size, reliability, and so on. In addition, the corresponding control for the wind turbine with the selected power electronic converters will be designed, the related grid code requirements such as fault-ride through control will be considered. The simulation studies will be conducted to show the effectiveness of the designed power electronic converters and control.

1.2 Performance index for evaluation and energy capture calculation

The power converters will be designed tailored for the 10 & 20 MW superconducting generator (SCG) and magnetic pseudo direct drive generator (PDDG). The designed power converters will be mainly evaluated with the following index,

- Cost
- Size
- Weight
- Efficiency
- Energy capture

1.3 Design specifications, power converter topologies and segmented generators

Power converters are widely used in wind energy conversion system. To date, a variety of power converters with different topologies and characteristics have been developed or studied for variable-speed wind turbine systems [1-10], [1-11]. Fig. 1-1 illustrates three types of wind energy conversion systems based on different power converter configurations. Fig. 1-1(a) shows the wind energy conversion system based on a back-to-back (BTB) voltage source converters (VSCs). Fig. 1-1(b) shows a wind turbine system based diode rectifier, current source, converter (CSC). Fig. 1-1(c) shows a wind turbine system with an AC/AC power electronic converter.

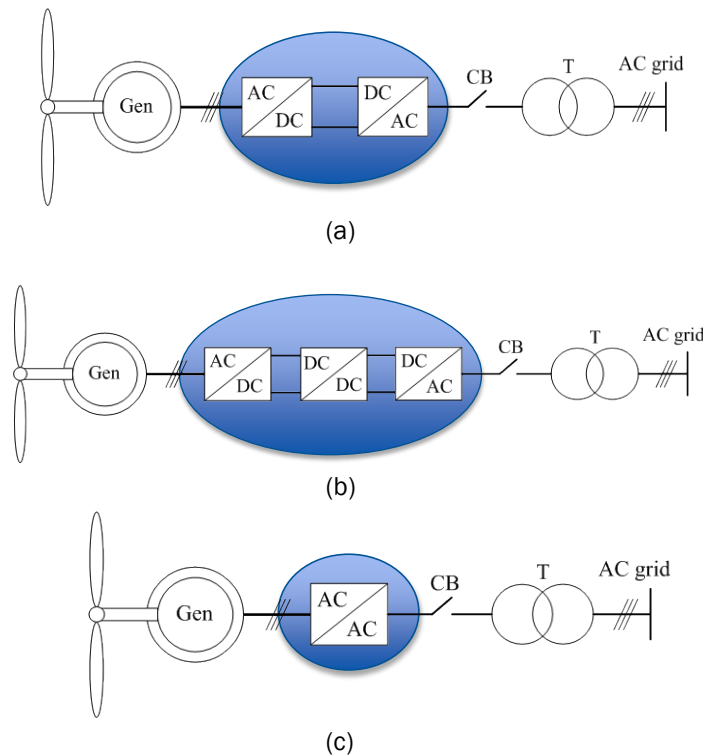


Fig. 1-1. The wind energy conversion system investigated is based on (a) Back-to-back VSC converters. (b) Current source converter. (c) AC/AC converter.

The above three power electronic converter configurations have been studied in the Deliverable D3.32 “Converter designs based on new components and modular multilevel topologies”. According to the Deliverable D3.32, several power electronic converters may be more attractive for the SC and PDD generators in 10 and 20 MW wind turbines based on single generator, their configurations are shown in Fig. 1-2. Fig. 1-2(a) shows the wind turbine based on the 3-level (3L) neutral-point clamped (NPC) back-to-back power converters, where two BTB 3L-NPC converters are connected in parallel for the generator. Fig. 1-2(b) shows the modular multilevel matrix converter (MMMC) for the generator, which is a direct AC/AC converter. Fig. 1-2(c) shows the wind turbine based on the converter configuration of current source inverter and active filters (CSI-

Actfilt). According to D3.32, these converters have better technical economic performance, therefore are selected for the study.

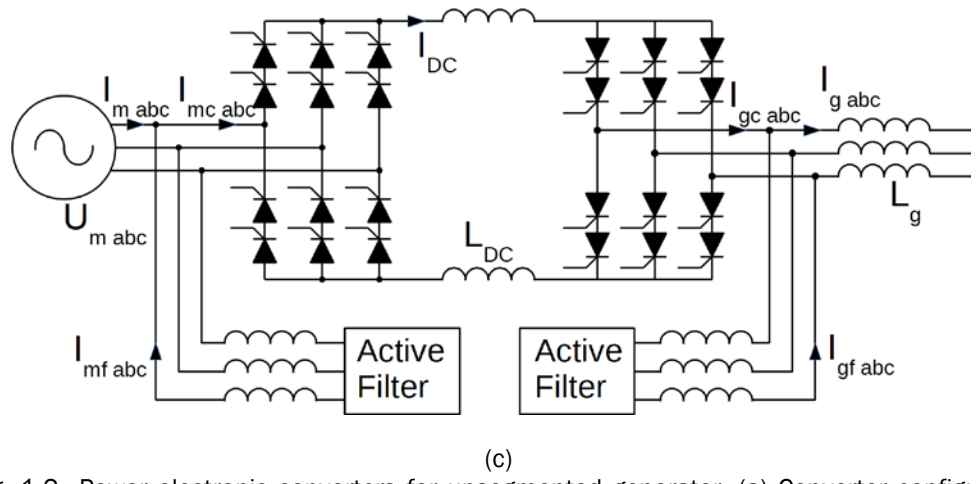
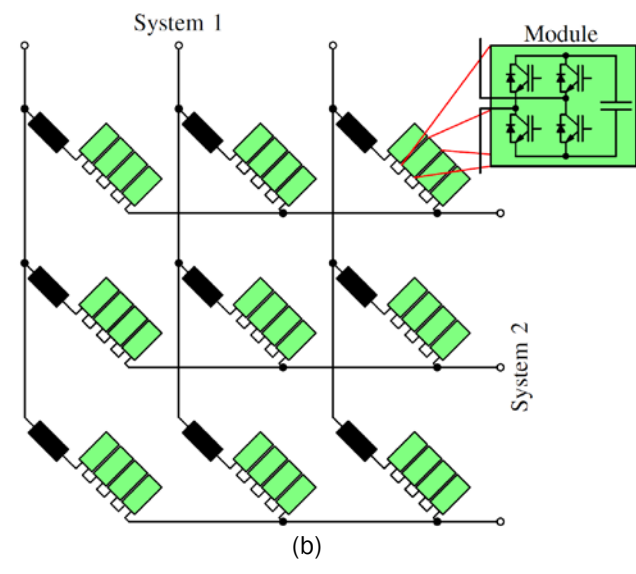
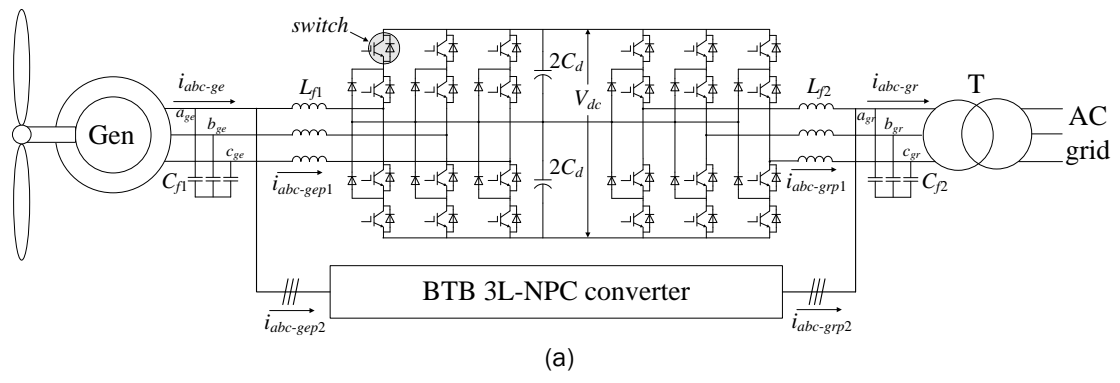


Fig. 1-2 Power electronic converters for unsegmented generator. (a) Converter configuration of P3L-based BTB Power Converter. (b) Converter configuration of MMMC. (c) Converter configuration of CSI-Actfilt.

In this report, the power electronic converters based on above topologies will be designed for the SCG and PDDG in 10 and 20 MW wind turbines, respectively, where the non-segmented generator and segmented generator will be considered for the SCG and PDDG. The related control of the power electronic converters for the requirement of the wind turbine and grid code will also be

designed. The wind turbine based on the designed power electronic converters will be modelled and simulated.

1.4 References

- [1-1] B. Wu, Y. Lang, N. Zargari, and S. Kouro, *Power Conversion and Control of Wind Energy System*, Wiley 2011.
- [1-2] Z. Chen, "An overview of power electronic converter technology for renewable energy systems," in *Direct-Drive Wind and Marine Energy Systems*, Edited by Markus Mueller, Woodhead Publishing Ltd. 2013
- [1-3] Z. Chen, "Power electronic converter systems for direct drive renewable energy applications," in *Direct-Drive Wind and Marine Energy Systems*, Edited by Markus Mueller, Woodhead Publishing Ltd. 2013.
- [1-4] Z. Chen, "Advanced Wind Energy Converters Using Electronic Power Conversion," Durham, PhD Thesis, 1997.
- [1-5] Z. Chen, E. Spooner, "Grid Interface Options for Variable-Speed, Permanent-Magnet Generators", *IEE Proc. -Electr. Power Applications*, Vol. 145, No. 4, July 1998, pp. 273-283.
- [1-6] Z. Chen, E. Spooner, "Grid Power Quality with Variable-Speed Wind Turbines", *IEEE Transactions on Energy Conversion*, Vol. 16, No.2, June 2001, pp. 148-154.
- [1-7] Z. Chen, E. Spooner, "Voltage Source Inverters for High-Power, Variable-Voltage DC Power Sources", *IEE Proc. -Generation, Transmission and Distributions*, Vol. 148, No. 5, September 2001, pp. 439-447.
- [1-8] Z. Chen, E. Spooner, "Current Source Thyristor Inverter And Its Active Compensation System," *IEE Proc. -Generation, Transmission and Distributions*, Vol. 150, No. 4, July 2003, pp. 447-454.
- [1-9] Z. Chen, "Compensation Schemes for A SCR Converter in Variable Speed Wind Power Systems," *IEEE Transactions on Power Delivery*, Vol. 19, No 2, April 2004, pp. 813-821.
- [1-10] Z. Chen. "An introduction of power electronic technology", in *Direct-Drive Wind and Marine Energy Systems*, Edited by Markus Mueller, Woodhead Publishing Ltd. 2013.
- [1-11] Z. Chen. "Power electronic converter systems for direct drive renewable energy applications," in *Direct-Drive Wind and Marine Energy Systems*, Edited by Markus Mueller, Woodhead Publishing Ltd. 2013.

2 VOLTAGE SOURCE CONVERTER DESIGN TAILORED TO SCG

2.1 Introduction

This chapter mainly designs power electronic converters for 10 and 20 MW SCG based wind turbines, where both the non-segmented generator and 4-segmented generator are considered

For the 10 MW SCG, the ac line-to-line voltage V_{ll} is 3.3 kV. As to the non-segmented SCG, its ac current peak value I_m in each phase is 2.47 kA. As to the 4-segmented SCG, the rated power for each segment is 2.5 MW and its current peak value I_m in each phase is 0.617 kA. Each segment of the 4-segmented SCG is isolated. The rated electrical frequency of the generator is 3.22 Hz. The reactance and resistance of the generator are given in Table 2-1. The grid voltage is 3.3 kV and grid frequency is 50 Hz.

For the 20 MW SCG, the ac line-to-line voltage V_{ll} is 6.6 and 3.3 kV for the non-segmented and 4-segmented generator, respectively. As to the non-segmented SCG, its ac current peak value I_m in each phase is 2.47 kA. As to the 4-segmented SCG, the rated power for each segment is 5 MW and its current peak value I_m in each phase is 1.235 kA. Each segment of the 4-segmented SCG is isolated. The rated electrical frequency of the generator is 4.09 Hz. The grid frequency is 50 Hz. The reactance and resistance of the generator are also given in Table 2-1. The grid frequency is 50 Hz. The grid voltage is 6.6 and 3.3 kV for non-segmented and 4-segmented generator, respectively.

Table 2-1
Investigated Wind Turbine Parameter Based on SCG

Rated SCG power (MW)	10		20	
Type	Non-segmented	4-segmented	Non-segmented	4-segmented
Rated power per segment (MW)	10	2.5	20	5
Rated stator line-to-line voltage V_{ll} (V)	3300		6600	3300
AC current peak value I_m in each phase (kA)	2.47	0.617	2.47	1.235
Electrical frequency f (Hz)	3.22		4.09	
Reactance L_d (mH)	13.12	52.46	16.148	16.148
Reactance L_q (mH)	16.95	67.79	21.796	21.796
Resistance per phase R_s (m Ω)	40.73	162.91	58.73	58.73
Grid-side voltage (V)	3300		6600	3300
Grid-side nominal AC frequency (Hz)	50			

2.2 Voltage Source Converter Topologies for SCG

2.2.1 Power Converter Type I for SCG based on Non-segmented Generator

Fig. 2-1 shows the power electronic converter type I for the wind turbine based on the non-segmented generator. The BTB 3L-NPC converter is used here, which is composed with 24 switches. The voltage applied on each switch is only half of the dc-link voltage. The 3L NPC converter is widely used for medium-voltage applications. In comparison with two-level VSC, the three-level NPC converter has lower dv/dt and smaller total harmonic distortion (THD) in its ac output voltages under the same switching frequency [2-1]. In Fig. 2-1, two BTB 3L-NPC converters are connected in parallel for one generator. The rating of each BTB converter is half of the power rating of the wind turbine.

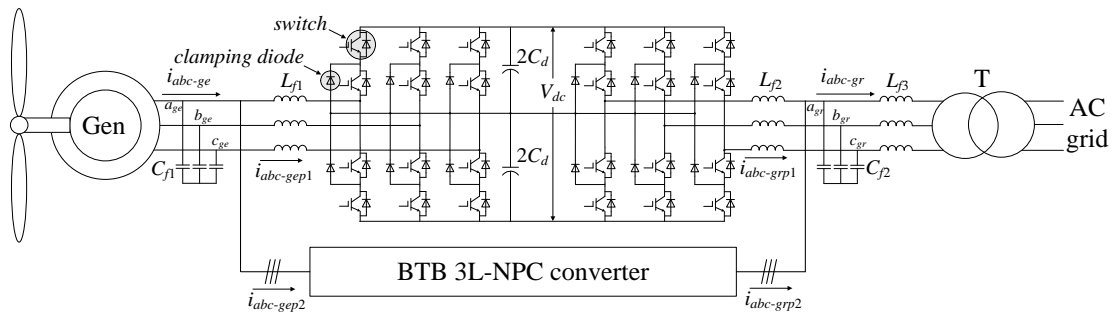


Fig. 2-1 Block diagram of the power converter type I for the non-segmented generator.

2.2.2 Power Converter Type II for SCG based on 4-Segmented Generator

Fig. 2-2 shows the power electronic converter type II for the wind turbine based on 4-segmented generator, where the BTB 3L-NPC converter is also used. Owing to the multiple segments in the SCG, each segment of the SCG is connected to one BTB 3L-NPC converter, which is the difference from the wind turbine with non-segmented generator in Fig. 2-1.

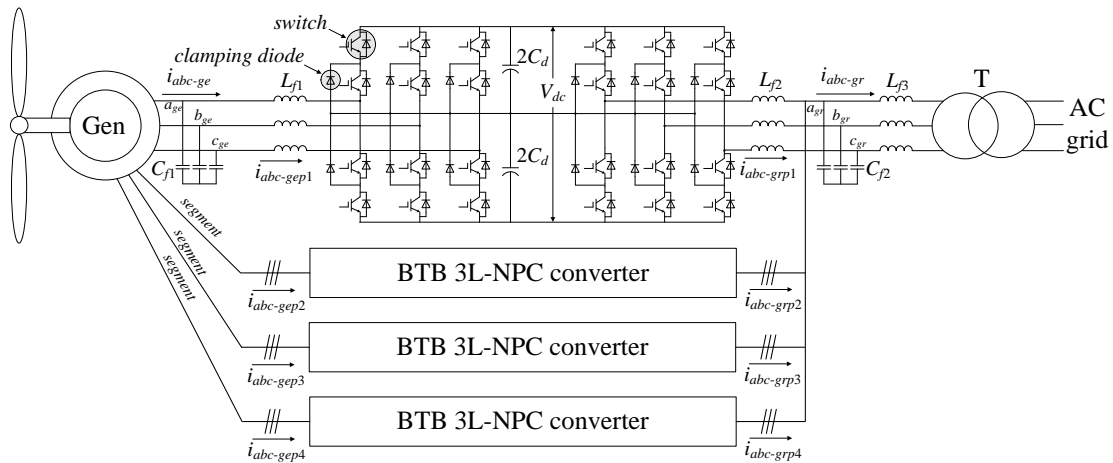


Fig. 2-2 Block diagram of the power converter type II for the 4-segmented generator.

2.3 Costs

The main costs of the power converters include:

- Semiconductors Costs
- Passive components (inductor & capacitor) Costs
- Cooling Systems Costs
- Mechanical Systems Costs

The costs of the power converter for 10 & 20 MW wind turbine systems based on the non-segmented & 4-segmented SCG are investigated below.

2.3.1 Semiconductors Costs

Tables 2-2 lists the semiconductor costs for the power converters in the 10 & 20 MW wind turbine systems based on non-segmented and 4-segmented generators.

According to [2-2], the dc-link voltage of the BTB converters can be designed as

$$V_{dc} = V_{ll} \times \sqrt{2} \times 1.15 \quad (2-1)$$

As to the power converters for the wind turbine, their ac voltages V_{ll} may be 3.3 or 6.6 kV, as shown in Table 2-2. The dc-link voltages of the 10 and 20 MW power converters can be designed as 5.4 and 10.8 kV for the 3.3 and 6.6 kV ac voltages, respectively. Each switch in the 3L-NPC converter takes half of the dc-link voltage.

According to [2-2], in the 3L-NPC converter, the required peak repetitive voltage rating for each switch/diode and clamping diode is

$$V_v = \frac{V_{dc}}{2} \times 1.6 \quad (2-2)$$

Hence, the preferred repetitive blocking voltage for each switch in the 3L NPC converter can be calculated as $V_v=4.5$ kV and 9 kV for the 3.3 and 6.6 kV ac voltage, respectively.

In the wind turbine system, as shown in Fig. 2.1 and Fig. 2.2, the switch current is the same to the ac current in each segment phase. As to the 10 MW and 20 MW wind turbine based on the non-segmented generator, the type I power converter composed of two 3L-NPC converters are used, where the switch current is half of the ac stator current and is 1.23 kA. In order to protect the switch, a 2.5 times margin of the RMS current is selected. As a consequence, the required current peak for each switch in the type I power converter tailored for the 10 and 20 MW wind turbine based on non-segmented SCG is 2.22 kA. As to the 10 MW and 20 MW wind turbine based on the 4-segmented generator, the type II power converter composed of one 3L-NPC converter is used, where the switch current is the same to the ac segment phase current and is 0.617 and 1.235 kA, respectively. In order to protect the switch, a 2.5 times margin of the RMS current is selected. As a consequence, the required current peak for each switch in the type II power converter tailored for the 10 and 20 MW wind turbine based on 4-segmented SCG is $I_{swm}=1.1$ and 2.2 kA, respectively.

In this report, the ABB IGCT 5SHX 26L4520 4500V/2200A and diode 5SDF 10H4503 4500V/1100A are used to construct the type I power converter for the 10 MW wind turbines based on the non-segmented generator, as well as the type I and II power converter for the 20 MW wind turbines based on the non-segmented and 4-segmented generator; the ABB IGCT 5SHX 14H4510 4500V/1100A and diode 5SDF 10H4503 4500V/1100A are used to construct the type II power converter for the 10 MW wind turbines based on the 4-segmented generator. Based on the required voltage and current for each switch shown in Table 2-2, the IGCT and clamping diode may be required to be connected in parallel and series in the power converters for the 10 MW and 20 MW systems.

In the 10 and 20 MW wind turbine system based on the non-segmented generator, the required IGCT and clamping Diode number is

$$n_{igct} = \text{ceil}\left(\frac{V_v}{4500}\right) \cdot \text{ceil}\left(\frac{I_{swm}}{2200}\right) \cdot 2 \cdot n_{switch} \quad (2-3)$$

$$n_{cdiode} = \text{ceil}\left(\frac{V_v}{4500}\right) \cdot \text{ceil}\left(\frac{I_{swm}}{1100}\right) \cdot 2 \cdot n_{diode} \quad (2-4)$$

where V_v is the required peak repetitive voltage rating. I_{swm} is the required current peak with 2.5 times RMS margin. n_{switch} is the switch number as 24, as shown in Fig. 2-1. n_{diode} is the clamping diode number as 12, as shown in Fig. 2-1.

In the 10 and 20 MW wind turbine system based on 4-segmented generator, the required IGCT and clamping Diode number is

$$n_{igct} = \text{ceil}\left(\frac{V_v}{4500}\right) \cdot \text{ceil}\left(\frac{I_{swm}}{1100}\right) \cdot 4 \cdot n_{switch} \quad (2-5)$$

$$n_{cdiode} = \text{ceil}\left(\frac{V_v}{4500}\right) \cdot \text{ceil}\left(\frac{I_{swm}}{1100}\right) \cdot 4 \cdot n_{diode} \quad (2-6)$$

where V_v is the required peak repetitive voltage rating. I_{swm} is the required current peak with 2.5 times RMS margin. n_{switch} is the switch number as 24, as shown in Fig. 2-2. n_{switch} is the clamping diode number as 12, as shown in Fig. 2-2.

From Table 2-2, it can be seen that the IGCT number and the diode number in 20 MW wind turbine system based on non-segmented and 4-segmented generator are the same, which are double of that in 10 MW wind turbine system with non-segmented generator. The cost of each semiconductor is listed in Table 2-3, based on which the total cost of the semiconductors can be calculated, as shown in Table 2-4. Fig. 2-3 shows the total semiconductor costs for the 10 and 20 MW wind turbine system. The cost of the semiconductors in 20 MW wind turbine system based on non-segmented and 4-segmented generator are the same, which are double of that in 10 MW wind turbine system based on non-segmented generator. The cost of the semiconductor in 10 MW wind turbine system based on 4-segmented generator is higher than that in 10 MW wind turbine system based on non-segmented generator.

Table 2-2
Costs of Semiconductors for Wind Turbine based on SCGs

Wind turbine power (MW)		10		20	
Generator type		Non-segmented	4-segmented	Non-segmented	4-segmented
AC line-to-line voltage for each segment (V)		3300		6600	3300
Stator AC current peak value for each segment (kA)		2.47	0.617	2.47	1.235
Generator-side AC frequency (Hz)		3.22		4.09	
Grid-side AC frequency (Hz)		50			
Power converter configuration		Type I	Type II	Type I	Type II
DC-link voltage V_{dc} (kV)		5.6		11.2	5.6
switch	Switch voltage (kV)	2.8	2.8	5.6	2.8
	preferred repetitive blocking voltage V_v (kV)	4.5	4.5	9	4.5
	Switch current peak (kA)	1.23	0.617	1.23	1.235
	Switch current peak value with 2.5 times RMS margin I_{swm} (kA)	2.2	1.1	2.2	2.2
	Switch type	IGCT 5SHX 26L4520	IGCT 5SHX 14H4510	IGCT 5SHX 26L4520	
	Connection type in each switch	single	single	2-series	single
Diode voltage (kV)		2.8	2.8	5.6	2.8

Clamping diode	preferred repetitive blocking voltage (kV)	4.5	4.5	9	4.5
	Diode current peak (kA)	1.23	0.617	1.23	1.23
	Switch current peak value with 2.5 times RMS margin (kA)	2.2	1.1	2.2	2.2
	Diode type	5SDF 10H4503			
	Connection type in each switch	2-parallel	single	2-series & 2-parallel	2-parallel
IGCT number		48	96	96	96
Clamping diode number		48	48	96	96
IGCT cost (k€)		91.2	142	182.4	182.4
Diode cost (k€)		14.4	14.4	28.8	28.8
Total Semiconductor costs (k€)		105.6	156.4	211.2	211.2

Table 2-3
Semiconductors Specifications and Cost [reference to ABB in 2015 exchange rate in Auguste 15th]

Semiconductors		Peak repetitive voltage (kV)	DC voltage (kV)	Peak current (kA)	Price/unit (€ ₂₀₁₅)
IGCT	5SHX 26L4520	4.5	2.8	2.2	1900
	5SHX 14H4510			1.1	1480
Diode	5SDF 10H4503			1.1	300

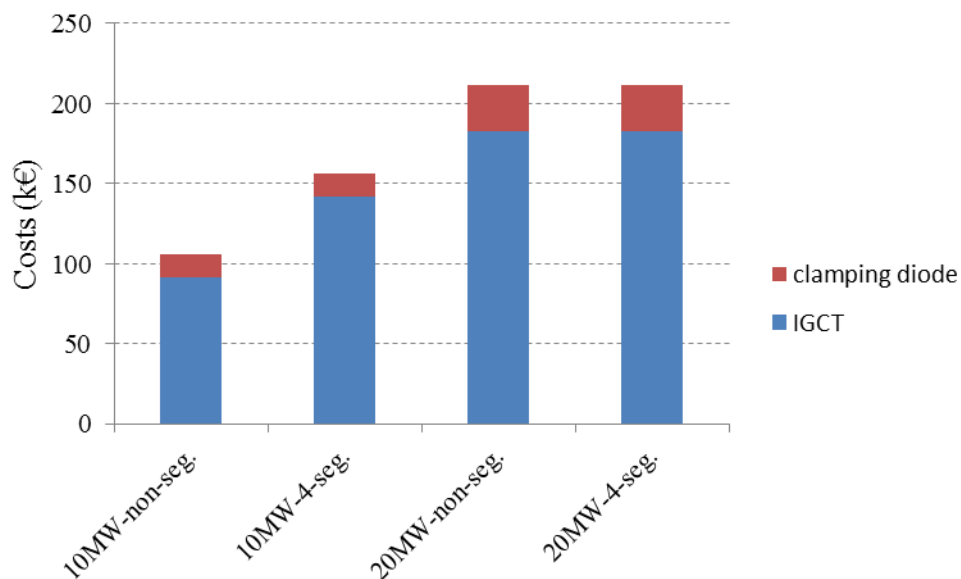


Fig. 2-3. Semiconductor costs for 10 & 20 MW wind turbine based on non-segmented and 4-segmented SCGs.

2.3.2 Passive Components Costs

The costs of the passive components in the configurations of the BTB power converters are investigated and compared. The passive component mainly includes the filter inductor, filter capacitor, and the dc-link capacitor.

The filter is usually adopted in industry to reduce the harmonics around the switching frequency and multiples of the switching frequency at the generator side and the grid side of the BTB power converter. The design of the filter is closely related to switching frequency. Owing to the application of IGCT in the power converter, the switching frequency f_{sw} for the 3L-NPC converter is selected as 500 Hz [2-3].

During the design of the filter, some design criteria should be specified to meet the generator-side and grid-side requirements. Here, the THD of the generator-side current is limited less than 3.5% and the grid-side current is limited less than 5% [2-4]. The filter capacitor value is limited by the decrease of the power factor at the rated power, which is generally less than 5%. According to [2-5], the filter capacitor can be obtained as

$$C_f = k \frac{P_n}{6\pi f U_g^2} \quad (2-7)$$

where k is the coefficient and $k < 5\%$. P_n is the rated power of the converter. U_g is the ac phase voltage. f is the ac source frequency.

The filter is normally used at the ac side, the filter design is carried out by setting the resonance frequency f_{res} of the filter below the switching frequency f_{sw} , generally around $0.5f_{sw}$ but often lower than this value due to the effect of the sub-harmonics of switching frequency [2-4], [2-5]. The resonance frequency of the LC filter is calculated by

$$f_{res} = \frac{\sqrt{L_f + L_m}}{2\pi \sqrt{C_f L_f L_m}} \quad (2-8)$$

where L_f is the converter-side filter inductance, C_f is the filter capacitance, L_m is the generator leakage inductance on the generator side or the combination of the grid inductance and transformer leakage inductance on the grid side. The damping resistance R_f (series-connected in the filter capacitor branch C_{f1} and C_{f2} in Fig. 2-1) are essential to suppress resonance. According to [2-6], the value of damping resistance can be design as

$$R_f = \frac{1}{6\pi f_{res} C_f} \quad (2-9)$$

According to [2-4], the dc-link capacitor of the 3L-NPC converter can be designed as

$$C_d = \frac{P_n}{2f_{sw} V_{dc} \Delta u} \quad (2-10)$$

where P_n is rated power of converter. Δu is voltage ripple, V_{dc} is dc-link voltage. The capacitor voltage ripple is limited under 1%. In addition, the variation of the dc-link's neutral point potential is selected to be restricted to 10% of the dc-link voltage.

After the design of these passive components, the designed inductance and capacitance are used in the simulation, as shown in Tables 2-4. The film capacitor 710uF/1200V is selected for dc-link capacitor [2-6], as shown in Table 2-5. The filter capacitor is shown in Table 2-6 [2-6]. The prices of the filter inductor are estimated based on copper and iron volume referring to the Chapter 3. Fig. 2-4 shows the costs of the passive components 10 and 20 MW wind turbine based on non-segmented and 4-segmented SCG. From Fig. 2-4, it can be seen that the filter inductor is the most expensive passive components and the filter ac capacitor is the cheapest passive component. The cost of the passive component for the 20 MW wind turbine system is more than that for the 10 MW wind turbine system.

Table 2-4
Costs of Passive Components for Wind Turbine based on SCGs

Wind turbine power (MW)		10		20	
Generator type		Non-segmented generator	4-Segmented generator	Non-segmented generator	4-Segmented generator
Average switching frequency for each switch (Hz)		500			
Generator-side filter	Inductor L_{f1} (mH)	1.4	2.8	2.4	1.4
	Capacitor (mF)	0.4	0.2	0.224	0.4
Grid-side filter	Inductor L_{f2} (mH)	2	2.2	3	1.75
	Capacitor (mF)	0.15	0.15	0.075	0.15
	Inductor L_{f3} (mH)	0.7	0.3	1	0.3
DC-link capacitor	Capacitor C_d (mF)	12.5	6.25	6.25	12.5
Total cost of inductor (k€ ₂₀₁₅)		207.6	167	286	367.3
Total cost of filter capacitor (k€ ₂₀₁₅)		41.4	26.3	77.5	41.4
Total cost of DC-link capacitor (k€ ₂₀₁₅)		168.2	168.2	336.5	336.5
Total passive components costs (k€ ₂₀₁₅)		417.2	361.5	700	745.2

Table 2-5
DC Capacitors [2-6]

Type	Capacitance (uF)	Voltage (V)	Price/unit (€ ₂₀₁₅)
DC capacitor WIMA DCP6K07119EP00KS0F	1190	700 (DC)	125.18

Table 2-6
Reference Price for Filter Capacitor [2-6]

Type	Capacitance (uF)	Voltage (V)	Price/unit (€ ₂₀₁₅)
------	------------------	-------------	---------------------------------

Filter AC capacitor MKP1847630354Y5	30	300 (AC)	15.29
--	----	----------	-------

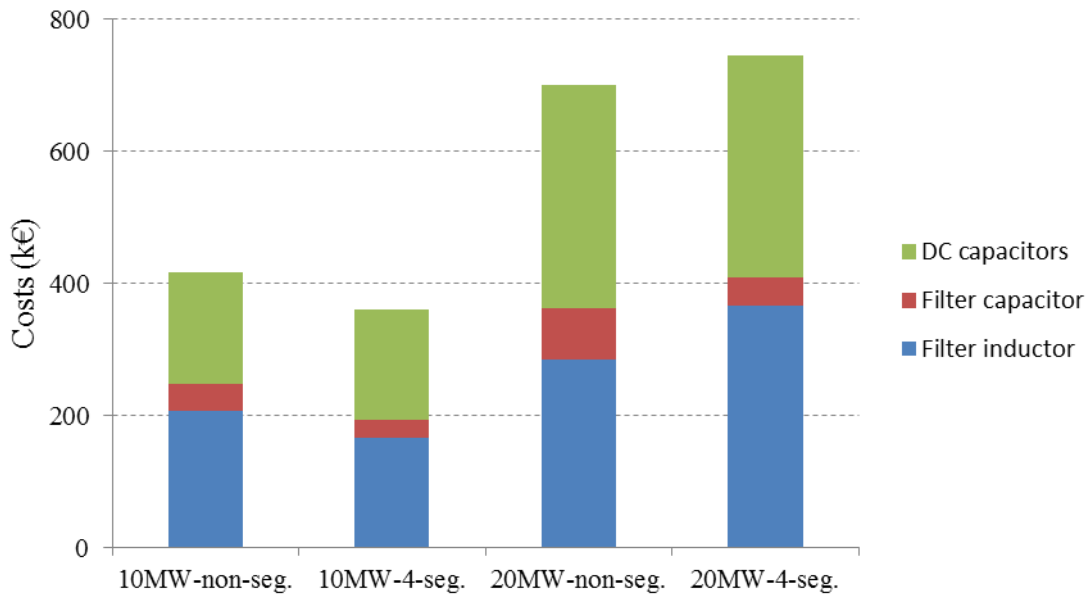


Fig. 2-4. Total passive components costs for 10 & 20 MW wind turbine based on non-segmented and 4-segmented SCGs.

2.3.3 Cooling System Costs

The cost of the cooling system is estimated based on the maximum power loss of the power converter and a cost per loss factor of 0.8€/W from the report D3.32. Based on the power converter efficiency shown in Figs. 2-10 to Fig. 2-12 (see Section 2.4), Table 2-10 lists the costs of the cooling system for the power converters in 10 MW and 20 MW wind turbine based on non-segmented and 4-segmented generators. Fig. 2-5 illustrates the cooling system costs for the power converters in 10 MW and 20 MW wind turbine based on non-segmented and 4-segmented generators. The cooling system costs for 20 MW power converters are nearly double of that for 10 MW power converters.

Table 2-7
Costs of Cooling System

Wind turbine power (MW)	10		20	
Generator type	Non-segmented generator	4-segmented generator	Non-segmented generator	4-segmented generator
Cooling system cost (k€ ₂₀₁₅)	110	136	233	256

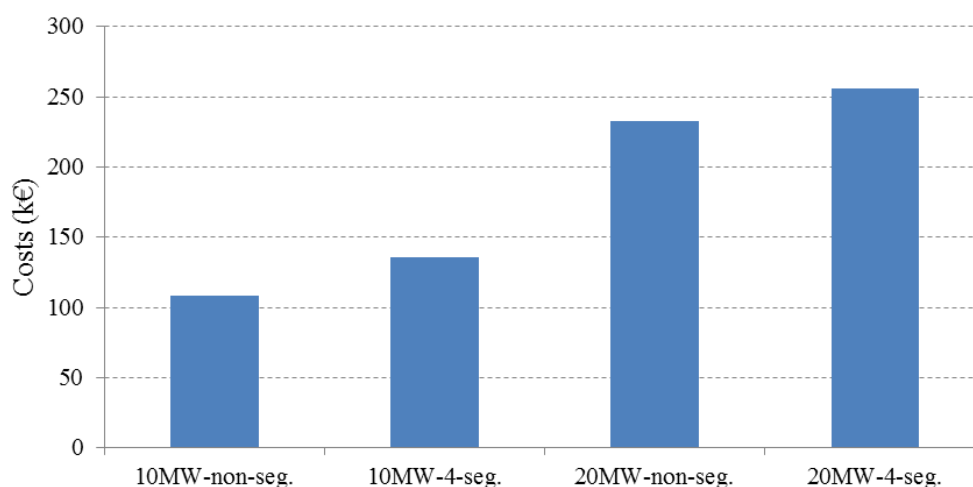


Fig. 2-5. Cooling system costs for 10 & 20 MW wind turbine based on non-segmented and 4-segmented SCGs.

2.3.4 Conclusions

Table 2-8 lists the total power converter costs including semiconductor cost, passive components cost, cooling system cost, and mechanical system cost, where the mechanical system cost is about 40% of the total cost excluding the cooling system.

Fig. 2-6 illustrates the power converter costs for the 10 and 20 MW wind turbines based on non-segmented and 4-segmented SCG. It is easy to be observed that the cost of the 10 MW power converter system for the wind turbine based on 4-segmented generator is a little higher than that for the wind turbine based on non-segmented generator mainly because more semiconductor cost for the power converters tailored for 4-segmented generator. The cost of the 20 MW power converter system for the wind turbine based on 4-segmented generator is a little higher than that for the wind turbine based on non-segmented generator mainly because more passive components are required for the power converters tailored for 4-segmented generator. The cost of the power converter system for 20 MW wind turbine based on non-segmented generator is nearly double of that for 10 MW wind turbine based on non-segmented generator. The cost of the power converter system for 20 MW wind turbine based on 4-segmented generator is nearly double of that for 10 MW wind turbine based on 4-segmented generator.

Table 2-8
Costs in k€₂₀₁₅ of Different Power Converter Configurations for Wind Turbine based on SCGs

Wind turbine power (MW)		10		20	
SCG type		Non-segmented	4-segmented	Non-segmented	4-segmented
Power converter type		Type I	Type II	Type I	Type II
Semiconductor cost (k€)		105.6	156.4	211.2	211.2
Passive components costs	Filter inductor cost (k€)	207.6	167	286	367.3
	Filter capacitor cost (k€)	41.4	26.3	77.5	41.4
	DC-link capacitor cost (k€)	168.2	168.2	336.5	336.5

Cooling system cost (k€)	110	136	233	256
Mechanical cost (k€)	200.9	198.6	348	366
Total cost (k€)	841.9	861.1	1508.7	1595

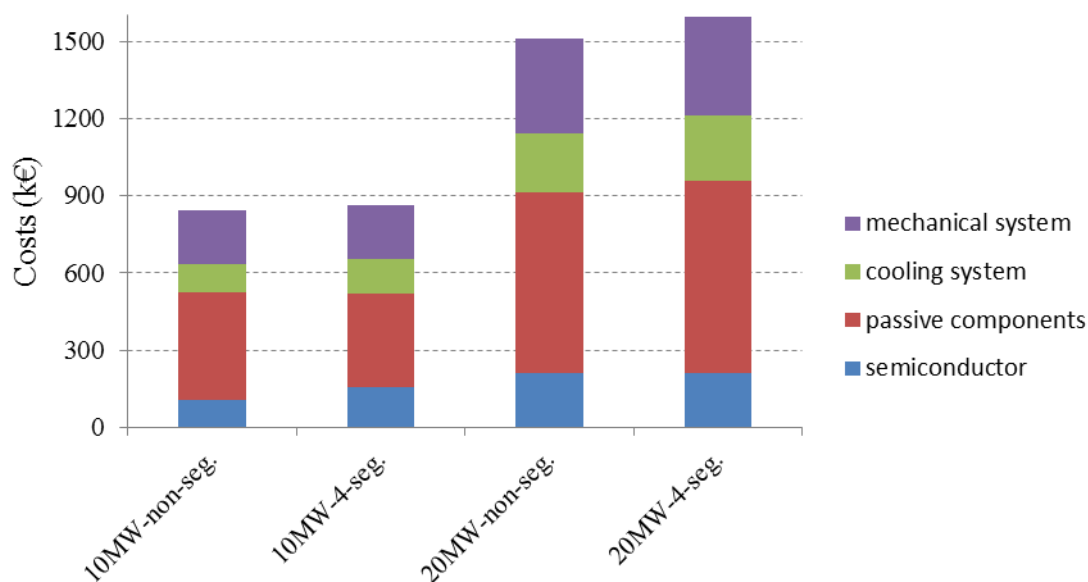


Fig. 2-6. Power electronic converter system costs for 10 & 20 MW wind turbine based on non-segmented and 4-segmented SCGs.

2.4 Size and Weight

2.4.1 Converter Size

The size of power converters for 10 and 20 MW wind turbine based on non-segmented and 4-segmented generators are roughly estimated here, as shown in Table 2-9, where the size of active rectifier unit, inverter unit, control unit, and cooling unit, etc. are considered.

The ABB 4.5 MVA and 9 MVA - PCS 6000 BTB power converters with the size of 5100×1200×2450 (L×W×H mm) and 5700×1200×2450 (L×W×H mm) [2-7] are referred here for the size estimation of 10 and 20 MW power converters tailored for non-segmented and 4-segmented generators, respectively. Suppose the linear relationship between the converter power and converter size, the size of the 2.5, 5 and 10 MW power converters can be estimated as 4830*1200*2450 (L×W×H mm), 5160*1200*2450 (L×W×H mm) and 5830*1200*2450 (L×W×H mm). The 10 MW wind turbine based on the type I power converter configuration tailored for non-segmented generator contains two 5 MW power converter, whose size is (2*5160)*1200*2450 (L×W×H mm). The 10 MW wind turbine based on the type II power converter configuration tailored for 4-segmented generator contains four 2.5 MW power converter, whose size is (4*4830)*1200*2450 (L×W×H mm). The 20 MW wind turbine based on the type I power converter configuration tailored for non-segmented generator contains two 10 MW power converter, whose size is (2*5830)*1200*2450 (L×W×H mm). The 20 MW wind turbine based on the type II power converter configuration tailored for 4-segmented generator contains four 5 MW power converter, whose size is (4*5160)*1200*2450 (L×W×H mm). The sizes of the power converter for the 10 and 20 MW wind turbine are listed in Table 2-9. Fig. 2-7 illustrates the power converter system size for 10 & 20 MW wind turbine based on non-segmented and 4-segmented generators. The size of the power converter for 10 MW wind turbine based on 4-segmented generator is bigger than that for 10 MW wind turbine based on non-segmented generator. The size

of the power converter for 20 MW wind turbine based on 4-segmented generator is bigger than that for 20 MW wind turbine based on non-segmented generator.

Table 2-9
Size of Power Converter System

Power converters	Generator type	Cubic size (L*W*H mm)	Volume (m ³)
10 MW	Non-segmented generator	(2*5160)*1200*2450	30.4
	4-segmented generator	(4*4830)* 1200*2000	46.4
20 MW	Non-segmented generator	(2*5830)*1200*2450	34.3
	4-segmented generator	(4*5160)*1200*2450	60.8

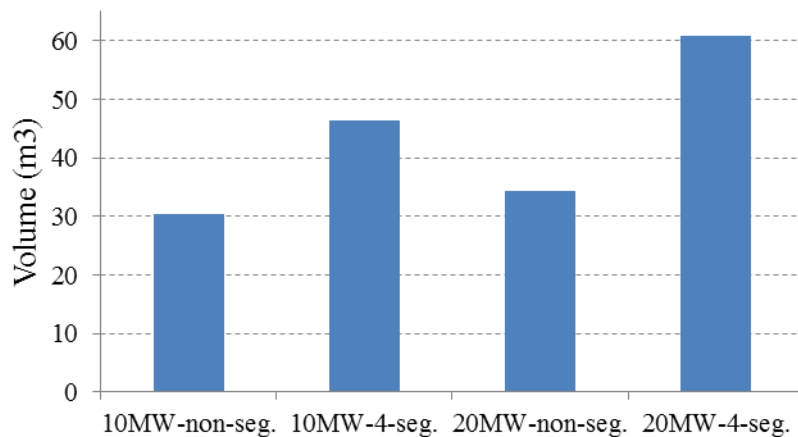


Fig. 2-7. Power converter system size for 10 & 20 MW wind turbine based on non-segmented and 4-segmented generators.

2.4.2 Converter Weight

The weight of power converters for 10 and 20 MW wind turbine based on non-segmented and 4-segmented generators are roughly estimated here, as shown in Table 2-10. The ABB 4.5 MVA and 9 MVA - PCS 6000 full power converters with the weight of approximately 5250 kg and 6200 kg [2-7] are referred here for the weight estimation of the 10 and 20 MW power converters tailed for non-segmented and 4-segmented generators, respectively. Suppose the linear relationship between the converter power and the converter weight, the weight of the 2.5, 5 and 10 MW power converters can be estimated as 4827, 5355 and 6411 kg. The 10 MW wind turbine based on the type I power converter configuration tailed for non-segmented generator contains two 5 MW power converter, whose weight is 2*5355 kg. The 10 MW wind turbine based on the type II power converter configuration tailed for 4-segmented generator contains four 2.5 MW power converter, whose weight is 4*4827 kg. The 20 MW wind turbine based on the type I power converter configuration tailed for non-segmented generator contains two 10 MW power converter, whose weight is 2*6411 kg. The 20 MW wind turbine based on the type II power converter configuration tailed for 4-segmented generator contains four 5 MW power converter, whose weight is 4*5355 kg. The weight of the power converter for the 10 and 20 MW wind turbine are listed in Table 2-10.

Fig. 2-8 illustrates the power converter system size for 10 & 20 MW wind turbine based on non-segmented and 4-segmented generators. The weight of the power converter for 10 MW wind turbine based on non-segmented generator is lighter than that for 10 MW wind turbine based on 4-segmented generator. The weight of the power converter for 20 MW wind turbine based on non-segmented generator is lighter than that for 20 MW wind turbine based on 4-segmented generator.

Table 2-10
Weight of Power Converter System

Power converters	Generator type	Weight (kg)
10 MW	Non-segmented generator	2*5355
	4-segmented generator	4*4827
20 MW	Non-segmented generator	2*6411
	4-segmented generator	4*5355

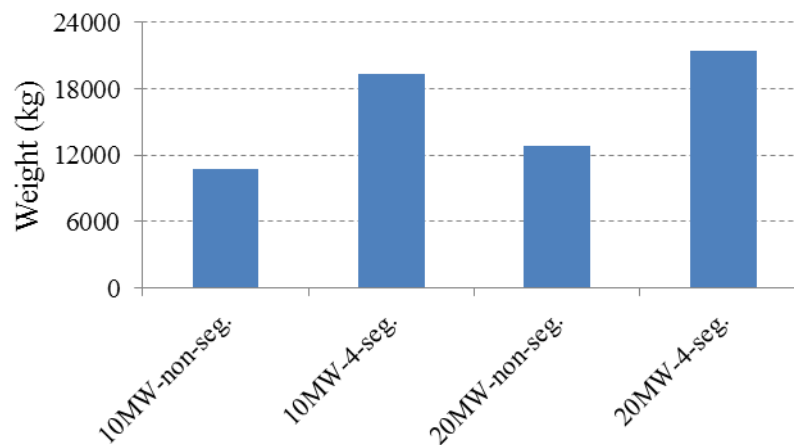


Fig. 2-8. Power converter system weight for 10 & 20 MW wind turbine based on non-segmented and 4-segmented generators.

2.5 Efficiency, Energy Capture and Wind Energy Cost

The 10 MW and 20 MW wind power system based on non-segmented and 4-segmented generator are modeled and simulated with the professional time-domain simulation tool PSCAD/EMTDC [2-8]. The system parameters are shown in the Appendix and the relationships between the wind speed and the power for the 10 MW and 20 MW wind turbine system are shown in Fig. 2-12. The resultant simulated semiconductor currents (IGBT and Diode currents) are used for power losses calculation with the IGBT and Diode data-sheet from the manufactures. The conduction losses and switching losses of the semiconductors (IGBT and Diode) are mainly considered here.

The semiconductor conduction losses can be calculated using a semiconductor approximation with a series connection of DC voltage source u_{vo} representing semiconductor on-state zero-current collector-emitter voltage and a collector emitter on-state resistance r_c as [2-9]

$$u_v(i_c) = u_{vo} + r_c \cdot i_c \quad (2-11)$$

where i_c is semiconductor current. These important parameters (u_{v0} and r_c) can be read directly from the semiconductor (IGBT and Diode in Table 2-3) datasheet. The instantaneous value of the semiconductor conduction losses can be expressed as

$$P_{ce}(t) = u_v(t) \bullet i_c(t) \quad (2-12)$$

The average conduction losses can be obtained as

$$P_{ceav} = \frac{1}{T_{sw}} \int_0^{T_{sw}} P_{ce}(t) dt \quad (2-13)$$

where the switching period $T_{sw}=1/f_{sw}$. The switching losses in the semiconductor are the product of switching energies and the switching frequency f_{sw} as

$$P_{sw}(t) = (E_{on} + E_{off}) \bullet f_{sw} \quad (2-14)$$

where E_{on} and E_{off} are the turn-on and turn-off energy losses in the semiconductor, which can be read directly from the semiconductor datasheet. As a consequence, the semiconductor losses can be calculated as

$$P_{loss} = P_{ceav} + P_{sw} \quad (2-15)$$

2.5.1 Efficiency for 10 MW Power Converters

The efficiency for the 10 MW power converters tailored for non-segmented and 4-segmented SCG is shown in Fig. 2-9. It can be observed that the efficiency curves for the two power converters tailored for non-segmented and 4-segmented SCG are similar.

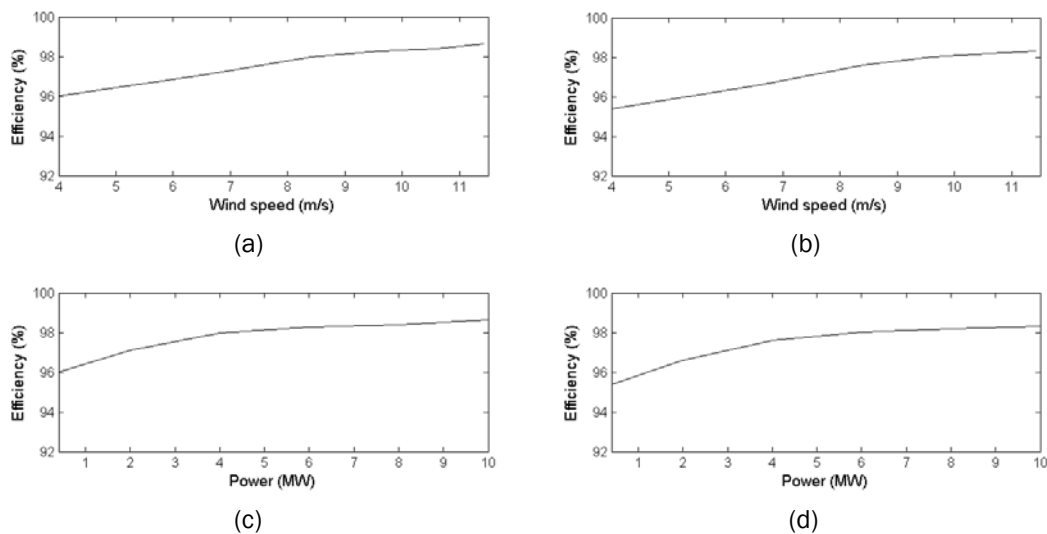


Fig. 2-9. Efficiency for 10 MW power converters. (a) For non-segmented generator. (b) For 4-segmented generator. (c) For non-segmented generator. (d) For 4-segmented generator.

2.5.2 Efficiency for 20 MW Power Converters

The efficiency for the 20 MW power converters tailored for non-segmented and 4-segmented SCG is shown in Fig. 2-10. It can be observed that the efficiency curves for the two power converters tailored for non-segmented and 4-segmented SCG are similar.

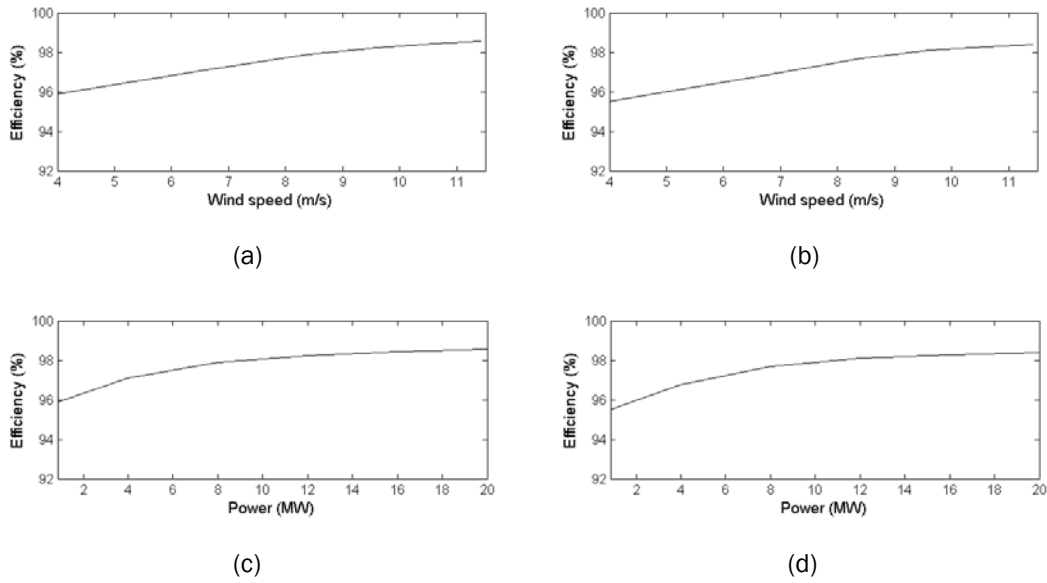


Fig. 2-10. Efficiency for 20 MW power converters. (a) For non-segmented generator. (b) For 4-segmented generator. (c) For non-segmented generator. (d) For 4-segmented generator.

2.5.3 Energy Capture and Wind Energy Cost

According to the report D1.21, The IEC Class 1A wind climate is used here, which is given by

$$f(v) = \frac{v}{\sigma^2} e^{-\frac{v^2}{2\sigma^2}} \quad (2-16)$$

where v is the wind speed. $\sigma=7.98$ m/s. The corresponding cumulative distribution of wind speed is given by

$$F_v(v) = \int_0^v f(v') dv' \quad (2-17)$$

The wind probability and the cumulative distribution of wind speed are illustrated in Fig. 2-11.

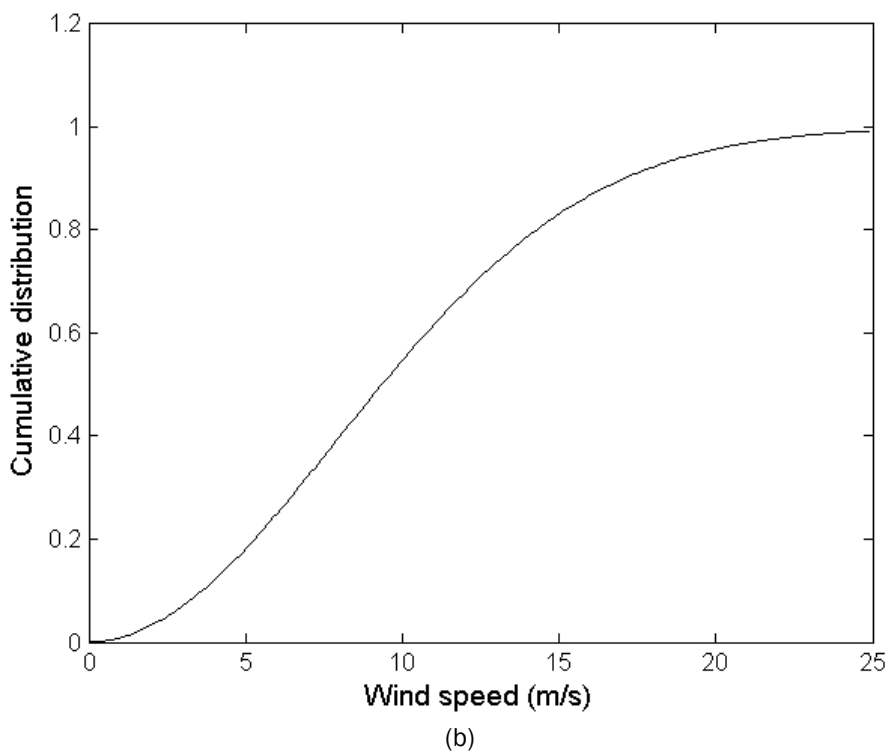
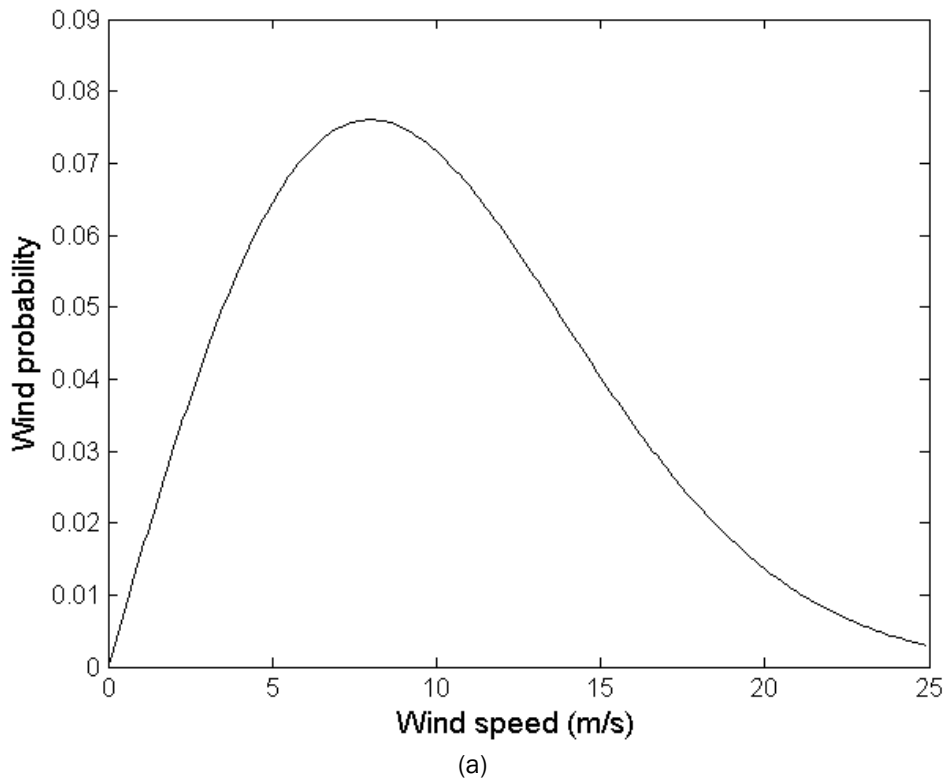


Fig. 2-11. (a) Wind probability. (b) Cumulative distribution of wind speed.

According to [2-10], the relationships between the wind speed and the power for 10 MW and 20 MW wind turbine system can be obtained, as shown in Fig. 2-12.

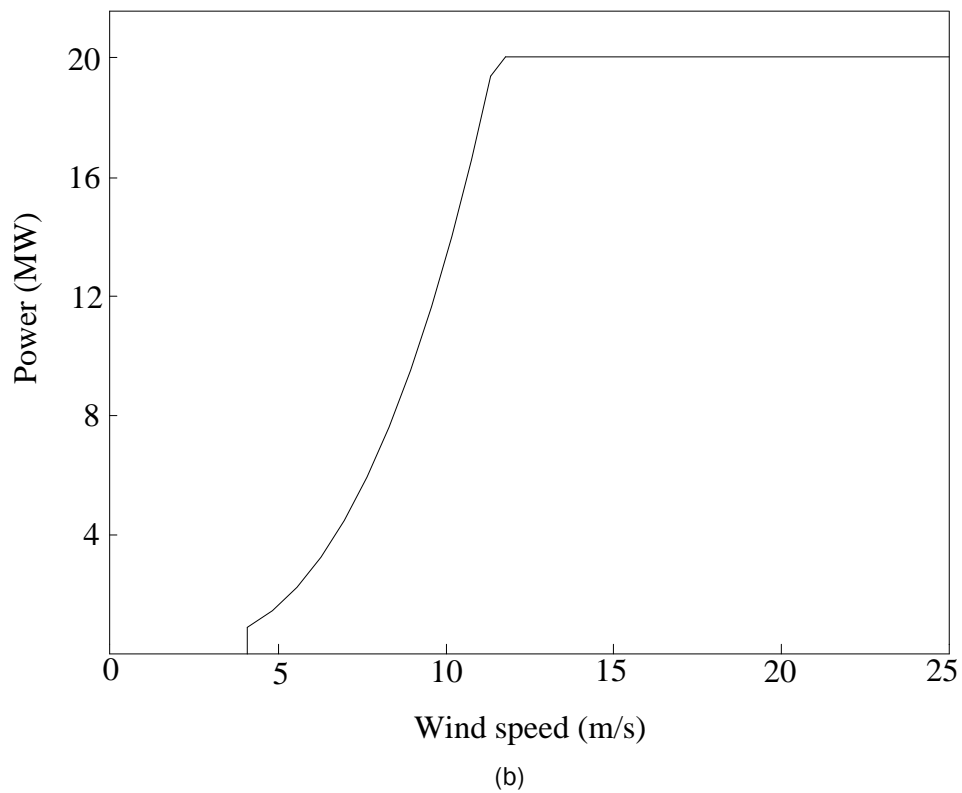
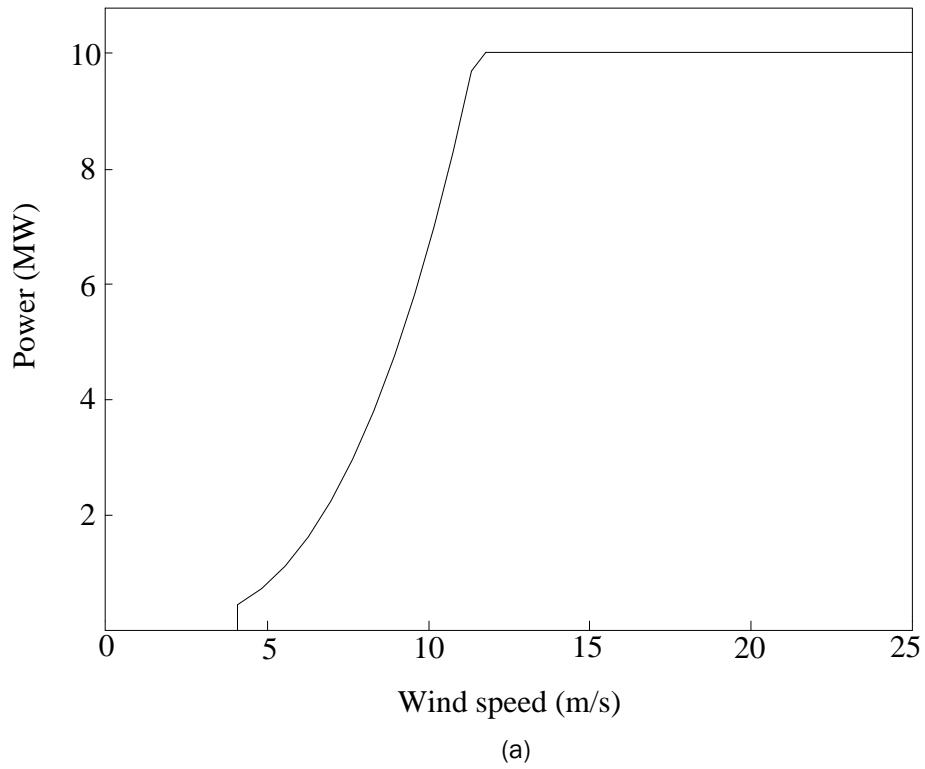
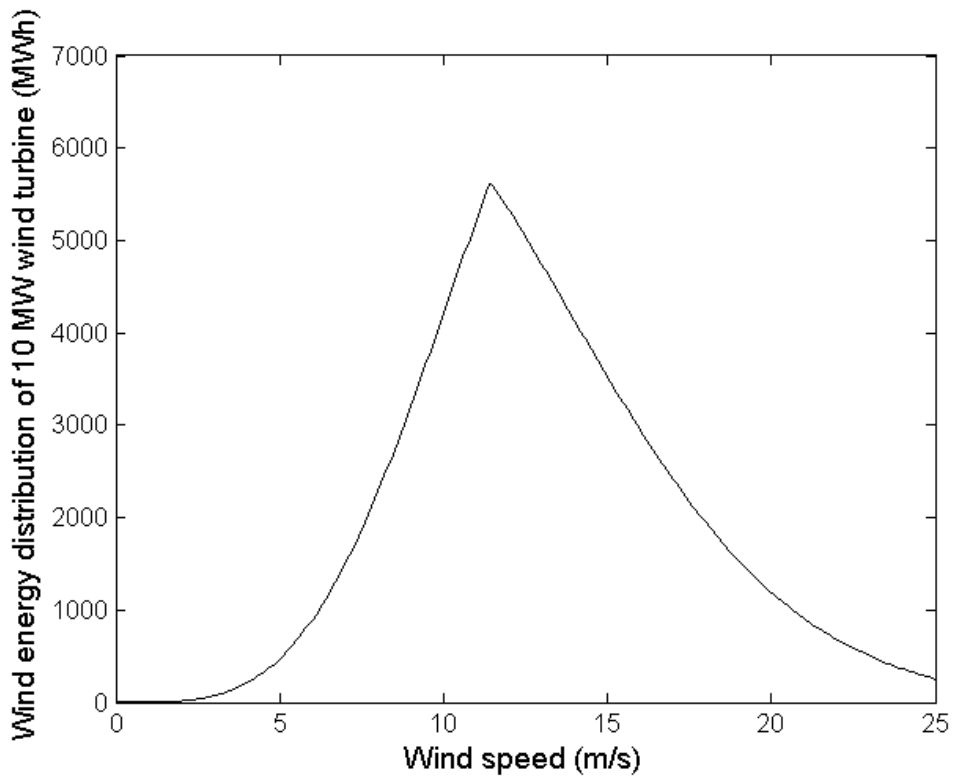
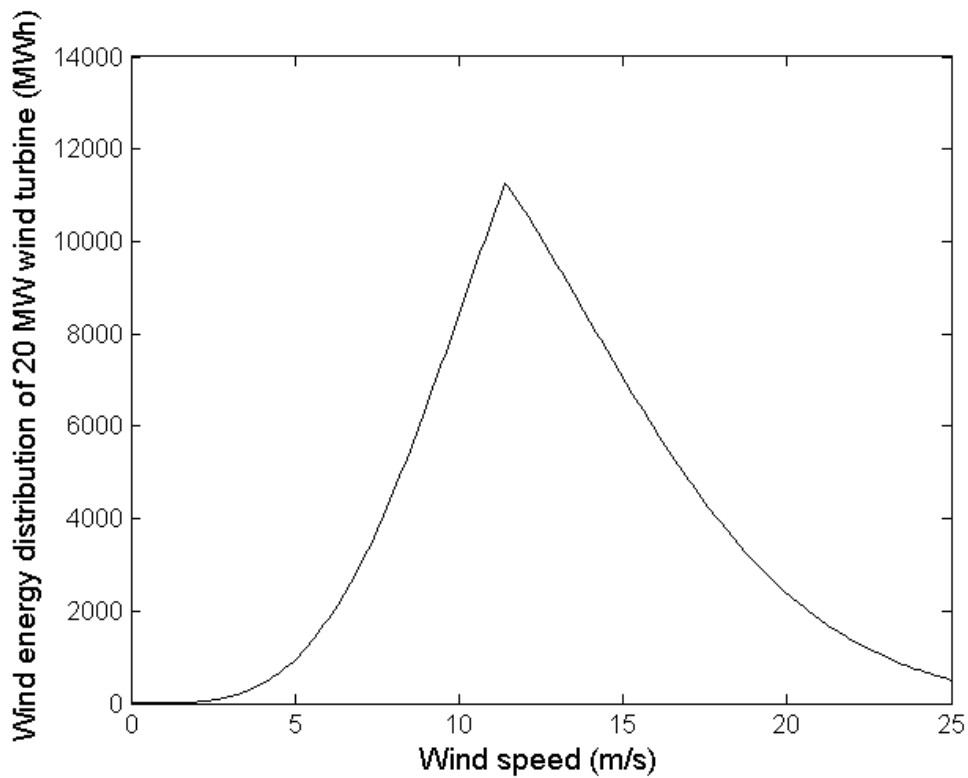


Fig. 2-12. Relationship between wind speed and power. (a) 10 MW wind turbine system. (b) 20 MW wind turbine system.



(a)



(b)

Fig. 2-13. Wind energy distribution in one year. (a) 10 MW wind turbine system. (b) 20 MW wind turbine system.

According to Fig. 2-11 and Fig. 2-12, the wind energy distribution in one year for the 10 and 20 MW wind turbine system can be produced, as shown in Figs. 2-13(a) and (b), respectively. The cut-in and cut-out speed of wind turbine is 4 m/s and 25m/s, respectively. Considering the contribution by power electronic system, according Fig. 2-13(a) and Fig. 2-9, it can obtain that the annual energy production (AEP) of the 10 MW wind turbine system based on non-segmented and 4-segmented generator are approximately 47588 and 47423 MWh, respectively, as listed in Table 2-11, where the small difference is derived from the efficiency difference in Fig. 2-9. Considering the contribution by power electronic system, according Fig. 2-13(b) and Fig. 2-10, the AEP of the 20 MW wind turbine system based on non-segmented and 4-segmented generator are approximately 95171 and 95018 MWh, respectively, as listed in Table 2-11, where the small difference is derived from the efficiency difference in Fig. 2-10. In addition, the corresponding utilization hour and the capacity factor is also given in Table 2-11, as

$$\text{Utilization hour} = \frac{\text{AEP}}{\text{Wind turbine rated power}} \quad (2-18)$$

$$\text{Capacity factor} = \frac{\text{Utilization hour}}{365 \text{ days} \times 24 \text{ hours/day}} \quad (2-19)$$

Fig. 2-14 illustrates the AEP. The wind energy yield for the 10 MW wind turbine based on non-segmented and 4-segmented generators are nearly the same. The wind energy yield for the 20 MW wind turbine based on non-segmented and 4-segmented generators are nearly the same. The wind energy yield for the 20 MW wind turbine is nearly double of that for the 10 MW wind turbine.

Table 2-11
Wind Energy Yield

Wind turbine	10MW Non-segmented	10MW 4-segmented	20MW Non-segmented	20MW 4-segmented
AEP (MWh)	47588	47423	95171	95018
Utilization hour (h)	4758.8	4742.3	4758.6	4750.9
Capacity factor (%)	54.3	54.1	54.3	54.2

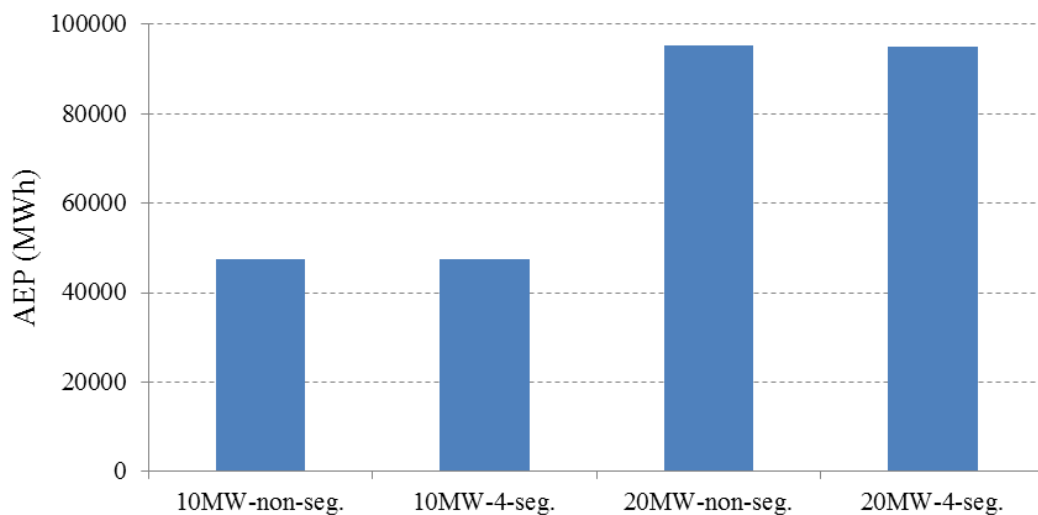


Fig. 2-14. Wind energy yield in one year.

The cost of energy (CoE) can be calculated for the 10 and 20 MW wind turbine based on non-segmented and 4-segmented generators as

$$CoE = \frac{C_{converter}}{AEP \times Lifetime} \quad (2-20)$$

Suppose that the wind turbine can be used for 25 years, according to Table 2-8 and Table 2-11, the CoE for the 10 and 20 MW wind turbine based on non-segmented and 4-segmented generators can be obtained as listed in Table 2-12. Fig. 2-15 illustrates the CoE of the 10 and 20 MW wind turbine based on non-segmented and 4-segmented generators, where the 10 MW wind turbine based on 4-segmented generator has the highest CoE and the 20 MW wind turbine based on non-segmented generator has the lowest CoE.

Table 2-12
Cost of Energy

Wind turbine	10MW Non-segmented	10MW 4-segmented	20MW Non-segmented	20MW 4-segmented
CoE (€/MWh)	0.71	0.73	0.63	0.67

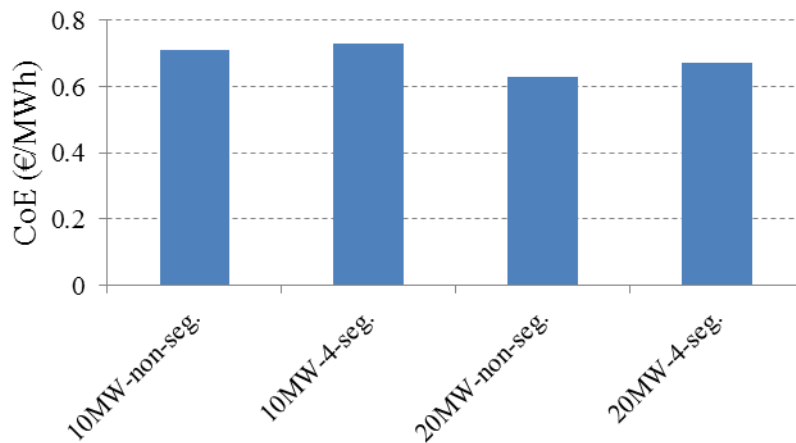


Fig. 2-15. Cost of energy of 10 and 20 MW wind turbine based on non-segmented and segmented generators.

2.6 Control Strategy Design

2.6.1 Control for Normal Operation

According to the power electronic converter configuration shown in Fig. 2-1 and Fig. 2-2, it can be seen that each BTB 3L-NPC converter is composed of a generator-side converter and a grid-side converter. Normally, the generator-side converter is used to control the generator for optimal power capture. The grid-side converter is used to keep the dc-link voltage V_{dc} constant.

A. Generator-Side Converter Control

The generator-side converter connected to the generator stator effectively decouples the generator from the grid. Thus, the generator rotor and the wind turbine rotor can rotate freely depending on the wind conditions.

The generator-side converter is used to regulate the wind turbine to enable optimal speed tracking for optimal power capture from the wind. The control structure for the generator-side converter is shown in Fig. 2-16. With the d -axis aligned with the rotor flux [2-11], the controller is based on the dynamic model of the generator in the synchronous rotating frame as

$$\begin{cases} u_{dg} = R_s i_{dg} + L_d \frac{di_{dg}}{dt} - L_q \omega_r i_{qg} \\ u_{qg} = R_s i_{qg} + L_q \frac{di_{qg}}{dt} + L_d \omega_r i_{dg} + \omega_r \psi_r \end{cases} \quad (2-21)$$

$$T_e = 1.5n_p((L_d - L_q)i_d i_q + i_q \psi_f) \quad (2-22)$$

where u_{ds} and u_{qs} , i_{ds} and i_{qs} , L_d and L_q are the d - and q -components of the stator voltage, stator current and stator inductance, respectively. R_s , ψ_r and ω_r stand for stator resistance, rotor flux and rotor speed, respectively. T_e is the generator electromagnetic torque. n_p is the pole-pair number. The active power P_g and reactive power Q_g can be expressed as

$$\begin{cases} P_g = \frac{3}{2}(u_{qg} i_{qg} + u_{dg} i_{dg}) \\ Q_g = \frac{3}{2}(u_{dg} i_{dg} - u_{qg} i_{qg}) \end{cases} \quad (2-23)$$

Owing to the d -axis aligns with the rotor flux, where the u_{ds} is 0, the q -axis current is proportional to the active power P_g and the d -axis stator current is proportional to the reactive power Q_g . Normally, the reactive power reference is set to zero to perform unity power factor operation.

In Fig. 2-16, the control block for the generator-side converter adopts double control loops. Based on the measured generator speed ω , the MPPT method calculates the optimal power command P_{g_ref} using the rotor speed versus power characteristic [2-12]. One thing to be mentioned is that, the power converter type I is used for non-segmented generator, as shown in Fig. 2-1. Hence, each 3L-NPC converter takes only half of the wind turbine power. In this situation, the coefficient k in Fig. 2-16 is 2. The power converter type II is used for 4-segmented generator, as shown in Fig. 2-2. In this situation, each 3L-NPC converter takes only one fourth of the wind turbine power and the coefficient k in Fig. 2-16 is 4. The proportional-integral (PI) controllers are used in the outside loop to regulate the generator active power P_g and reactive power Q_g so as to track the reference P_{g_ref} and Q_{g_ref} , respectively, and produces corresponding q -axis current command i_{qg_ref} and d -axis current command i_{dg_ref} . In the inside loop, the PI controllers are adopted to regulate d - and q -axis stator current to track the command value.

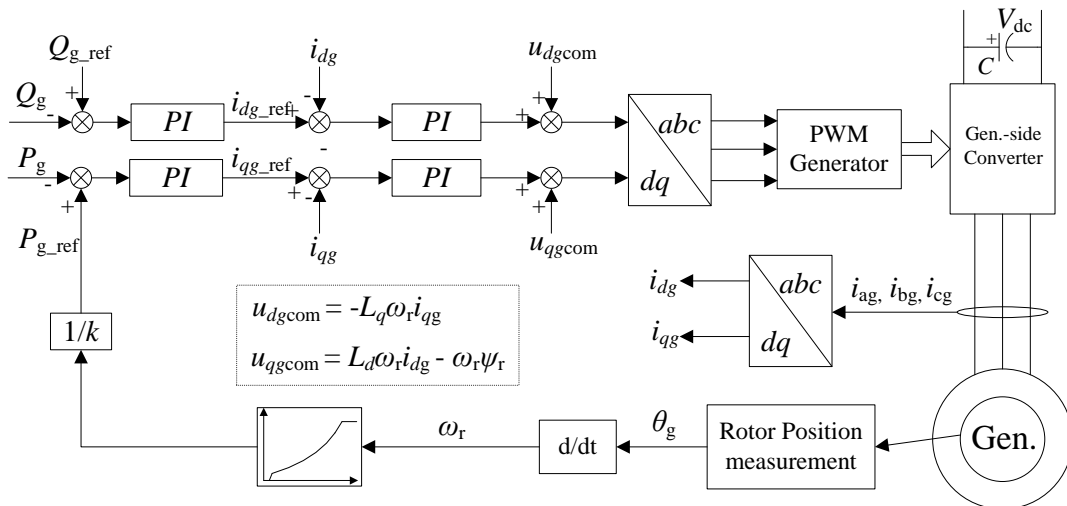


Fig. 2-16. Control strategy for the generator-side converter.

B. Grid-Side Converter Control

The grid-side converter is used to keep the dc-link voltage V_{dc} constant and regulate the reactive power of the grid. The control for the grid-side converter is shown in Fig. 2-17. With the d -axis aligned with the grid voltage vector position [2-13], the dynamic model of the grid-side converter in the synchronous rotating frame can be described as

$$\begin{cases} u_{ds} = R_{fs}i_{ds} + L_{fs} \frac{di_{ds}}{dt} + U_m \\ u_{qs} = R_{fs}i_{qs} + L_{fs} \frac{di_{qs}}{dt} \end{cases} \quad (2-24)$$

$$\begin{cases} P_s = \frac{3}{2}U_m i_{ds} \\ Q_s = \frac{3}{2}U_m i_{qs} \end{cases} \quad (2-25)$$

$$C \frac{dV_{dc}}{dt} = \frac{P_s}{V_{dc}} - i_{load} \quad (2-26)$$

where u_{ds} and u_{qs} are the d - and q -components of the grid-side converter output voltage, respectively. i_{ds} and i_{qs} are the d - and q -components of the grid current, respectively. U_m is grid phase voltage peak value. P_s and Q_s are the grid active and reactive power, respectively. i_{load} is the current shown in Fig. 2-17.

Based on above analysis, the grid-side inverter adapts double control loops. The inside loop is used to control the grid side current. The outside loop is used to maintains the output dc voltage V_{dc} at a fixed value by balancing the input and output power to the dc-link. In addition, the grid-side converter can regulate the grid reactive power.

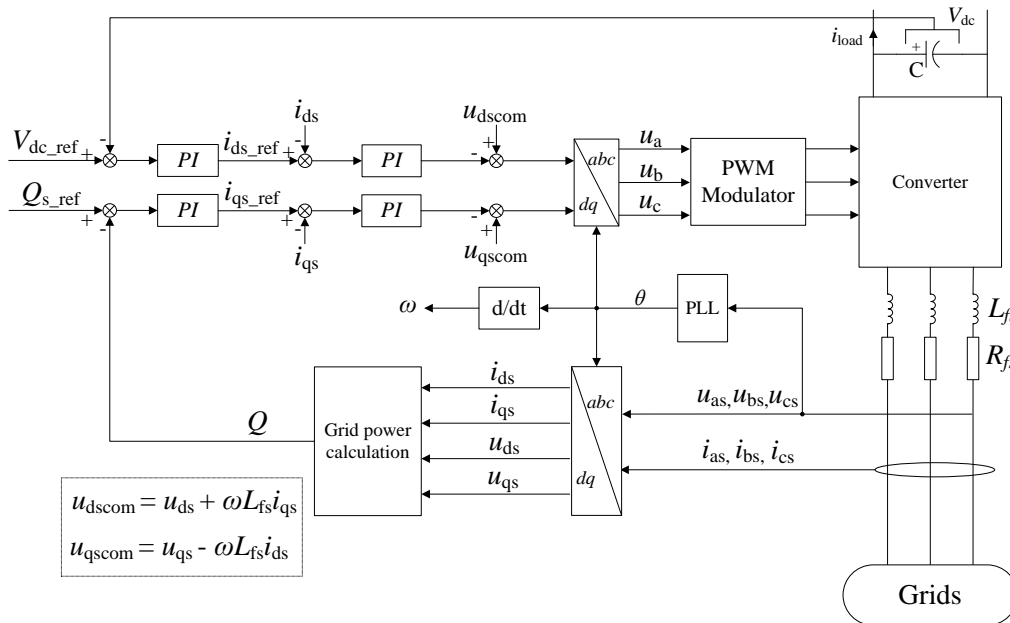


Fig. 2-17. Control strategy for the grid-side converter.

C. Circulating Current Elimination Control

When discontinuous space-vector modulation is used in multiple parallel converters, as shown in Fig. 2-1, because of the different switching characteristics and impedance discrepancy of individual converter, even if synchronized control of each converter is applied, the switching status of the converters in parallel will differ from each other. This results in what is called circulating current in which currents that circulate among power switching devices will not flow into the generators or power grid [2-13]. The existence of this circulation will increase the current flow through the power switching devices, increase the loss of the power converters, and perhaps damage the power converter. Therefore, a circulating current elimination control is essential for the type I power converter configuration with two parallel power converters. One thing to be mentioned is that the wind turbine system based on segmented generator, as shown in Fig. 2-2, has no circulating current because each segment of the generator is isolated.

Fig. 2-18 shows the circulating current control (CCC) in the parallel power converter configuration [2-14]. In Fig. 2-18, the circulating current can be obtained by

$$i_{cc} = \frac{i_{a_grp1} + i_{b_grp1} + i_{c_grp1}}{3} \quad (2-27)$$

The circulating current can be suppressed by using a PI controller, where the grid-side converter can be used to generate the produced reference voltage u_{cc_ref} by the PI controller.

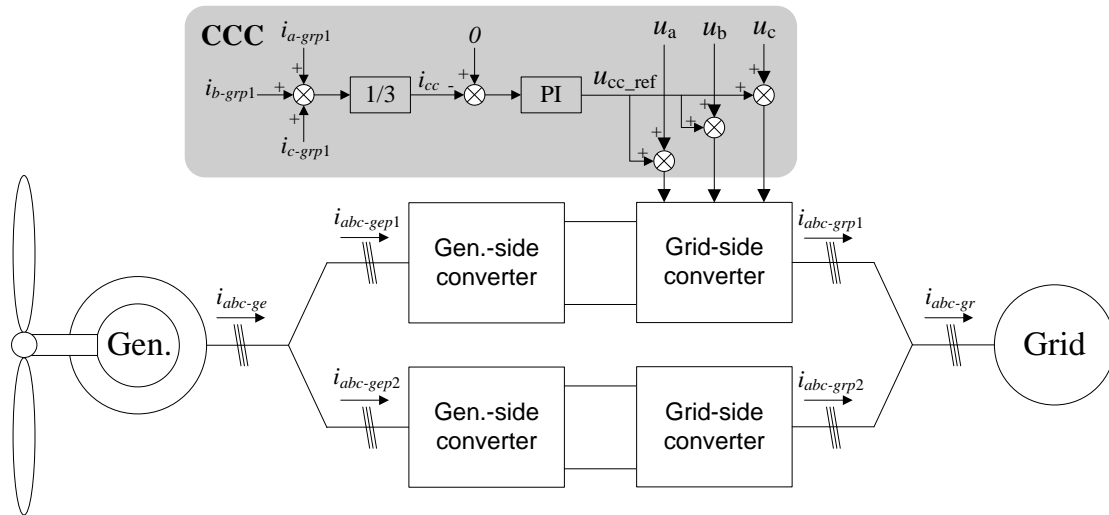


Fig. 2-18. Circulating current elimination control.

2.6.2 Fault Ride-Through Control

In order to analyze the control under grid fault situation, the relationship among turbine speed, dc-link voltage and system parameters, will be established firstly.

Neglecting the power converter losses, Fig. 2-19 shows the power flow branches for the wind turbine system. The different power branches are represented as

$$P_w - P_{gen} = P_m = \omega_w J \frac{d\omega_w}{dt} \quad (2-28)$$

$$P_{gen} - P_{grid} = P_c = u_{dc} C \frac{du_{dc}}{dt} \quad (2-29)$$

where P_{gen} is the generator power, P_m is the power that stored in kinetic energy, P_c is the energy stored in the dc-link capacitor, P_{grid} is the energy injected into the grid, J is the system inertia and generator losses are neglected.

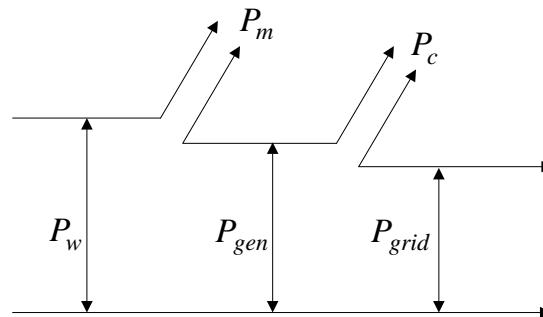


Fig. 2-19. Power flow branches

The wind turbine control for ride-through the grid fault is presented in Fig. 2-20. Based on the measured wind turbine speed, the optimal power-tracking algorithm calculates the power command P_{g_ref} . The generator-side converter uses this power command to control the generator, such that the generator tracks the command power. The grid-side converter maintains the dc-link voltage at a fixed value by balancing the input and output power to the dc-link.

When a fault occurs in the grid, a voltage dip occurs at the output side of the grid-side converter, which results in that the maximum active power that can be exported to the grid is reduced. Thus, the power P_{grid} can be injected into the grid is quickly reduced. However, the generator output power P_{gen} is not reduced as quickly. From Fig. 2-19, it is easy to be observed that there will be more energy stored in the dc-link capacitor, which will result in the increase of dc-link voltage V_{dc} . It could damage the power converter.

The fault ride-through (FRT) control shown in Fig. 2-20 emphasizes the regulation of the dc-link voltage so as to protect the power electronic system without any wind turbine disconnection during a critical voltage dip fault. When the dc-link voltage V_{dc} is over the limited value during the faults, the controller in FRT shown in Fig. 2-20 will produce a compensation component, which will reduce the current reference in the q -axis. As a consequence, the reference power for the generator-side converter will be reduced, which results in that the generator power P_{gen} will be reduced during the fault. Finally, the generator power and the grid power are both reduced during the fault, which can effectively reduce the energy stored in the dc-link capacitor and limit the dc-link voltage in the power electronic converter and protect the power electronic converter during the grid fault situations. The reduction of P_{gen} will cause more energy stored in the mechanical system as P_m , which will increase the wind turbine speed. However, owing to the short fault period and the huge mass of wind turbine, the wind turbine speed is only increased a little during fault with the fault ride-through control.

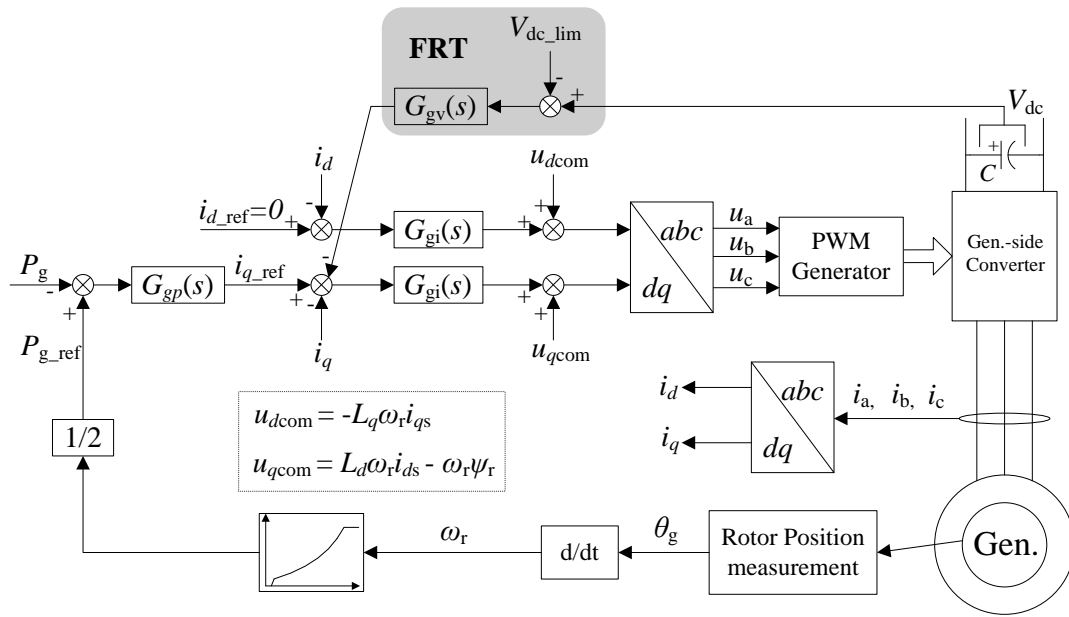


Fig. 2-20. Fault ride-through control for the generator-side converter.

2.7 Simulation Studies

To verify the presented power electronic converters and corresponding control strategy, the 10 MW and 20 MW wind turbine based on the non-segmented generator and 4-segmented generator configuration are modelled, where the generator is modelled referring to [2-11]. The wind turbine parameters are shown in the Appendix. The simulation results are presented in this section, where the power signal has gone through a filter with a time constant of one cycle.

2.7.1 Case I: Under variable wind speed

Fig. 2-21 shows the performance of the 10 MW wind turbine based on the non-segment generator under variable wind speed [2-15]. Fig. 2-21(a) shows the variable wind speed. The generator speed is shown in Fig. 2-21(b). The generator power is shown in Fig. 2-21(c). The dc-link voltage of the power converter is kept balancing during the operation, as shown in Fig. 2-21(d).

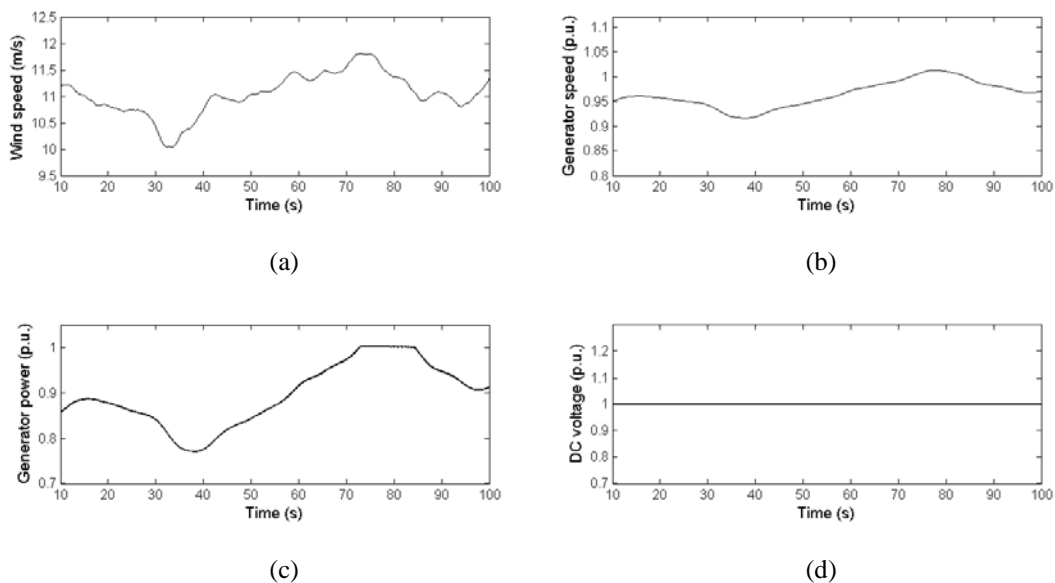


Fig. 2-21. Performance of the 10 MW wind turbine with the non-segmented generator configuration. (a) Wind speed. (b) Generator speed. (c) Generator power. (d) DC-link voltage of the BTB power electronic converter.

Fig. 2-22 shows the performance of the 10 MW wind turbine based on the 4-segmented generator under variable wind speed. Fig. 2-22(a) shows the variable wind speed. The generator speed is shown in Fig. 2-22(b). The generator power is shown in Fig. 2-22(c). The dc-link voltage of the power converter is kept balancing during the operation, as shown in Fig. 2-22(d).

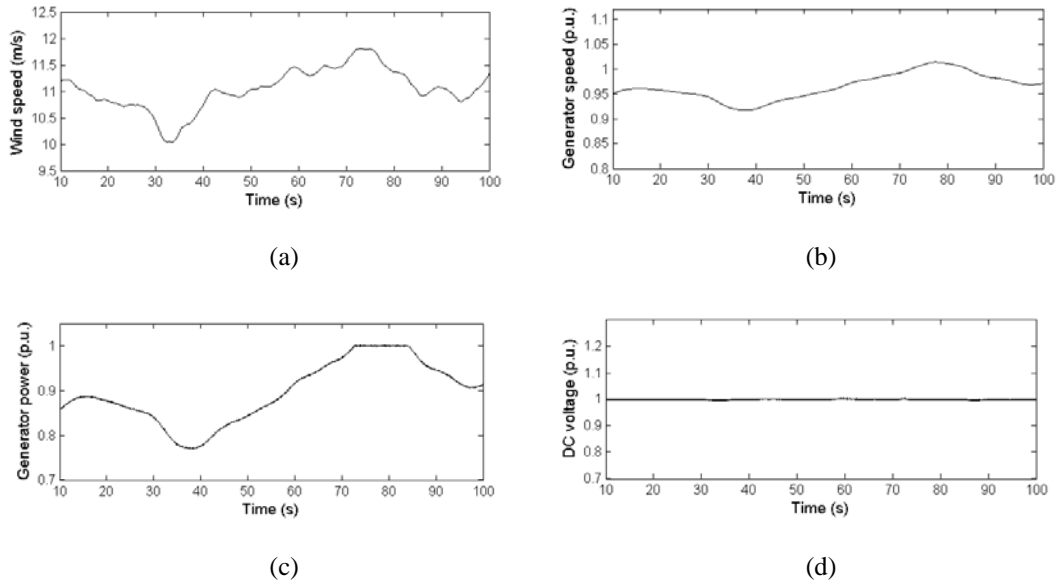


Fig. 2-22. Performance of the 10 MW wind turbine with the 4-segmented generator configuration. (a) Wind speed. (b) Generator speed. (c) Generator power. (d) DC-link voltage of the BTB power electronic converter.

Fig. 2-23 shows the performance of the 20 MW wind turbine based on the non-segment generator under variable wind speed. Fig. 2-23(a) shows the variable wind speed. The generator speed is shown in Fig. 2-23(b). The generator power is shown in Fig. 2-23(c). The dc-link voltage of the power converter is kept balancing during the operation, as shown in Fig. 2-23(d).

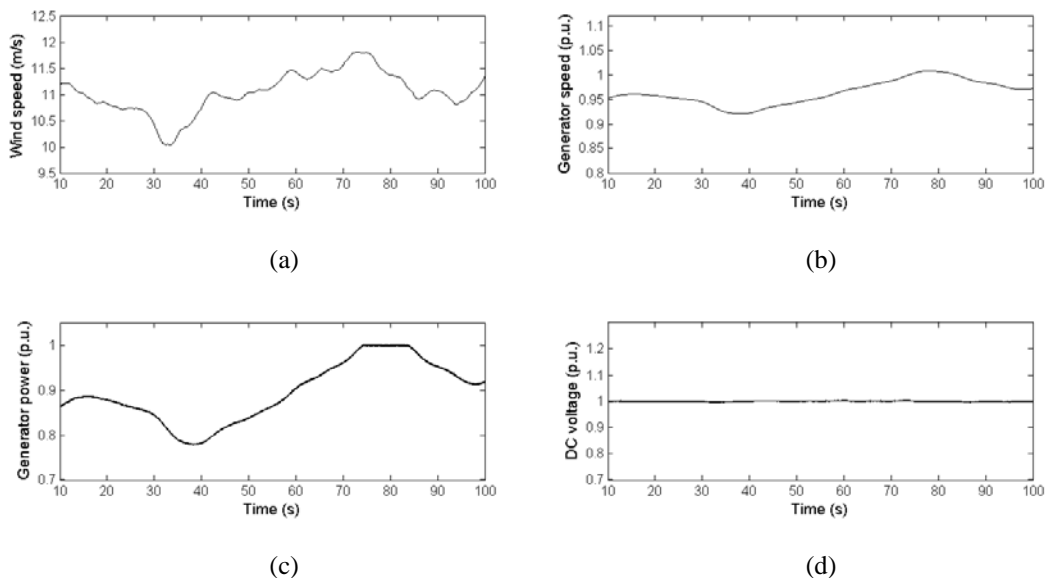


Fig. 2-23. Performance of the 20 MW wind turbine with the non-segmented generator configuration. (a) Wind speed. (b) Generator speed. (c) Generator power. (d) DC-link voltage of the BTB power electronic converter.

Fig. 2-24 shows the performance of the 20 MW wind turbine based on the 4-segment generator under variable wind speed. Fig. 2-24(a) shows the variable wind speed. The generator speed is shown in Fig. 2-24(b). The generator power is shown in Fig. 2-24(c). The dc-link voltage of the power converter is kept balancing during the operation, as shown in Fig. 2-24(d).

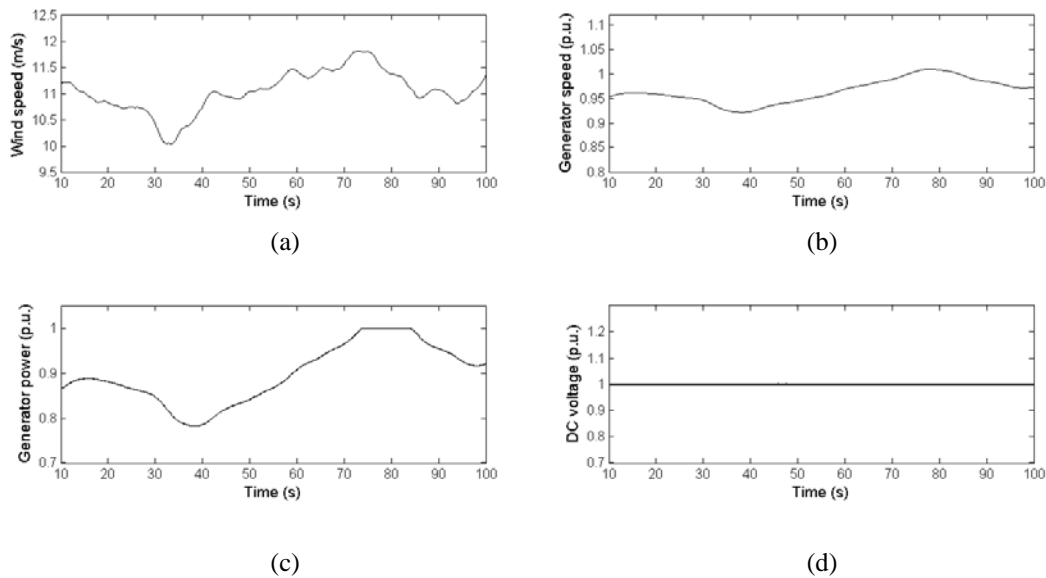
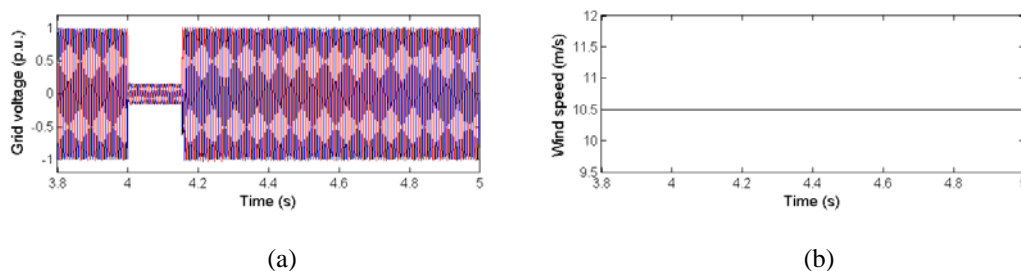


Fig. 2-24. Performance of the 20 MW wind turbine with the 4-segmented generator configuration. (a) Wind speed. (b) Generator speed. (c) Generator power. (d) DC-link voltage of the BTB power electronic converter.

2.7.2 Case II: Grid fault situation

A. 10 MW wind turbine based on non-segmented generator

Fig. 2-25 shows the performance of the 10 MW wind turbine based on the non-segmented generator under grid fault situation, where the FRT control is not used here. Fig. 2-25(a) shows the grid voltage, where the grid voltage dips to a low value approximately 15% of the rated value and lasts for 150 ms [2-16]. Figs. 2-25(b) and (c) show the wind speed and the generator speed, respectively. Fig. 2-25(d) shows the generator power (black curve) and the grid power (blue curve). During the fault period, the generator is still controlled to follow the optimal power and the generator power is nearly unchanged. However, the grid power is reduced because the grid voltage dips. As a consequence, owing to the power unbalance between the generator power and the grid power, more power would be stored in the dc-link capacitor, which would result in the increase of the dc-link voltage. The two dc-link voltages in the two parallel power converters are both increased to a high value during the fault, as shown in Figs. 2-25(e) and (f).



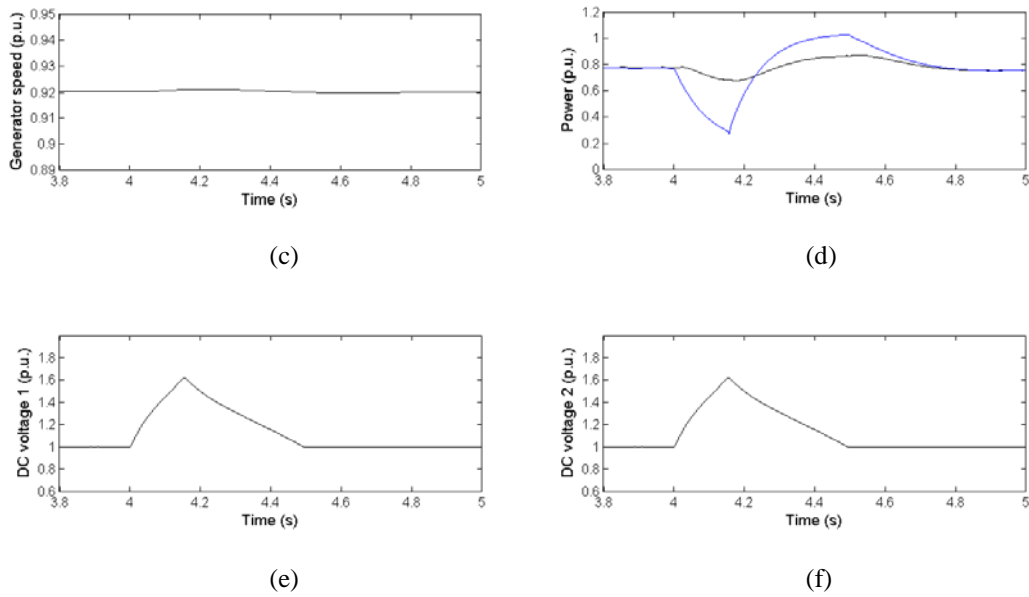
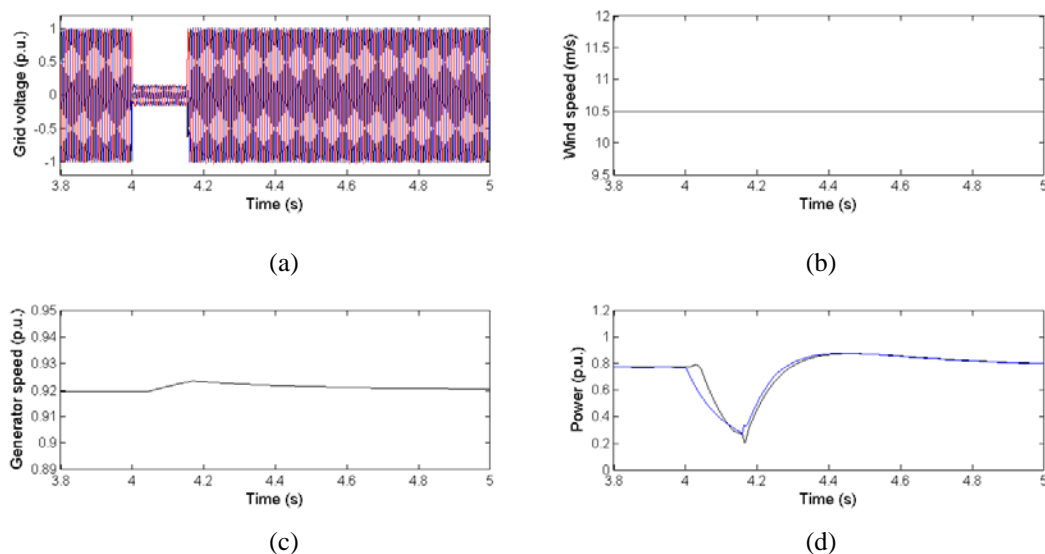


Fig. 2-25. Performance of the 10 MW wind turbine with the single generator configuration under grid voltage dip situation without FRT control. (a) Grid voltage. (b) Wind speed. (c) Generator speed. (d) Generator power and grid power. (e) DC-link voltage V_{dc1} . (f) DC-link voltage V_{dc2} .

Fig. 2-26 shows the performance of the 10 MW wind turbine based on the non-segmented generator under grid fault situation, where the FRT control is used here. Fig. 2-26(a) shows the grid voltage, where the grid voltage dips to a low value approximately 15% of the rated value and lasts for 150 ms. Figs. 2-26(b) and (c) show the wind speed and the generator speed, respectively. Fig. 2-26(d) shows the generator power (black curve) and the grid power (blue curve). During the fault period, the grid power is reduced owing to the grid voltage dips. With the FRT control, the generator power is also reduced, which can effectively limit the dc-link voltage of the power electronic converter. The two dc-link voltages in the two parallel power converters are both limited during the fault, as shown in Figs. 2-26e) and (f), which shows the effectiveness of the presented FRT control. On the other hand, owing to the reduction of the generator power, there will be more energy stored in the kinetic energy. Consequently, it will result in the increase of the wind turbine speed. However, the wind turbine speed is just increased a little in the fault period, as shown in Fig. 2-26(c), because of the large mass of the wind turbine. In addition, the chopper resistor may also be added in the dc-link of the power converter to cost the extra energy and keep the wind turbine system operation under faults [2-17].



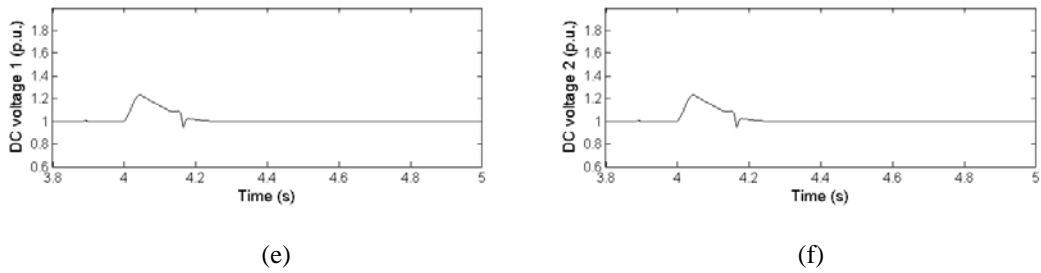
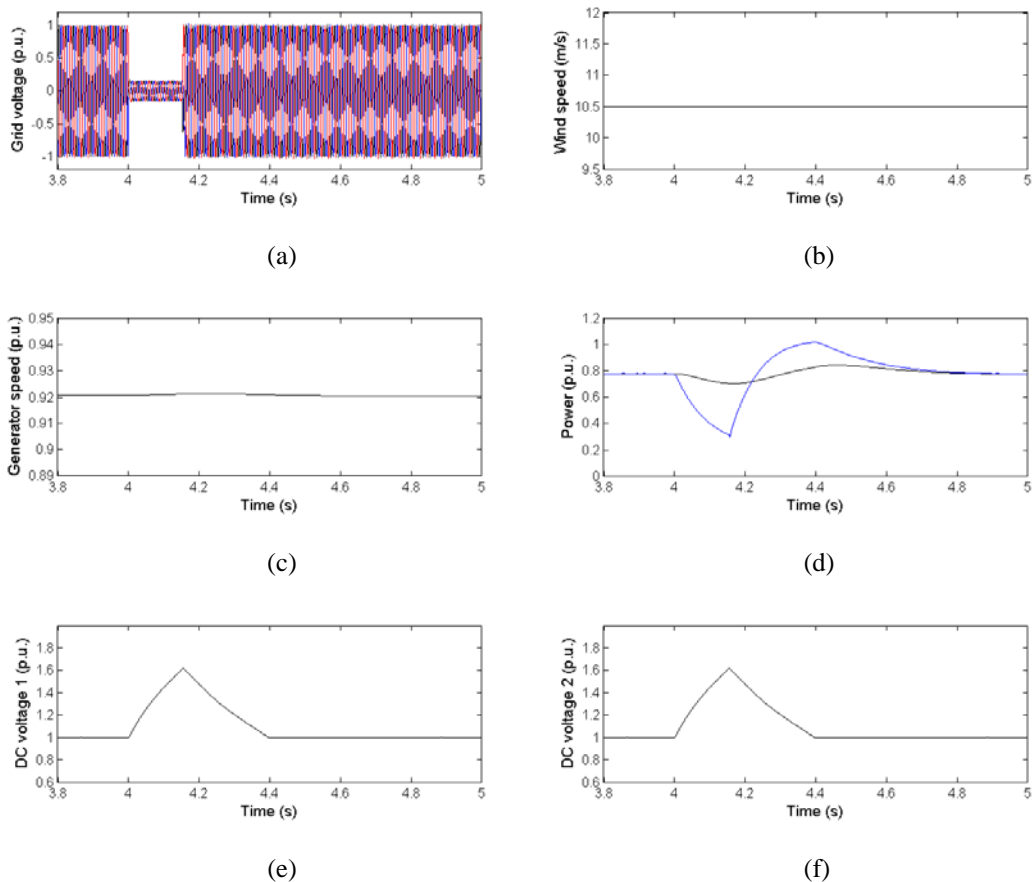


Fig. 2-26. Performance of the 10 MW wind turbine with the single generator configuration under grid voltage dip situation with FRT control. (a) Grid voltage. (b) Wind speed. (c) Generator speed. (d) Generator power and grid power. (e) DC-link voltage Vdc1. (f) DC-link voltage Vdc2.

B. 10 MW wind turbine based on 4-segmented generator

Fig. 2-27 shows the performance of the 10 MW wind turbine based on the 4-segmented generator under grid fault situation, where the FRT control is not used here. Fig. 2-27(a) shows the grid voltage, where the grid voltage dips to a low value approximately 15% of the rated value and lasts for 150 ms. Figs. 2-27(b) and (c) show the wind speed and the generator speed, respectively. Fig. 2-27(d) shows the generator power (black curve) and the grid power (blue curve). During the fault period, the generator is still controlled to follow the optimal power and the generator power is nearly unchanged. However, the grid power is reduced because the grid voltage dips. As a consequence, owing to the power unbalance between the generator power and the grid power, more power would be stored in the dc-link capacitor, which would result in the increase of the dc-link voltage. The four dc-link voltages in the two parallel power converters are both increased to a high value during the fault, as shown in Figs. 2-27(e) and (f).



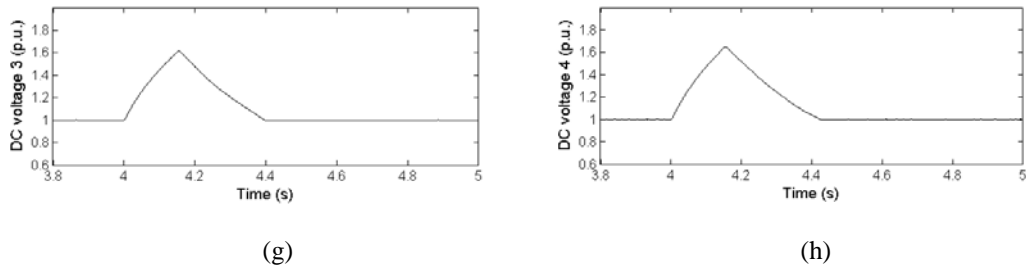
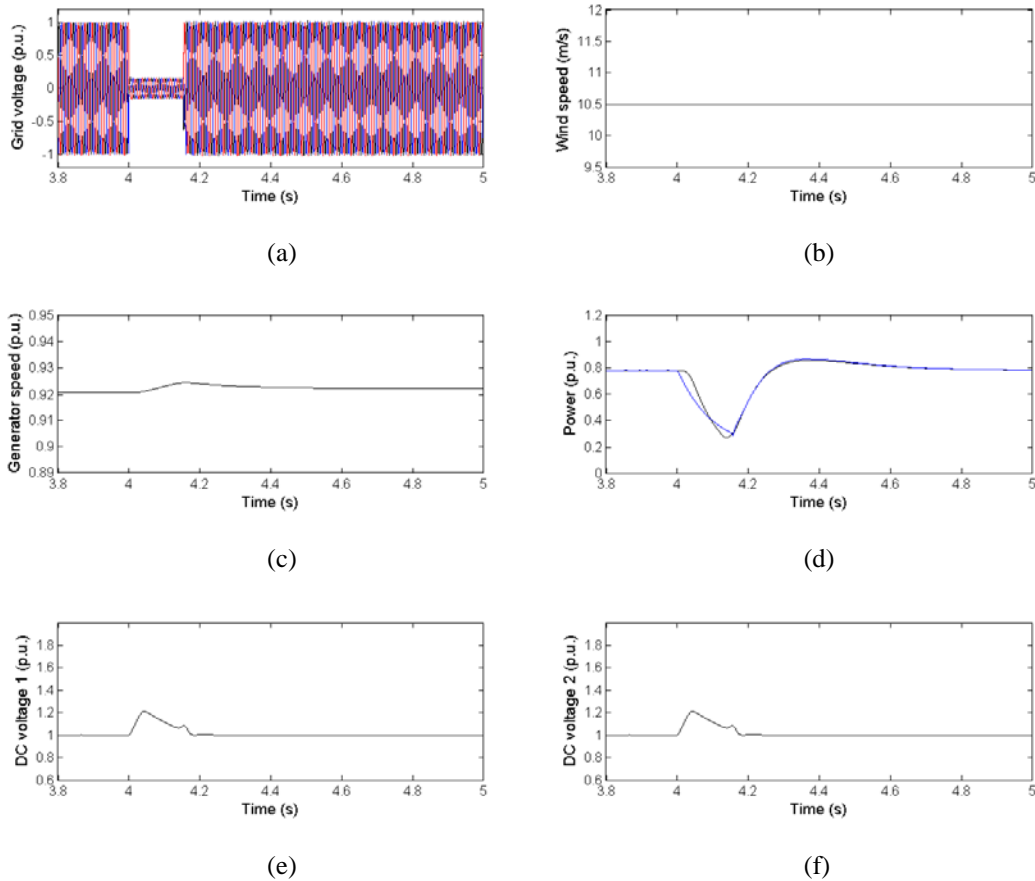


Fig. 2-27. Performance of the 10 MW wind turbine with the 4-segmented generator configuration under grid voltage dip situation without FRT control. (a) Grid voltage. (b) Wind speed. (c) Generator speed. (d) Generator power and grid power. (e) DC-link voltage Vdc1. (f) DC-link voltage Vdc2. (g) DC-link voltage Vdc3. (h) DC-link voltage Vdc4.

Fig. 2-28 shows the performance of the 10 MW wind turbine based on the 4-segmented generator under grid fault situation, where the FRT control is used here. Fig. 2-28(a) shows the grid voltage, where the grid voltage dips to a low value approximately 15% of the rated value and lasts for 150 ms. Figs. 2-28(b) and (c) show the wind speed and the generator speed, respectively. Fig. 2-28(d) shows the generator power (black curve) and the grid power (blue curve). During the fault period, the grid power is reduced owing to the grid voltage dips. With the FRT control, the generator power is also reduced, which can effectively limit the dc-link voltage of the power electronic converter. The two dc-link voltages in the two parallel power converters are both limited during the fault, as shown in Figs. 2-28e) and (f), which shows the effectiveness of the presented FRT control. The reduction of the generator power results in that more energy is stored in the kinetic energy and the wind turbine speed is slightly increased because of the large mass of the wind turbine, as shown in Fig. 2-28(c).



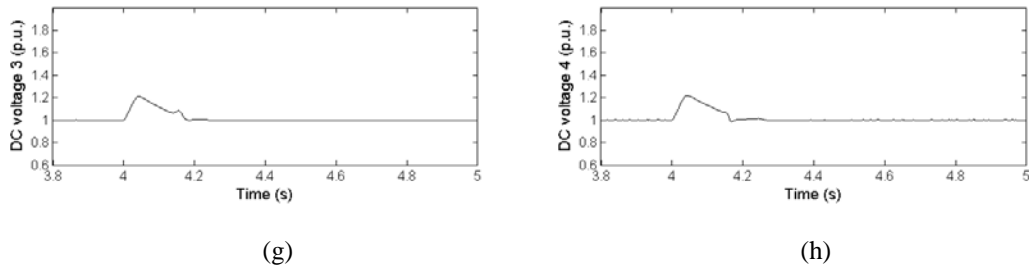


Fig. 2-28. Performance of the 10 MW wind turbine with the 4-segmented generator configuration under grid voltage dip situation with FRT control. (a) Grid voltage. (b) Wind speed. (c) Generator speed. (d) Generator power and grid power. (e) DC-link voltage Vdc1. (f) DC-link voltage Vdc2. (g) DC-link voltage Vdc3. (h) DC-link voltage Vdc4.

C. 20 MW wind turbine based on non-segmented generator

Fig. 2-29 shows the performance of the 20 MW wind turbine based on the single generator under grid fault situation, where the FRT control is not used here. Fig. 2-29(a) shows the grid voltage, where the grid voltage dips to a low value approximately 15% of the rated value and lasts for 150 ms. Fig. 2-29(b) and (c) shows the wind speed and the generator speed, respectively. Fig. 2-29(d) shows the generator power (black curve) and the grid power (blue curve). During the fault period, the generator is still controlled to follow the optimal power and the generator power is nearly unchanged. However, the grid power is reduced because the grid voltage dips. As a consequence, owing to the power unbalance between the generator power and the grid power, more power would be stored in the dc-link capacitor, which would result in the increase of the dc-link voltage. The two dc-link voltages in the two parallel power converters are both increased to a high value during the fault, as shown in Fig. 2-29(e) and (f).

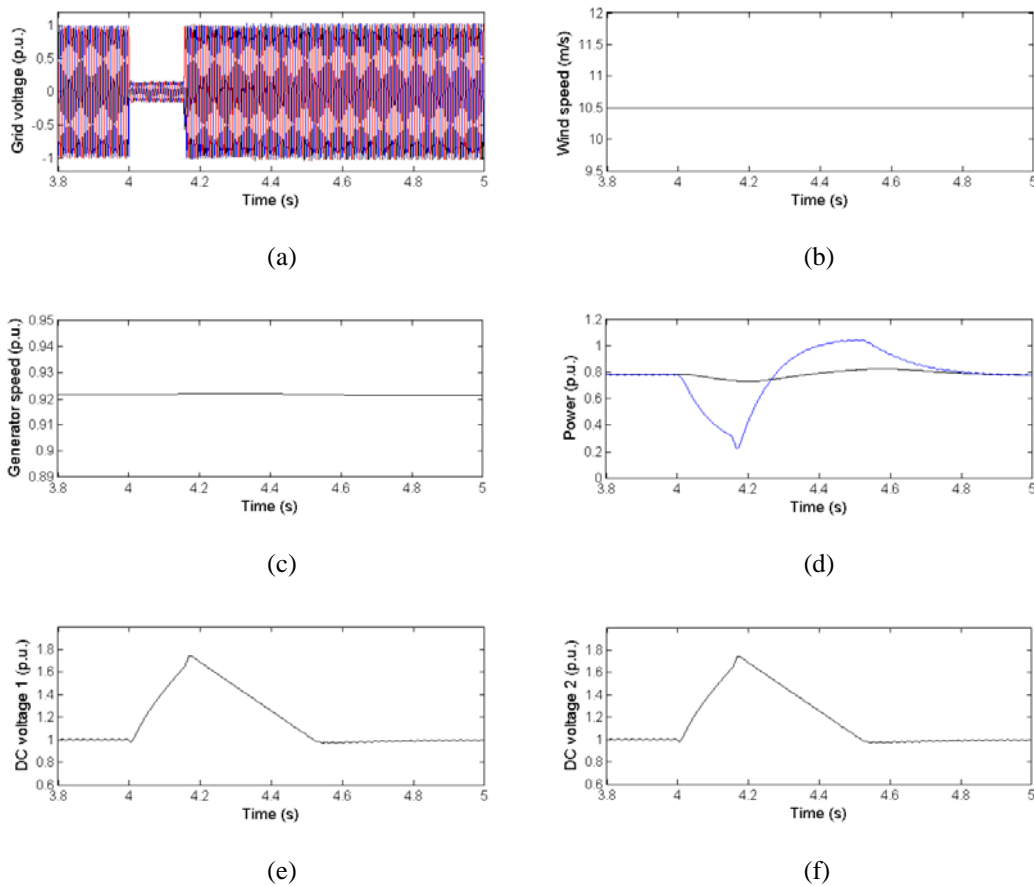


Fig. 2-29. Performance of the 20 MW wind turbine with the single generator configuration under grid voltage dip situation without FRT control. (a) Grid voltage. (b) Wind speed. (c) Generator speed. (d) Generator power and grid power. (e) DC-link voltage Vdc1. (f) DC-link voltage Vdc2.

Fig. 2-30 shows the performance of the 20 MW wind turbine based on the non-segmented generator under grid fault situation, where the FRT control is used here. Fig. 2-30(a) shows the grid voltage, where the grid voltage dips to a low value approximately 15% of the rated value and lasts for 150 ms. Fig. 2-30(b) and (c) shows the wind speed and the generator speed, respectively. Fig. 2-30(d) shows the generator power (black curve) and the grid power (blue curve). During the fault period, the grid power is reduced owing to the grid voltage dips. With the FRT control, the generator power is also reduced, which can effectively limit the dc-link voltage of the power electronic converter. The two dc-link voltages in the two parallel power converters are both limited during the fault, as shown in Fig. 2-30(e) and (f), which shows the effectiveness of the presented FRT control. On the other hand, owing to the reduction of the generator power, there will be more energy stored as kinetic energy. Consequently, it will result in the increase of the wind turbine speed. However, the wind turbine speed is just increased a little in the fault period, as shown in Fig. 2-30(c), because of the large mass of the wind turbine.

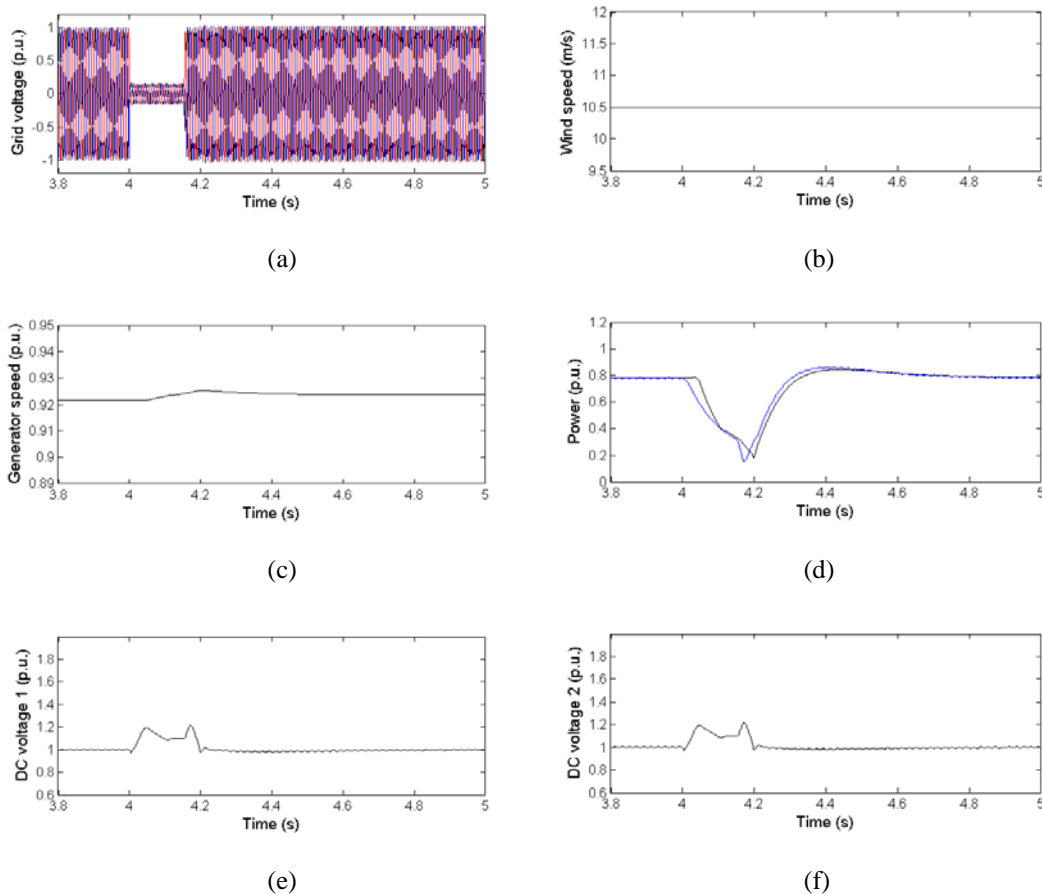


Fig. 2-30. Performance of the 20 MW wind turbine with the 4-segmented generator configuration under grid voltage dip situation with FRT control. (a) Grid voltage. (b) Wind speed. (c) Generator speed. (d) Generator power and grid power. (e) DC-link voltage Vdc1. (f) DC-link voltage Vdc2.

D. 20 MW wind turbine based on 4-segmented generator

Fig. 2-31 shows the performance of the 20 MW wind turbine based on the single generator under grid fault situation, where the FRT control is not used here. Fig. 2-31(a) shows the grid voltage,

where the grid voltage dips to a low value approximately 15% of the rated value and lasts for 150 ms. Fig. 2-31(b) and (c) shows the wind speed and the generator speed, respectively. Fig. 2-31(d) shows the generator power (black curve) and the grid power (blue curve). During the fault period, the generator is still controlled to follow the optimal power and the generator power is nearly unchanged. However, the grid power is reduced because the grid voltage dips. As a consequence, owing to the power unbalance between the generator power and the grid power, more power would be stored in the dc-link capacitor, which would result in the increase of the dc-link voltage. The two dc-link voltages in the two parallel power converters are both increased to a high value during the fault, as shown in Fig. 2-31(e) and (f).

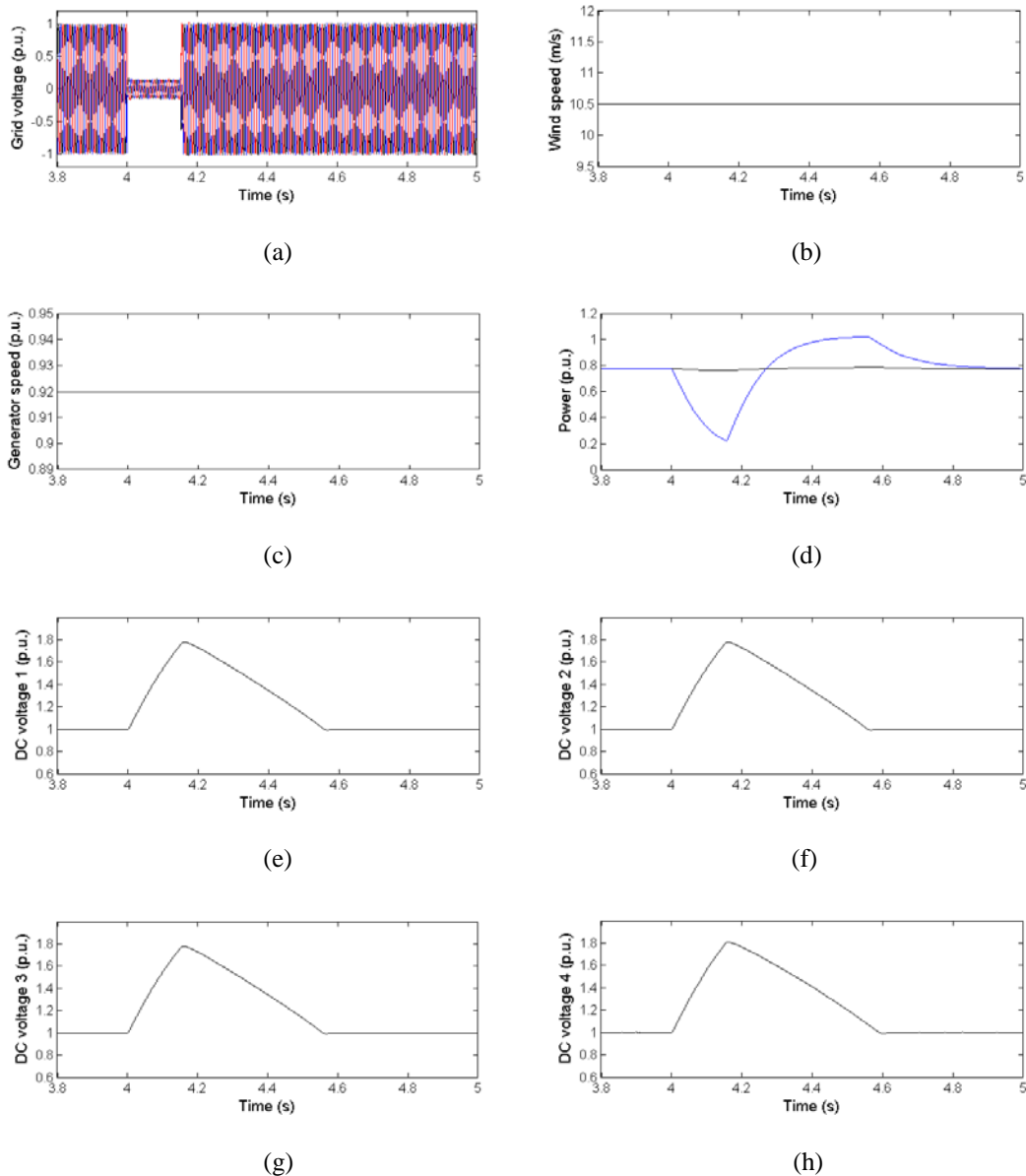


Fig. 2-31. Performance of the 20 MW wind turbine with the 4-segmented generator configuration under grid voltage dip situation without FRT control. (a) Grid voltage. (b) Wind speed. (c) Generator speed. (d) Generator power and grid power. (e) DC-link voltage Vdc1. (f) DC-link voltage Vdc2. (g) DC-link voltage Vdc3. (h) DC-link voltage Vdc4.

Fig. 2-32 shows the performance of the 20 MW wind turbine based on the non-segmented generator under grid fault situation, where the FRT control is used here. Fig. 2-32(a) shows the

grid voltage, where the grid voltage dips to a low value approximately 15% of the rated value and lasts for 150 ms. Fig. 2-32(b) and (c) shows the wind speed and the generator speed, respectively. Fig. 2-32(d) shows the generator power (black curve) and the grid power (blue curve). During the fault period, the grid power is reduced owing to the grid voltage dips. With the FRT control, the generator power is also reduced, which can effectively limit the dc-link voltage of the power electronic converter. The two dc-link voltages in the two parallel power converters are both limited during the fault, as shown in Fig. 2-32(e) and (f), which shows the effectiveness of the presented FRT control. On the other hand, owing to the reduction of the generator power, there will be more energy stored in the kinetic energy. Consequently, it will result in the increase of the wind turbine speed. However, the wind turbine speed is just increased a little in the fault period, as shown in Fig. 2-32(c), because of the large mass of the wind turbine.

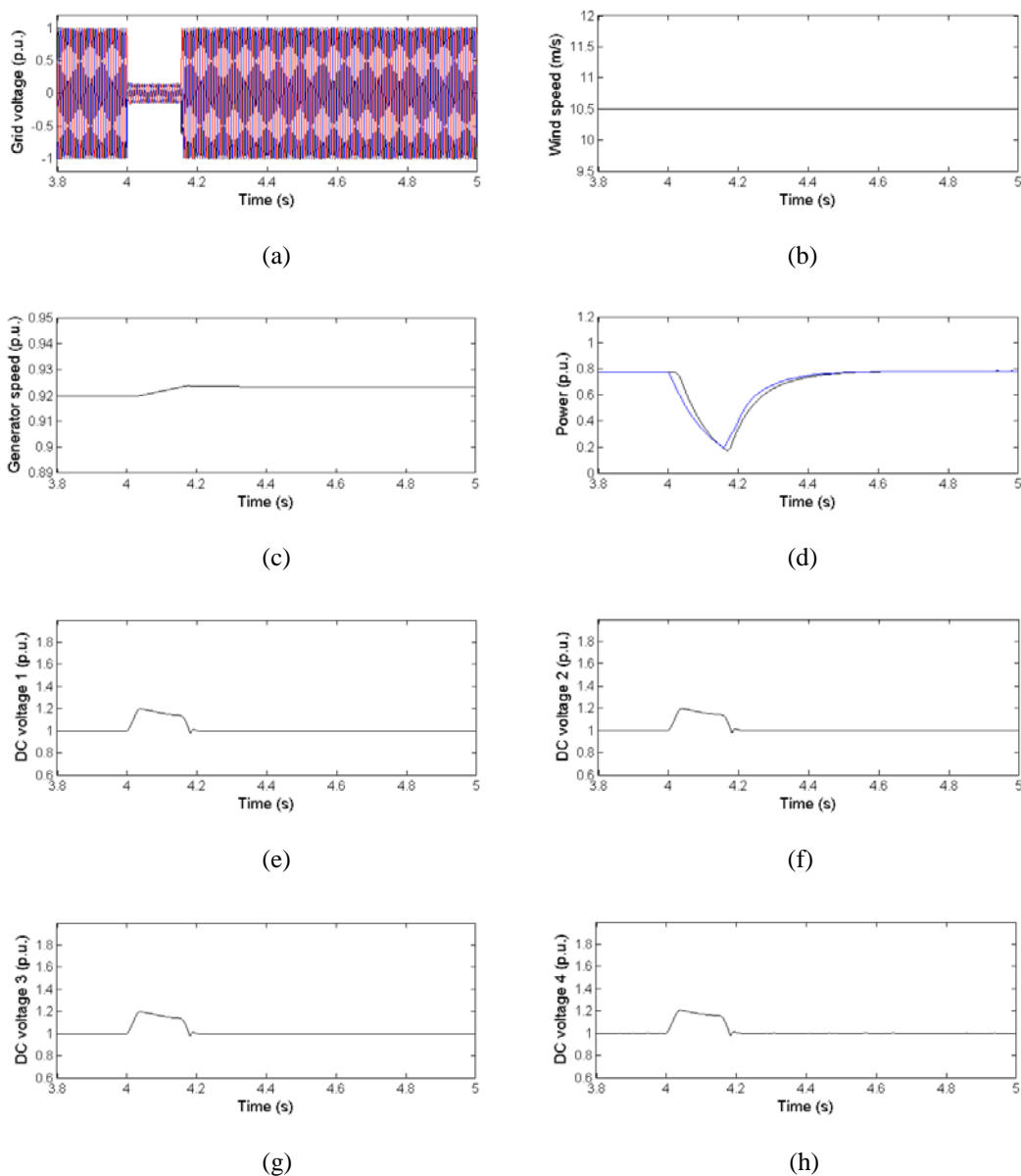


Fig. 2-32. Performance of the 20 MW wind turbine with the 4-segmented generator configuration under grid voltage dip situation with FRT control. (a) Grid voltage. (b) Wind speed. (c) Generator speed. (d) Generator power and grid power. (e) DC-link voltage Vdc1. (f) DC-link voltage Vdc2. (g) DC-link voltage Vdc3. (h) DC-link voltage Vdc4.

2.7.3 Case III: Circulating current control

A. 10 MW wind turbine based on non-segmented generator

Fig. 2-33 shows the performance of the 10 MW wind turbine based on single generator, as shown in Fig. 2-1, where the circulating current control is not used. Fig. 2-33(a) shows the generator stator current i_{abc_ge} . Figs. 2-33(b) and (c) show the generator-side converter current i_{abc_gep1} and i_{abc_gep2} of the two parallel converters. It can be seen that the circulating current appears in the converter i_{abc_gep1} and i_{abc_gep2} , as shown in Figs. 2-33(d) and (e), which does not flow into the generator.

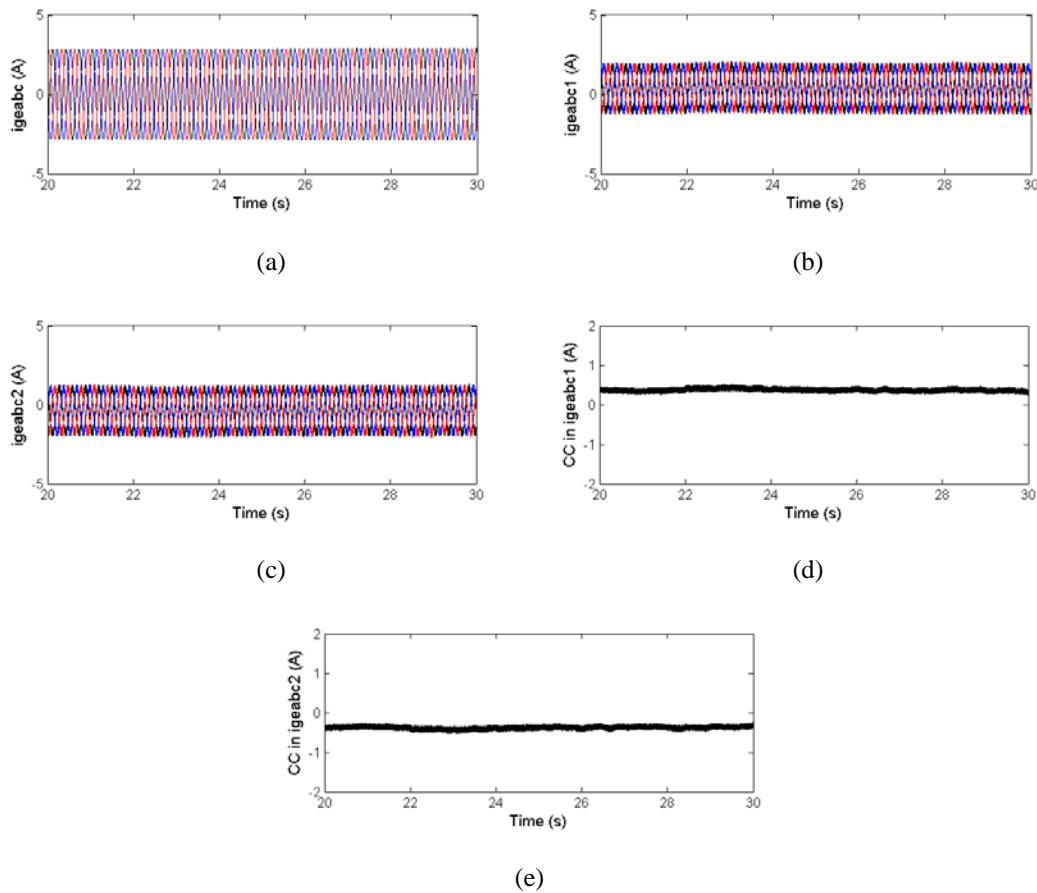


Fig. 2-33. Performance of the 10 MW wind turbine with the single generator configuration without CCC. (a) Generator stator three-phase current i_{abc_ge} . (b) Three-phase current i_{abc_gep1} of VSC1. (c) Three-phase current i_{abc_gep2} of VSC2. (d) Circulating current in i_{abc_gep1} . (e) Circulating current in i_{abc_gep2} .

Fig. 2-34 shows the performance of the 10 MW wind turbine based on single generator, where the circulating current control is used. Fig. 2-34(a) shows the generator stator current i_{abc_ge} . Figs. 2-34(b) and (c) show the generator-side converter current i_{abc_gep1} and i_{abc_gep2} of the two parallel converters. It can be seen that the circulating current in i_{abc_gep1} and i_{abc_gep2} are eliminated in the converter with the circulating current control, as shown in Figs. 2-34(d) and (e).

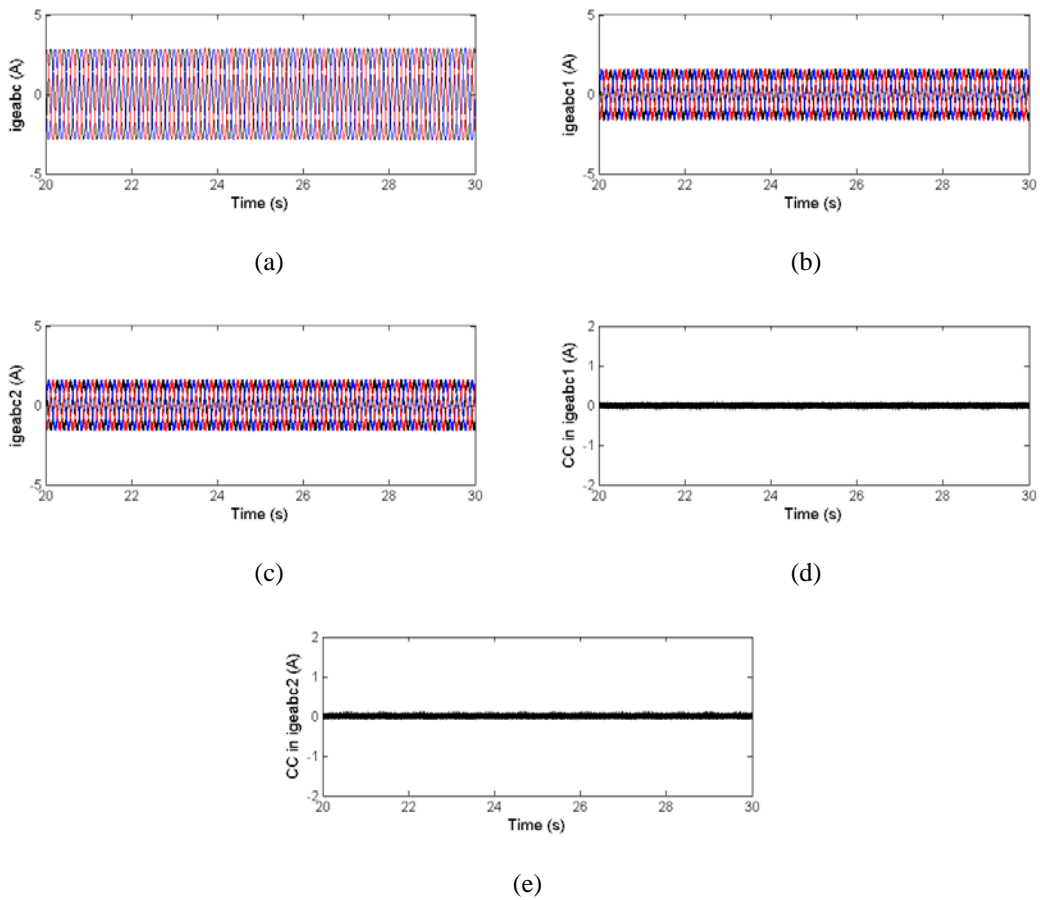
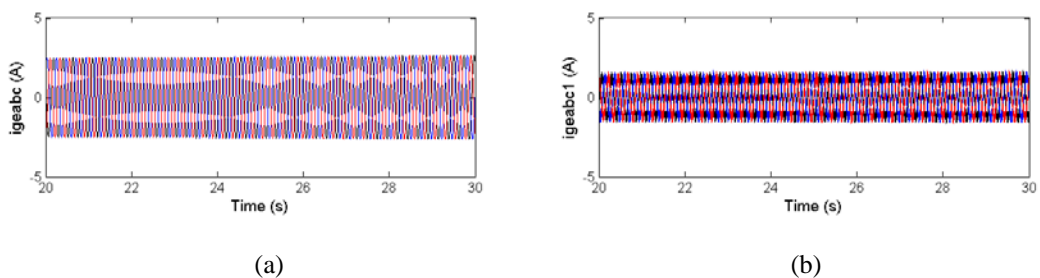


Fig. 2-34. Performance of the 10 MW wind turbine with the single generator configuration with CCC. (a) Generator stator three-phase current i_{abc_ge} . (b) Three-phase current i_{abc_gep1} of VSC1. (c) Three-phase current i_{abc_gep2} of VSC2. (d) Circulating current in i_{abc_gep1} . (e) Circulating current in i_{abc_gep2} .

B. 20 MW wind turbine based on non-segmented generator

Fig. 2-35 shows the performance of the 20 MW wind turbine based on single generator, as shown in Fig. 2-1, where the circulating current control is used. Fig. 2-35(a) shows the generator stator current i_{abc_ge} . Figs. 2-35(b) and (c) show the generator-side converter current i_{abc_gep1} and i_{abc_gep2} of the two parallel converters. It can be seen that the circulating current in i_{abc_gep1} and i_{abc_gep2} are eliminated in the converter with the circulating current control, as shown in Figs. 2-35(d) and (e).



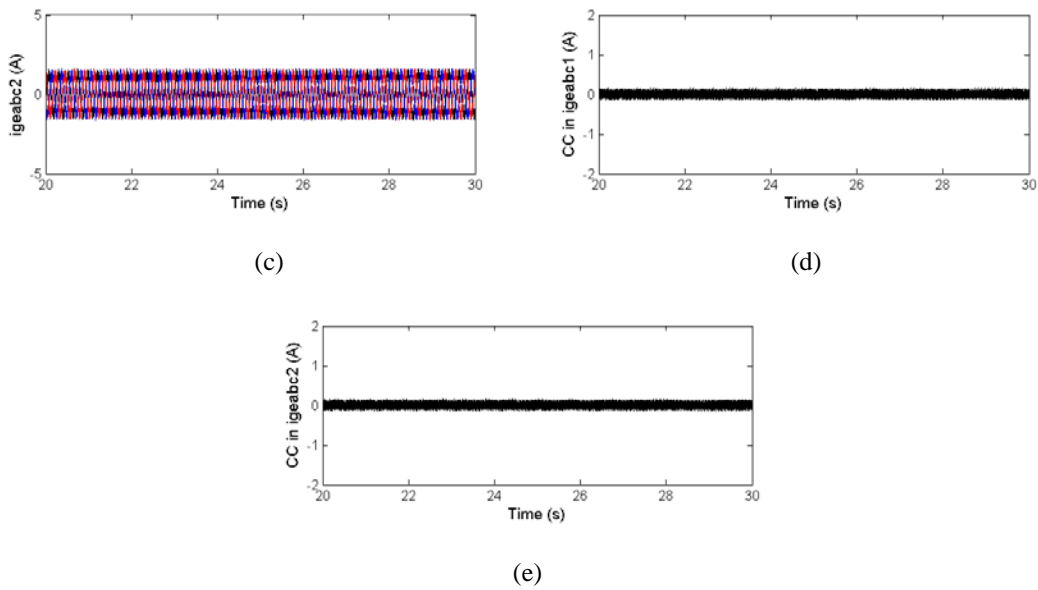


Fig. 2-35. Performance of the 20 MW wind turbine with the single generator configuration with CCC. (a) Generator stator three-phase current i_{abc_ge} . (b) Three-phase current i_{abc_gep1} of VSC1. (c) Three-phase current i_{abc_gep2} of VSC2. (d) Circulating current in i_{abc_gep1} . (e) Circulating current in i_{abc_gep2} .

2.8 Discussion and Conclusions

In this Section, the cost, size, efficiency, energy capture and cost of energy of the 10 and 20 MW wind turbine system contributed by the power electronic converters are discussed. The cost of the power converter system for the 20 MW wind turbine is less than double cost of that for the 10 MW wind turbine. The cost of the power converter for the 4-segmented generator is a little higher than that for the non-segmented generator in both 10 and 20 MW wind turbine. As to the 10 MW wind turbine, the size of the power converter for the 4-segmented generator is smaller than that for the non-segmented generator. As to the 20 MW wind turbine, the size of the power converter for the 4-segmented generator is bigger than that for the non-segmented generator. In both the 10 and 20 MW wind turbines, the weight of the power converter for the non-segmented generator is lighter than that for the 4-segmented generator. The power converter efficiency of the 10 and 20 MW wind turbine are similar. The AOE of the 20 MW wind turbine is almost double of that of the 10 MW wind turbine system. The CoE of the 10 MW wind turbine based on 4-segmented generator is the highest and the CoE of the 20 MW wind turbine based on non-segmented generator is the lowest. In addition, the related control for the wind turbine under normal situation and fault situation is presented. The simulation studies have been conducted and the results verify the presented control. No major challenges are identified for the power electronic system connecting SCG to grid.

2.9 Appendix

The 10 and 20 MW wind turbine system parameters for simulation studies are shown in Table 2-17.

Table 2-17
10 and 20 MW Wind Turbine Parameters for Simulations [2-10]

Wind turbine parameter	Value	Value
Wind turbine rated power (MW)	10	20
Rotor diameter (m)	178	252
Hub height	119	153
Cut in wind speed (m/s)	4	4
Nominal wind speed (m/s)	11.4	11.4
Cut out wind speed (m/s)	25	25

2.10 References

- [2-1] B. Wu, Y. Lang, N. Zargari, and S. Kouro, *Power Conversion and Control of Wind Energy System*, Wiley 2011.
- [2-2] B. Backlund, M. Rahimo, S. Klaka, J. Siefken, "Topologies, voltage ratings and state of the art high power semiconductor devices for medium voltage wind energy conversion," in *proceeding on PEMWA*, 2009, pp. 1-6.
- [2-3] <http://new.abb.com/semiconductors/integrated-gate-commutated-thyristors-igct>
- [2-4] X. Zeng, Z. Chen, and F. Blaabjerg, "Design and comparison of full-size converters for large variable-speed wind turbines," in *proceeding on European Conference on Power Electronics and Applications 2007*, pp. 1-10.
- [2-5] X. Wei, L. Xiao, Z. Yao, and C. Gong, "Design of LCL filter for wind power inverter," in *proceeding on WNWEC*, 2010, pp. 1-6.
- [2-6] <http://eu.mouser.com/>
- [2-7] ABB. PCS 6000 for large wind turbines medium voltage, full power converters up to 9 MVA
- [2-8] PSCAD, [Online available] <https://hvdc.ca/pscad/>
- [2-9] D. Graovac and M. Purschel, *IGBT Power Losses Calculation Using the Data-sheet Parameters*, Infineon Technologies AG, 2009.
- [2-10] INN WIND D1.21 report. Reference Wind Turbine Report.
- [2-11] Chee-Mun Ong, *Dynamic Simulation of Electric Machinery Using Matlab/Simulink*. New Jersey: Prentice Hall PTR, 1998, Chap. 7.
- [2-12] Valtchev V., Bossche A., Ghijselen J., Melkebeek J.: 'Autonomous renewable energy conversion system', *Renew. Energy*, 2000, 19, (1), pp.259-275

- [2-13] Sun Tao, Chen Zhe, Blaabjerg F “Flicker Study on Variable Speed Wind Turbines with Doubly Fed Induction Generators,” *IEEE Transactions on Energy Conversion*, vol. 20, no. 4, pp. 896–905, 2005.
- [2-14] Z. Xu, R. Li, H. Zhu, D. Xu, and C. H. Zhang, “Control of parallel multiple converters for direct-drive permanent-magnet wind power generation systems,” *IEEE Transactions on Power Electronics*, vol. 27, no. 3, pp. 1259-1270, Mar. 2012.
- [2-15] F. Deng and Z. Chen, “Operation and control of a dc-grid offshore wind farm under dc transmission system faults,” *IEEE Transactions on Power Delivery*, vol. 28, no. 3, pp. 1356-1363, Jul. 2013.
- [2-16] S. Mali, S. James, and I. Tank, “Improving low voltage ride-through capability for grid connected wind turbine generator,” in *Proc. 4th International Conference on Advances in Energy Research*, 2013, pp. 530-540.
- [2-17] Z. Wu, X. Dou, J. Chu, and M. Hu, “Operation and control of a direct-driven PMSG-based wind turbine system with an auxiliary parallel grid-side converter,” *Energy*, pp. 3405-3421, 2013.

3 VOLTAGE SOURCE CONVERTER DESIGN TAILORED TO PDDG

3.1 Introduction

This chapter focuses on converter designs for 10 MW and 20 MW magnetic pseudo direct drive (PDD) generators. From the converter point of view, the PDD behaves like a permanent magnet synchronous machine. Originally, the converter design tailored for the PDD should have been based on the results of D3.32 (a design scenario in D3.32 was chosen with regard to the PDD parameters). Due to the possibility to divide the PDD in different segments, which was not considered for D3.32, new converter topologies are possible and must be discussed at first.

3.2 Topologies for the PDDG

In D3.32, the parallel 3-level neutral point clamped (NPC) voltage source inverter (VSI) and the current source inverter (CSI) with a modular multilevel active filter were the most promising solutions. Both approaches are also adaptable to a segmented generator. Besides, the segmentation makes multiple other topologies possible which have not been considered yet.

This section presents the resulting new converter choices for a segmented PDD generator. At first, the main topologies from D3.32 (and small variations of them) are adapted for a segmented generator:

- Parallel 3-level NPC VSI in back-to-back configuration:

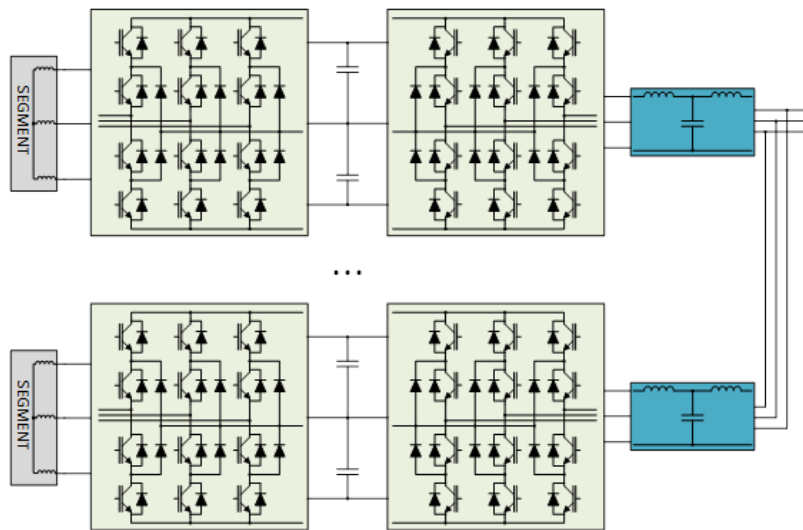


Figure 3-1: Parallel 3-level NPC VSI in back-to-back configuration.

The approach is similar to parallel NPC VSI, but here each NPC VSI is connected to one segment for the PDD generator. The number of segments and the resulting voltage and current levels are important, because they determine if standard components can be used.

- Modular Multilevel Converter (MMC) in back-to-back configuration:

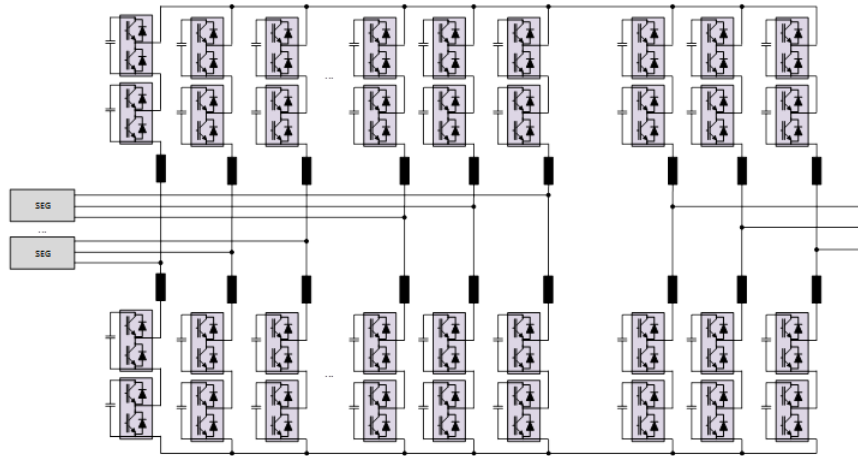


Figure 3-2: MMC in back-to-back configuration.

This is the adaption of the modular multilevel converter from D3.32 to a segmented generator. The numbers of branches and modules are very high, especially with a high number of segments. Additionally, the grid side MMC uses different modules than the generator side MMCs. The main advantage of this topology is a high availability with redundant modules at cost of a high complexity.

- Modular Multilevel Matrix Converter (MMMC):

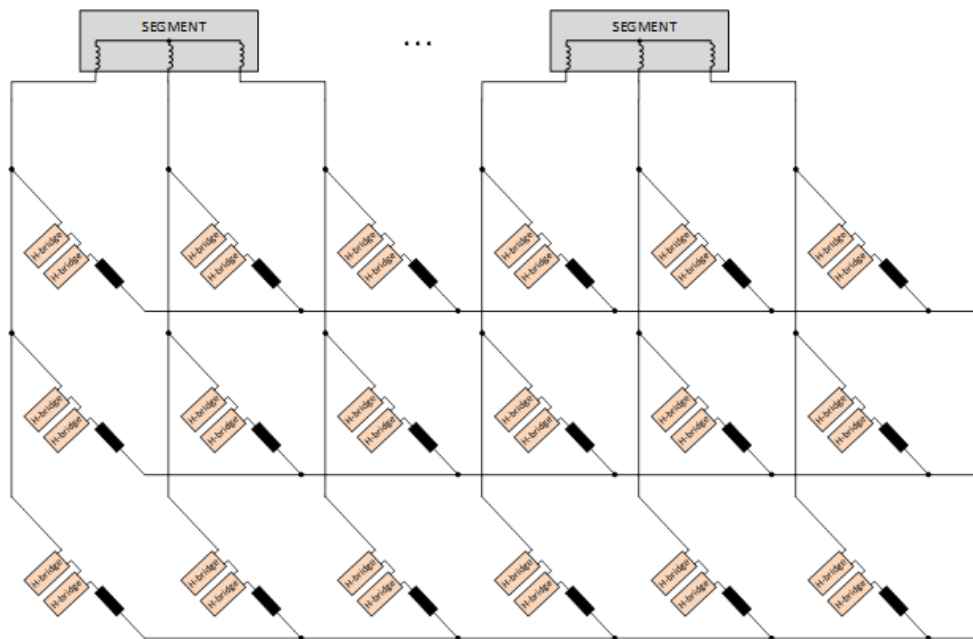


Figure 3-3: MMMC.

Each segment uses an MMMC, which are connected in parallel. Due to segmentation, the numbers of branches and modules are even higher than for the MMC. With redundant modules the availability is also high. However, the complexity of the system is very high as well.

- Parallel CSI with modular multilevel active filter:

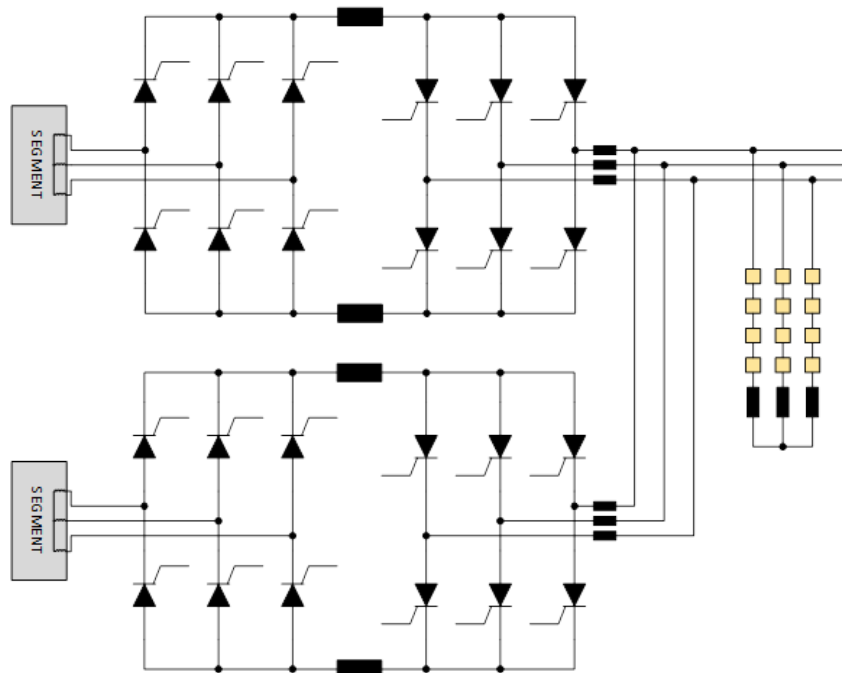


Figure 3-4: Parallel CSI with modular multilevel active filter.

The parallel connected CSI can share one modular multilevel filter at the grid side. The active filter at the generator side used in D3.32 is not necessary for the operation of the PDD generator.

It can be seen that the adaption of the converter concepts from D3.32 to a segmented generator leads to no major changes of the topologies' advantages/disadvantages. Only the use of one active filter for all parallel CSI can be pointed out. Accordingly, the general tendency of the converter comparison in D3.32 should be also valid for a segmented PDD.

Besides, the segmentation of the generator makes additional topologies possible:

- Parallel 2-level VSI in back-to-back configuration:

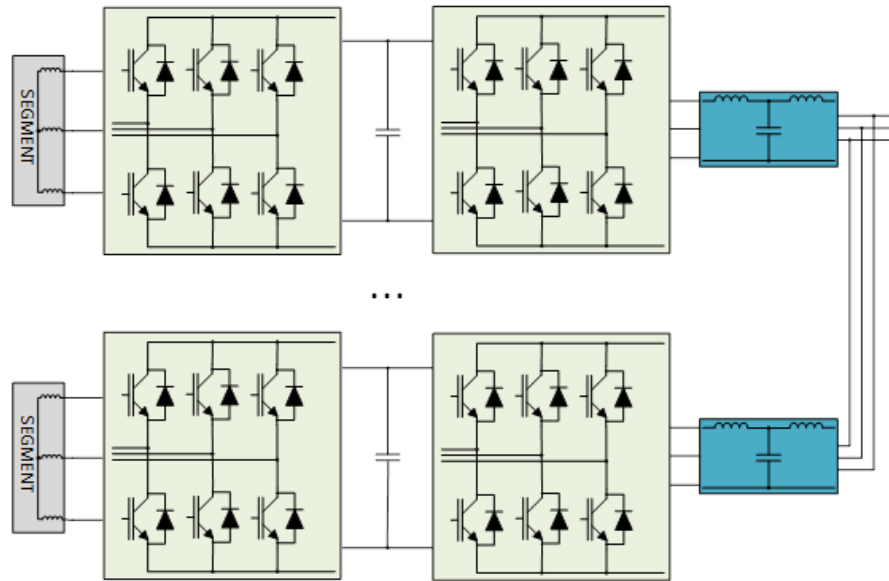


Figure 3-5: Parallel 2-level VSI in back-to-back configuration.

The only change to the parallel 3-level NPC VSI approach is the use of 2-level VSI instead of 3-level NPC VSI. This solution should only be considered if there is a high number of segments and a low segment voltage (for avoiding parallel and/or serial IGBTs). The low voltage level of the segments would lead to very high sum of the output currents and thus to very high currents for the grid connection transformer.

- 2-level (or 3-level NPC) VSI per segment connected in series combined with a 3-level NPC VSI on grid-side:

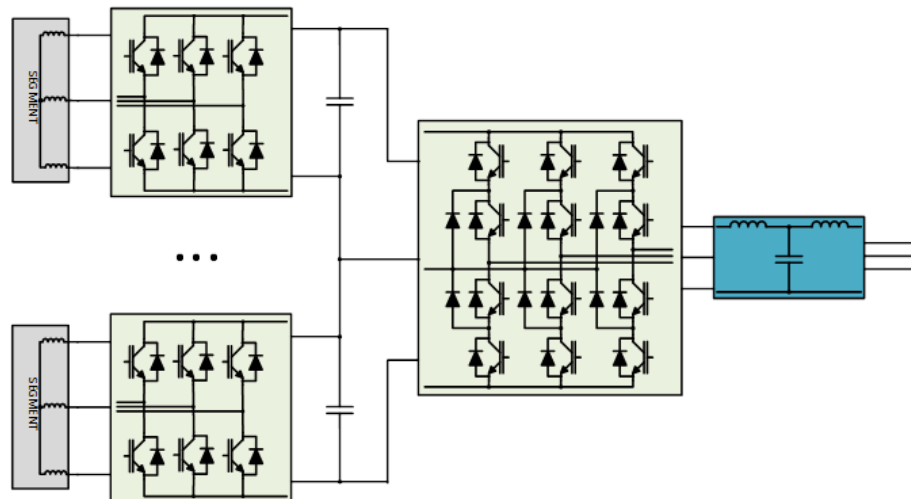


Figure 3-6: 2-level (or 3-level NPC) VSI per segment connected in series combined with a 3-level NPC VSI on grid-side.

For this topology, the number of segments in combination with the maximum segment voltage is limited by the NPC VSI voltage rating and the available IGBTs. Additionally, the handling of an error at the generator side VSI is problematic. The isolation of the segments against ground results from the 3-level NPC VSI voltage because the generator side VSIs of the segments are floating.

- 2-level (or 3-level NPC) VSI per segment connected in series combined with a MMC on grid-side:

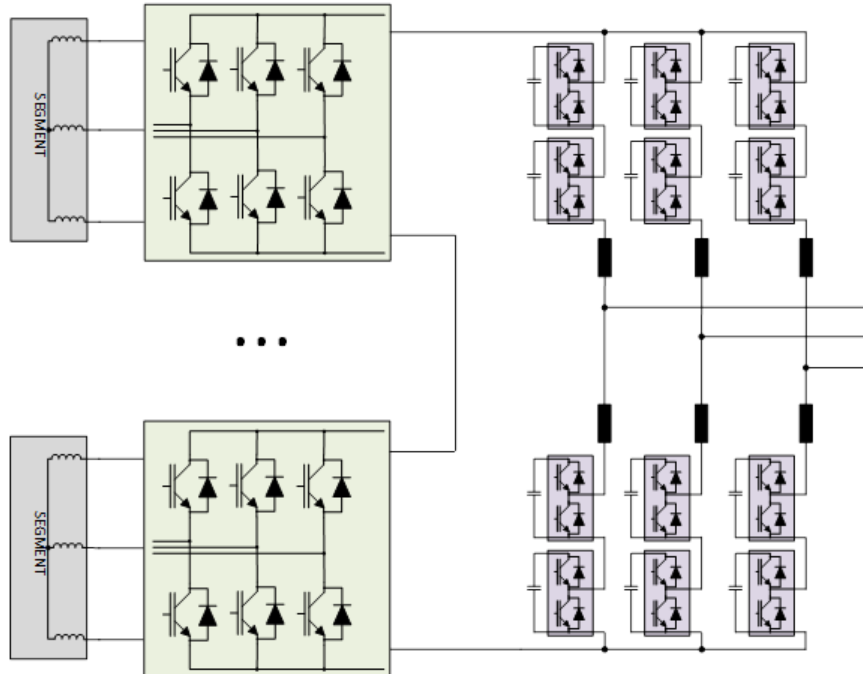


Figure 3-7: 2-level (or 3-level NPC) VSI per segment connected in series combined with a MMC on grid-side.

Compared to the prior topology, there is no restriction for the number of segments and the segment voltage by the grid-side, because of the modularity of the MMC. Even a direct connection to the medium voltage grid without transformer is thinkable. However, the isolation of the segments against ground is dictated by the grid voltage, which cancels this advantage. In addition, the handling of an error at the generator side VSIs is problematic as well.

- 2-level VSI per segment connected as a cascaded H-bridge converter (CHB) on grid-side:

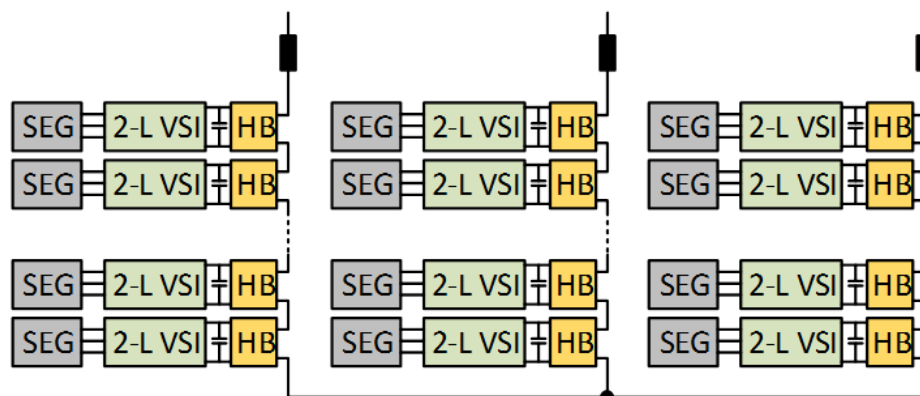


Figure 3-8: 2-level VSI per segment connected as a cascaded H-bridge converter (CHB) on grid-side.

The connection of the segments as a CHB is only suitable for a higher number of segments. Depending on the segment number and voltage a connection to the grid without transformer would be possible. But again, the isolation of the segments against ground is dictated by the grid voltage. Additionally, it is not possible to use redundant

modules in the branches of the CHB, because there are no “redundant segments”. As a result, the availability of the converter is a problem, because a high number of devices is used without redundancy.

In conclusion, none of the additional topologies offers significant advantages. Instead, the isolation between the segments and ground as well as fault handling is a problem for some of them.

Accordingly, the results from D3.32 showing the parallel 3-level NPC and the CSI with modular multilevel active filter seem to be valid, even under consideration of the possibility to segment the generator. In the past, the trend of market and technical community clearly points from CSI to VSI concepts. Therefore, the authors of this chapter choose the parallel 3-level NPC (Figure 3-9) instead of the CSI with modular multilevel active filter as topology for the PDD topology. Nevertheless, due to the good performance of the CSI in D3.32, this topology is further investigated for the PDD in Chapter 4.

For the 10 MW PDD with 3.3 kV parallel 3-level NPC VSI and no segmentation of the generator are chosen. The segmentation would not offer significant advantages (and even reduces the fault tolerance) for the NPC VSI and is not needed from the generator point of view. However, for the 20 MW PDD with 6.6 kV parallel 3-level NPC VSIs are used with a generator divided into two segments. Each of the segments only has a voltage of 3.3 kV, which makes the power electronic components for the 10 MW PDD and the 20 MW PDD similar (besides different nominal generator frequency and changes in current harmonic requirements on the grid-side). This reduction from 6.6 kV to 3.3 kV avoids the use of serial connected IGBTs due to high blocking voltage requirements. Because each segment uses parallel NPC VSIs fault tolerance is still given for the 20 MW converter. The resulting Parameters of the 10 MW PDD and the 20 MW PDD are given in Table 3-1.

Table 3-1
10 MW and 20 MW PDD generator parameters

Nominal active power	10 MW	20 MW
Segmentation	None	Two Segments
Nominal active power per segment	10 MW	10 MW
Nominal generator line-to-line voltage RMS per segment	3.3 kV	3.3 kV
Electrical frequency at nominal operation	48.25 Hz	34.1 Hz
Self-inductance per phase and segment	1.21 mH	1.79 mH
Mutual inductance per phase and segment	-0.57 mH	-0.82 mH
Resistance per phase and segment	3.94 mΩ	4.43 mΩ

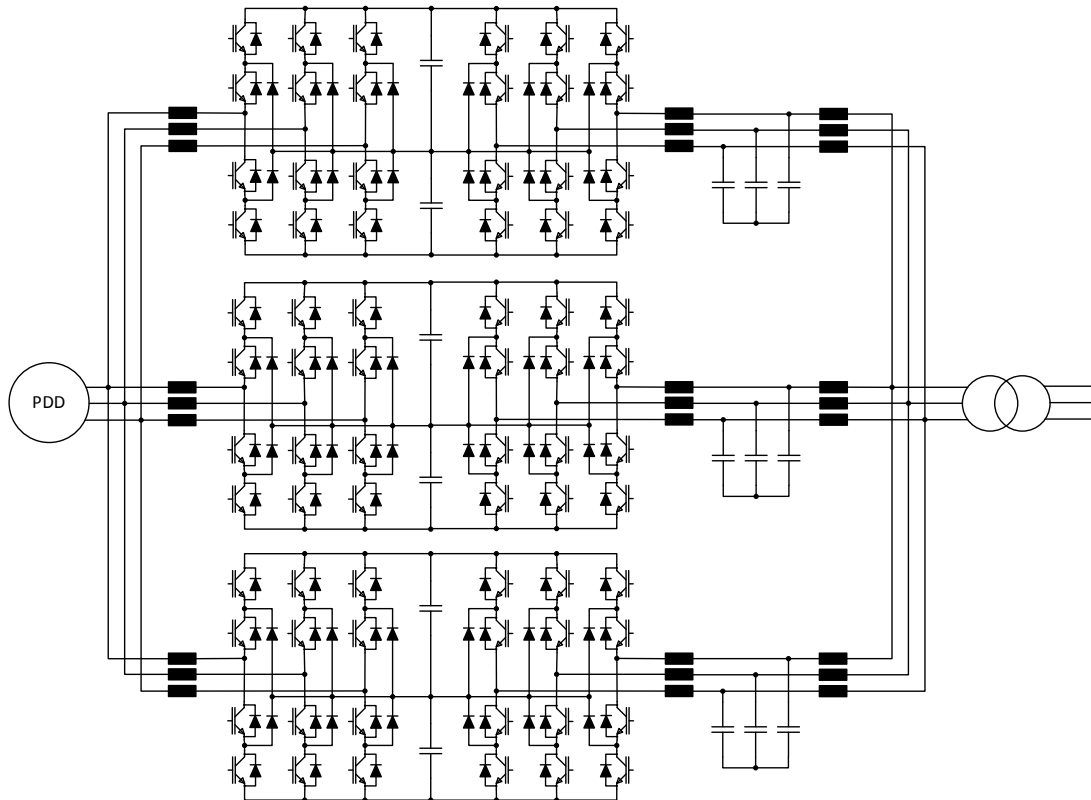


Figure 3-9: Three parallel 3-level NPC converter in back-to-back configuration for the 10 MW PDD (or one of the 20 MW PDD segments).

3.3 Component Design for Neutral Pointed Clamped Converter

This section presents the NPC VSI component design for the 10 MW and 20 MW PDD generators. Each subsection discusses the respective component for the 10 MW PDD and for the 20 MW PDD.

3.3.1 DC Link Capacitor Design

The minimum required DC link voltage for 3.3 kV line to line RMS voltage using space-vector modulation is

$$V_{DC,min} = \frac{2}{3} \cdot 3300 \text{ V} / 1.155 \approx 4666 \text{ V} . \quad (3-1)$$

Due to DC link voltage variations and additional voltage reserve for control, a safety factor of 20 % is used:

$$V_{DC} = 1.2 \cdot V_{DC,min} \approx 5600 \text{ V} . \quad (3-2)$$

The critical criterion for designing the DC link capacitors is the variation of the DC link's neutral point potential. This variation is restricted to 10 % of the DC link voltage. The maximum energy variation in the DC link capacitors is numerically calculated considering the influence of the generator side currents and grid side currents in different operating point. The necessary capacitor resulting from this maximum energy variation is

$$C_{DC,1} = C_{DC,2} = 6.5 \text{ mF} \quad (3-3)$$

for the converters of the 10 MW PDD generator and

$$C_{DC,1} = C_{DC,2} = 6.5 \text{ mF} \quad (3-4)$$

for the converters of the 20 MW PDD generator, with $C_{DC,1}$ and $C_{DC,2}$ being the upper and lower DC link capacitors.

The device DCP6K07119EP00KS0F (700 V DC, 1190 μF , [3-1]) is chosen for representing the DC link capacitor in Figure 3-10. With the given maximum DC voltage of the device, four DCP6K07119EP00KS0F have to be connected in series. To achieve the wanted total capacitance, 22 DCP6K07119EP00KS0F must be connected in parallel for the 10 MW PDD converters and for the 20 MW PDD converters. This results in the total number of DCP6K07119EP00KS0F devices used:

$$n_{\text{devices}} = 2 \cdot n_{\text{series}} \cdot n_{\text{parallel}} = 176 \quad (3-5)$$

for each of the 10 MW PDD converters and

$$n_{\text{devices}} = 2 \cdot n_{\text{series}} \cdot n_{\text{parallel}} = 176 \quad (3-6)$$

for each of the 20 MW PDD converters.

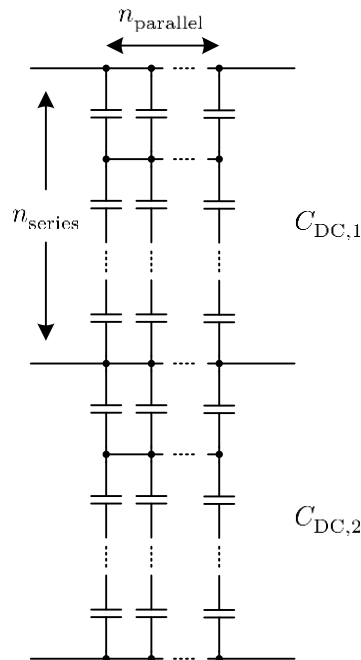


Figure 3-10: Series and parallel connection of devices for DC link capacitor.

3.3.2 Semiconductor Choice

For the 3-level NPC VSI the maximum blocking voltage of a single switch is

$$V_{\text{block}} = \frac{V_{\text{DC}}}{2} \quad (3-7)$$

Considering voltage overshoot and failure rates due to cosmic rays [3-2], IGBTs with 4.5 kV blocking voltage are used. Looking for example at ABB HiPak IGBTs with 4.5 kV blocking voltage, there are single IGBTs available with 650 A, 800 A, and 1200 A current rating. For the clamping diodes, for example Mitsubishi Diode half bridge modules with 4.5 kV blocking voltage and 300 A, 400 A, 800 A, and 1200 A rated current can be used. For the first choice of the current rating, the possible maximum currents are considered. Depending on the number of parallel NPC VSIs n_p , the maximum phase current of a converter for a 10 MW, 3.3 kV generator (or segment) is

$$\hat{i} = \sqrt{\frac{2}{3}} \cdot \frac{P}{n_p \cdot U_{ll,rms} \cdot \cos(\varphi)} \quad (3-8)$$

With the power factor of the PDD at nominal operation being about $\cos(\varphi) = 0.95$, the maximum converter currents for $n_p = 1, 2, 3, 4$ are $\hat{i} = 2604 \text{ A}, 1302 \text{ A}, 868 \text{ A}, 651 \text{ A}$. This makes two, three, and four parallel converters candidates for the available current ratings. As a compromise between fault tolerance and cost, three parallel converters with 4.5 kV, 800 A IGBTs were chosen as first candidate.

The carrier frequency (twice the switching frequency for 3-level NPC VSI switches) is determined by a thermal simulation of a single NPC VSI leg. Based on an ideal phase current and a sinusoidal set point curve for the modulation index, the conducting and switching losses of the IGBTs are calculated using datasheet values for the devices [3-3]~[3-6]. The baseplates of all devices are assumed to be constant at 90 °C as a worst case scenario. Aiming for a maximum junction temperature of 125 °C the maximum carrier frequency for the grid-side is approximately 300 Hz for this first candidate of devices. The results for the generator side with the only slightly lower frequency of 48.25 Hz and the different current direction showed that the generator side converter would have to use a carrier frequency lower than or equal to 150 Hz for this first candidate of devices.

As a consequence of the low possible carrier frequency, 4.5 kV, 1200 A IGBTs in combination with 4.5 kV, 800 A clamping diodes are chosen instead. Thermal simulations for these showed, that a maximum carrier frequency

$$f_{\text{carrier}} = 750 \text{ Hz} \quad (3-9)$$

is possible for generator side converters and grid side converters. The grid side results of the thermal simulation with an initial junction temperature $T_{j,0} = 90 \text{ °C}$ are presented in Figure 3-12. As expected, the temperatures of IGBT 1 and IGBT 4 are critical for the design (numbering of devices is given in Figure 3-11).

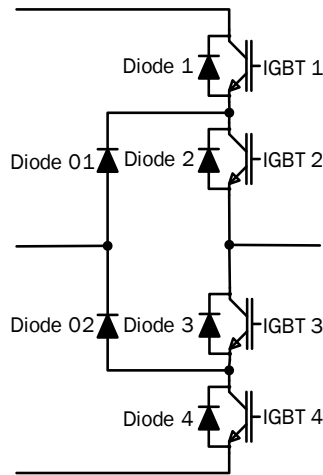


Figure 3-11: Device numbering for a single 3-level NPC converter leg.

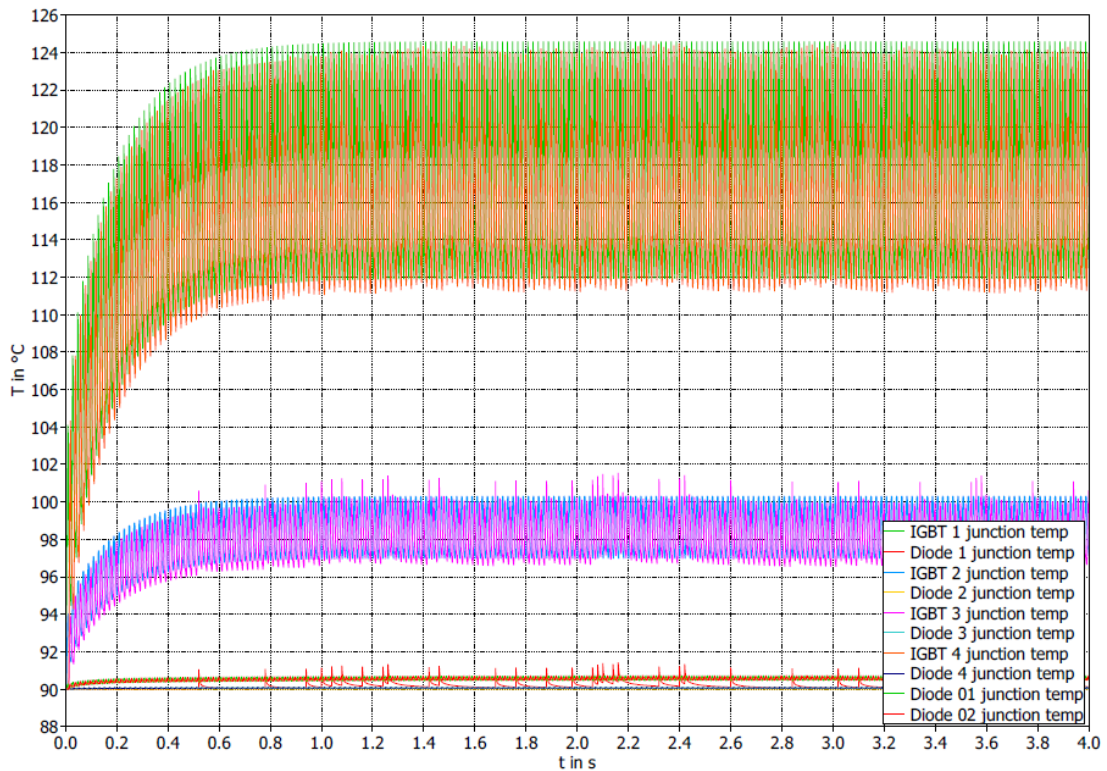


Figure 3-12: Thermal simulation results for grid side converters with 4.5 kV, 1200 A IGBTs, 4.5 kV, 800 A clamping diodes, and 750 Hz carrier frequency. Operation at maximum active and reactive power with duty cycle $m=1.15$.

With the same carrier frequency for the generator-side, the thermal simulation of the generator-side results in Figure 3-13. In contrast to the grid-side, this time the temperature of the freewheeling diode of IGBT 1 and IGBT 4 are critical for the design.

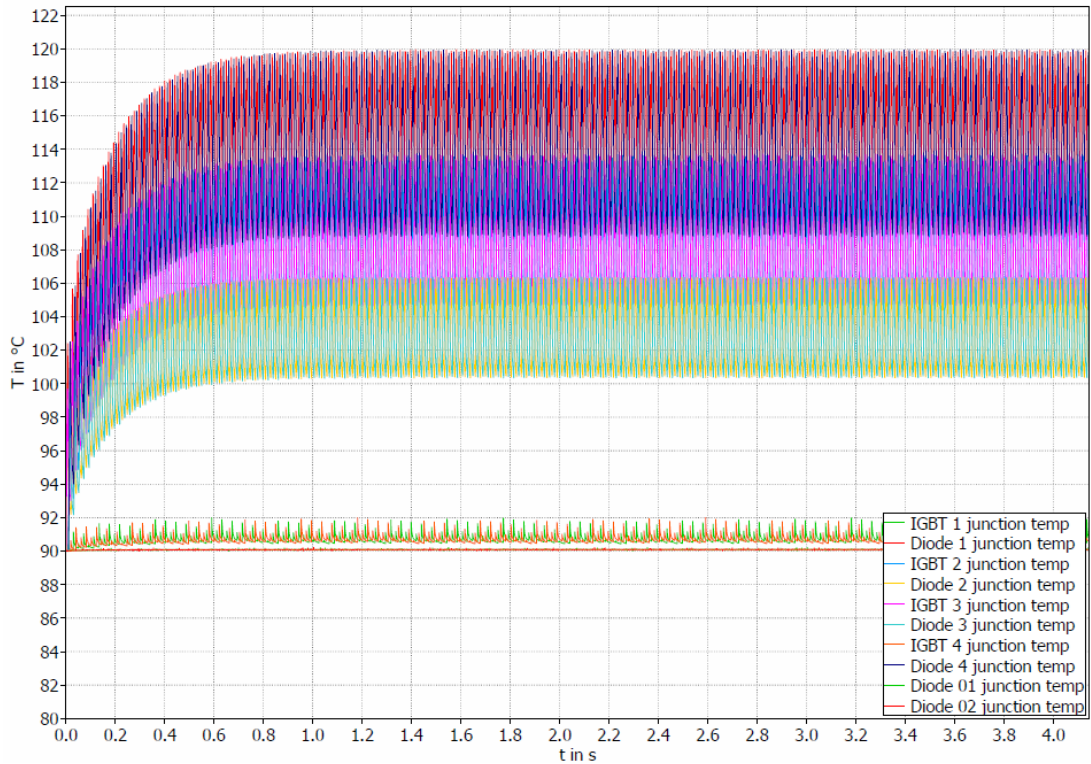


Figure 3-13: Thermal simulation results for generator side converters (10 MW PDD) with 4.5 kV, 1200 A IGBTs, 4.5 kV, 800 A clamping diodes, and 750 Hz carrier frequency. Operation at maximum active and reactive power with duty cycle $m=1.15$.

Due to the different nominal generator frequency of 34.1 Hz for the 20 MW PDD generator, the thermal simulation is repeated and the results are shown in Figure 3-14. Again, $f_{\text{carrier}} = 750 \text{ Hz}$ will be used as carrier frequency.

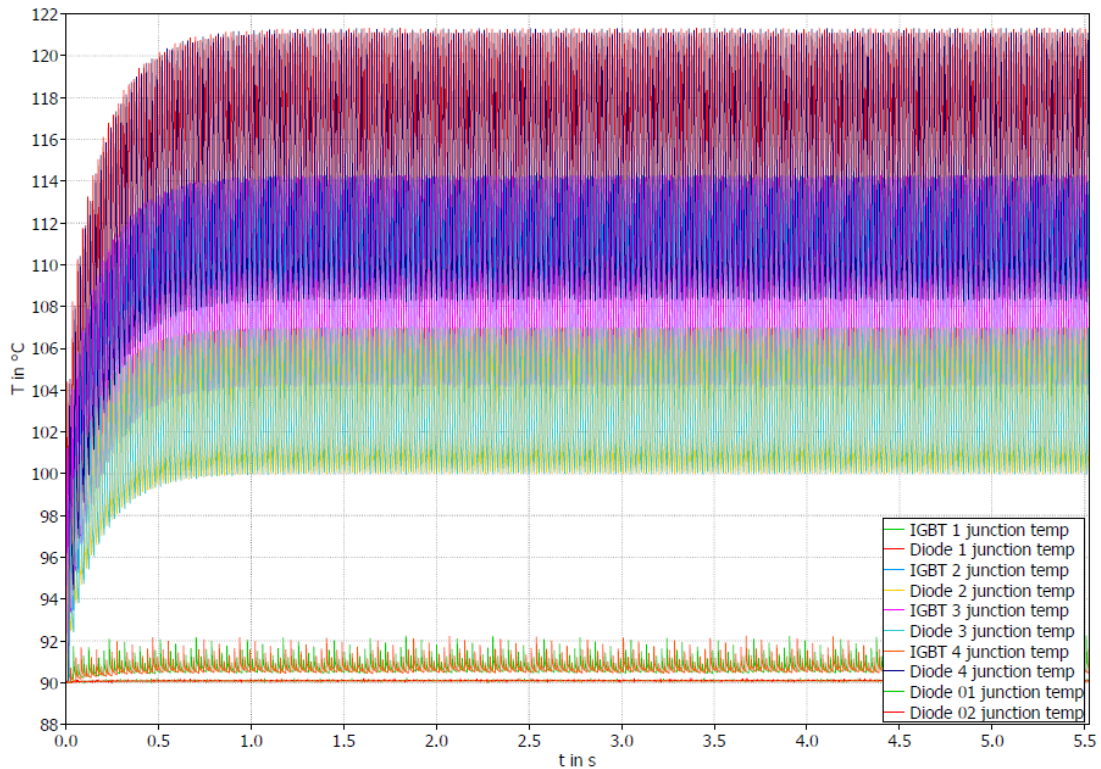


Figure 3-14: Thermal simulation results for generator side converters (20 MW PDD) with 4.5 kV, 1200 A IGBTs, 4.5 kV, 800 A clamping diodes, and 750 Hz carrier frequency. Operation at maximum active and reactive power with duty cycle $m=1.15$.

For a real design, the junction temperature variation and the resulting lifetime considerations would be investigated as well, but they are not considered for choosing the switching frequency in this report.

3.3.3 Grid Filter Design

For the grid side filter, a sinusoidal filter for each of the parallel connected converters is used, as presented in Figure 3-15. The design of the grid side filter is done with the method described in [3-7] and [3-8] assuming the current harmonic restrictions from [3-9]. For modulation, an asymmetrical regular sampled (ASR) PWM with phase disposition (PD) carriers is used.

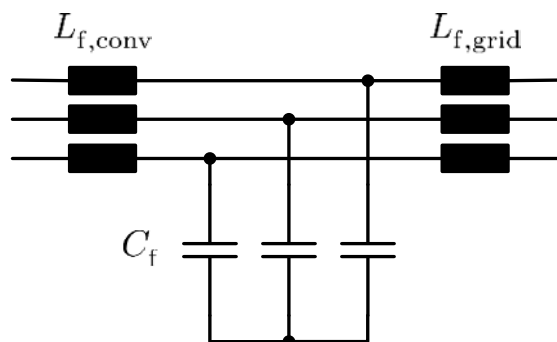


Figure 3-15: Sinusoidal filter.

The worst case spectrum of the voltage, which is used for the filter design, is given in Figure 3-16.

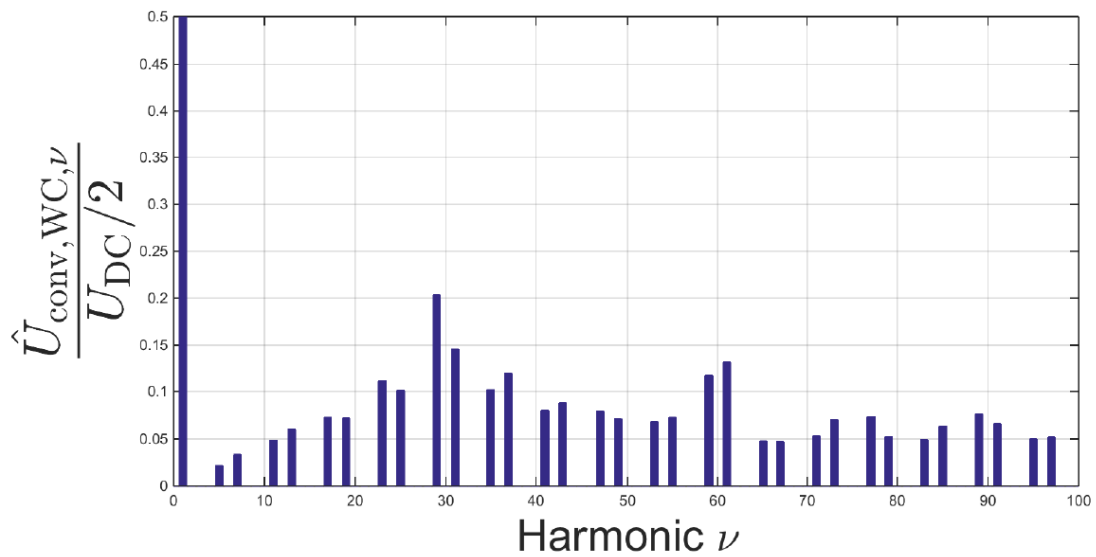


Figure 3-16: Worst case spectrum for filter design.

Due to the different number of parallel connected NPC VSI the harmonic current restrictions of each of the converters is different for the 10 MW PDD generator and the 20 MW PDD generator. As a result, the grid side filters of the converters must be different for the two cases, even with identical voltage rating, current rating, and carrier frequency. The assumptions that are made for calculating the current harmonic restrictions and the filter parameters are given in Table 3-2.

Table 3-2
Assumed grid parameters for filter design.

$U_{n,ll,rms}$	S_k	k_{XR}	$f_{carrier}$	$u_{k,transformer}$
2.9 kV	100 MVA	2	750 Hz	6 %

Figure 3-17 shows the output current spectrum for one of the three parallel converters for the 10 MW PDD generator including the current harmonic restrictions. The filter parameters for achieving this spectrum are listed in Table 3-3.

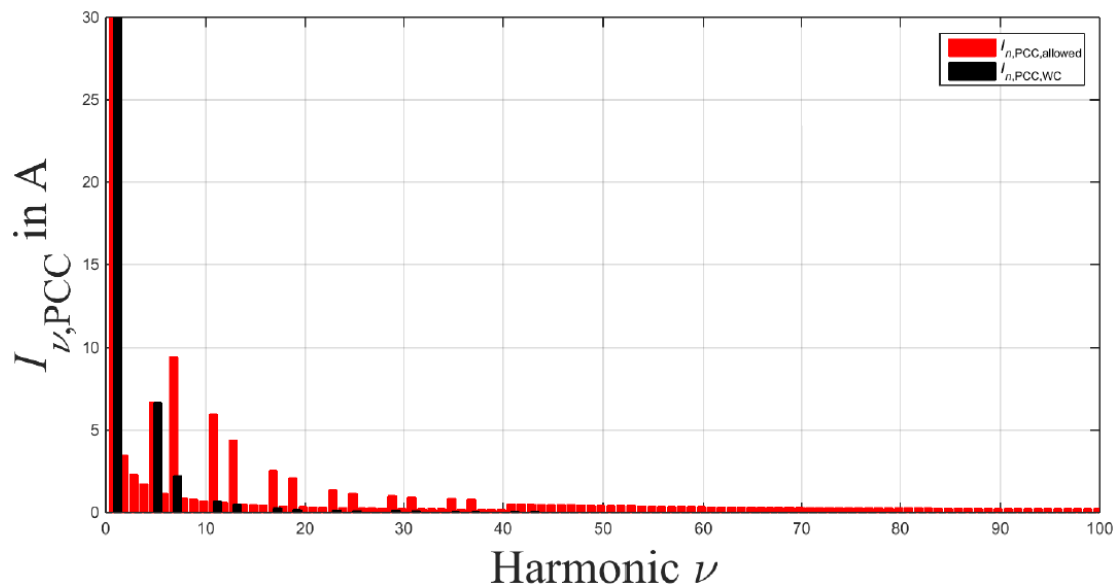


Figure 3-17: Output current spectrum for one 3-level NPC converter for the 10 MW PDD generator.

Table 3-3
Filter parameter for 10 MW PDD generator.

$L_{f,conv}$	C_f	$L_{f,grid}$
3.01 mH	475 μ F	2.07 mH

The output spectrum for one of the six parallel converters for the 20 MW PDD generator including the current harmonic restrictions is presented Figure 3-18. Table 3-4 shows the calculated filter parameters for this spectrum.

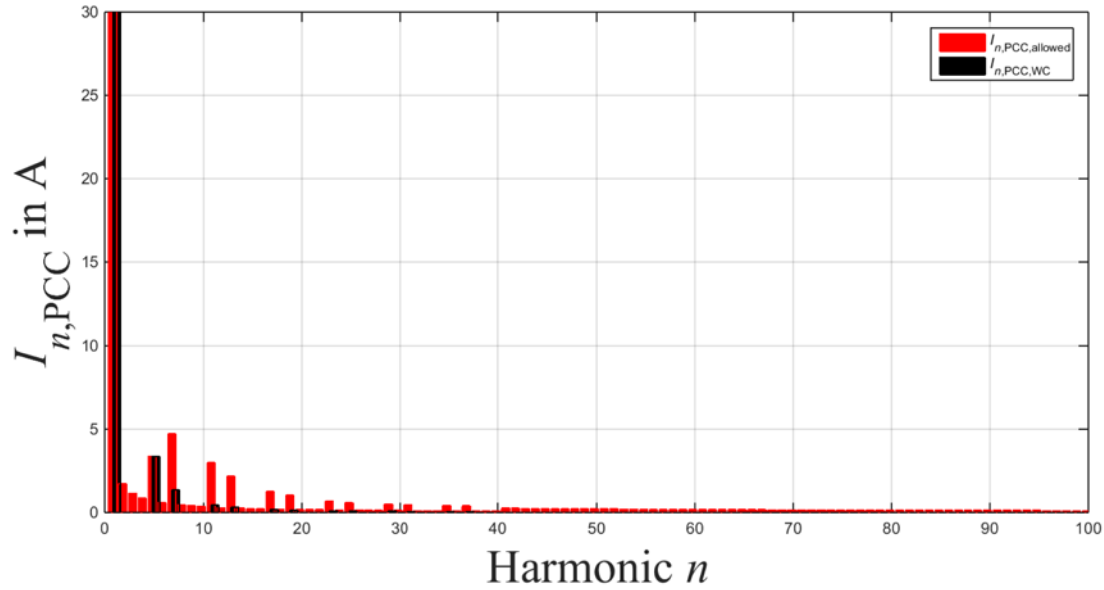


Figure 3-18: Output current spectrum for one 3-level NPC converter for the 20 MW PDD generator.

Table 3-4
Filter parameter for 20 MW PDD generator.

$L_{f,conv}$	C_f	$L_{f,grid}$
3.44 mH	555 μ F	2.39 mH

For the filter capacitors, the device MKP1847630354Y5 (350 V AC, 30 μ F, [3-10]) is used and connected in parallel and series to achieve the necessary capacitance analogue to the DC link capacitor. The resulting number devices for the 10 MW PDD filter capacitors is

$$n_{\text{devices}} = 3 \cdot n_{\text{series}} \cdot n_{\text{parallel}} = 1710 \quad (3-10)$$

and

$$n_{\text{devices}} = 3 \cdot n_{\text{series}} \cdot n_{\text{parallel}} = 1998 \quad (3-11)$$

for the 20 MW PDD filter capacitors. No devices are available from the shelf for the filter inductors. That is why no device and device number is given here for the inductor cost estimation in Section 3.5. Instead of estimating the cost based on specific devices, it is estimated based on the copper and iron volume.

Additional potential for optimization is given by using extended or different filter concepts, e.g. additional absorption filters. Due to the depth of this field, only the basic sinusoidal filter is considered in this report.

3.3.4 Generator Side Inductor

The PDD generator has no special restrictions for the harmonics of the generator currents (in contrast to the SCG in Chapter 2). Accordingly, no generator side filter is used. Nevertheless, before connecting the parallel generator side NPC VSIs, an inductor is used for each converter phase for suppressing any circulating currents between the parallel converters.

The inductance is calculated for a maximum circulating current ripple of 10 % of the maximum generator current and with the voltage mesh presented in Figure 3-19.

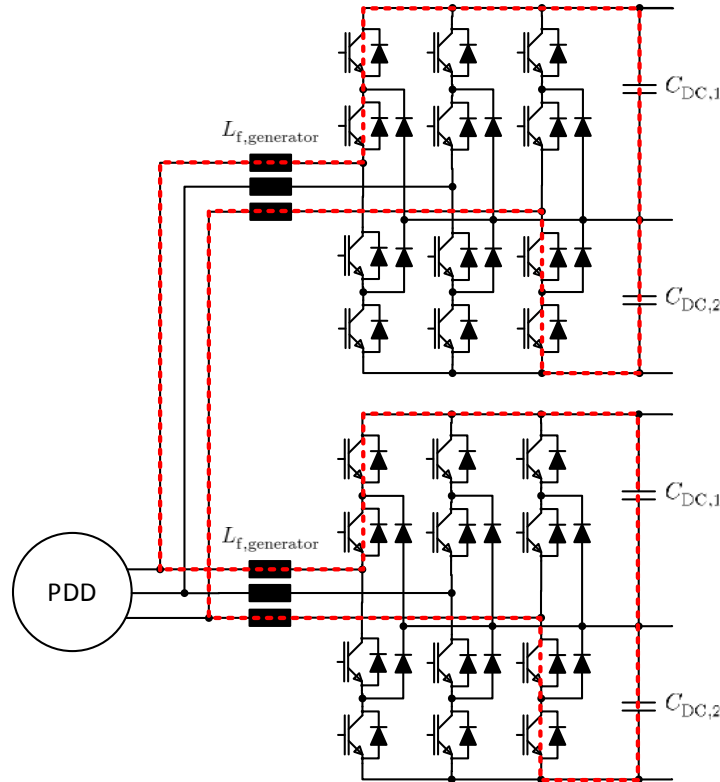


Figure 3-19: Voltage mesh for generator side inductor design.

The DC link voltages of the two shown NPC converters is assumed as $V_{DC,NPC1} = 1.05 \cdot V_{DC}$ and $V_{DC,NPC2} = 0.95 \cdot V_{DC}$. If both converters should have the same output voltage and the converter with the lower DC link voltage is in the same switching state the whole switching period, the other converter is in the investigated switching state only for $\Delta T = \frac{V_{DC,NPC2}}{V_{DC,NPC1}} \cdot T_{carrier}$. As a result, the generator side inductors are determined with

$$L_{f,generator} = \frac{1}{4} \cdot \frac{\Delta T \cdot (V_{DC,NPC1} + V_{DC,NPC2})}{\Delta i} \approx 1.95 \text{ mH}. \quad (3-12)$$

Analogue to filter inductor on the grid-side, no device is available of the shelf for these inductors.

3.4 Efficiency

The efficiencies of the converters are obtained via simulation. For the calculation of the efficiency the switching losses of the semiconductors, the conducting losses of the semiconductors, the

resistive losses of the filters are considered. Analogue to the thermal calculations in Section 3.3.2, baseplates of all devices are assumed to be constant at 90 °C.

For the 10 MW PDD converter efficiency, the applied rotational speed and power for different wind speeds is shown in Figure 3-20. These curves are approximated from characteristics given in report D1.21. For the 20 MW PDD, Figure 3-20 is scaled to a maximum power of 20 MW and a maximum rotational speed of 6.82 rpm. The resulting efficiency curves are given in Figure 3-21 and Figure 3-22. The efficiency at nominal operation of the 10 MW PDD converter is 98.0 % and the efficiency of the 20 MW PDD converter is 97.9 %.

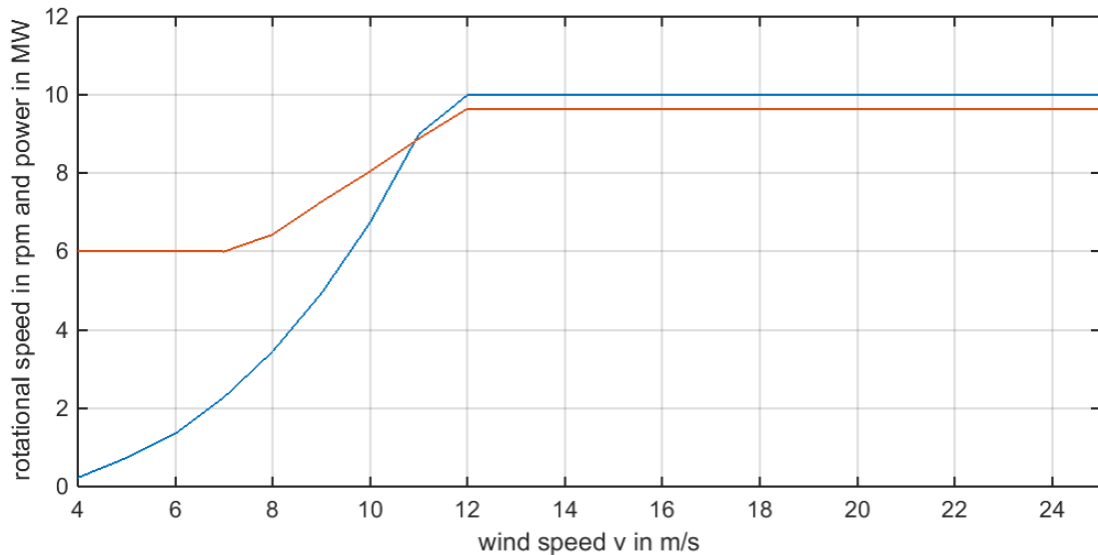


Figure 3-20: 10 MW Rotor operating conditions for CoE calculations.

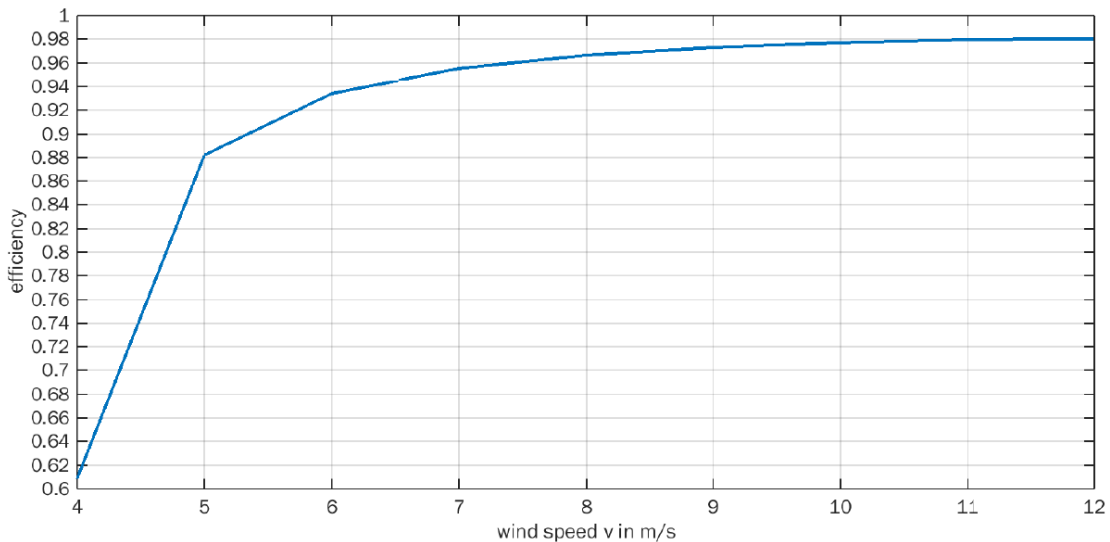


Figure 3-21: Converter efficiency for the 10 MW PDD generator.

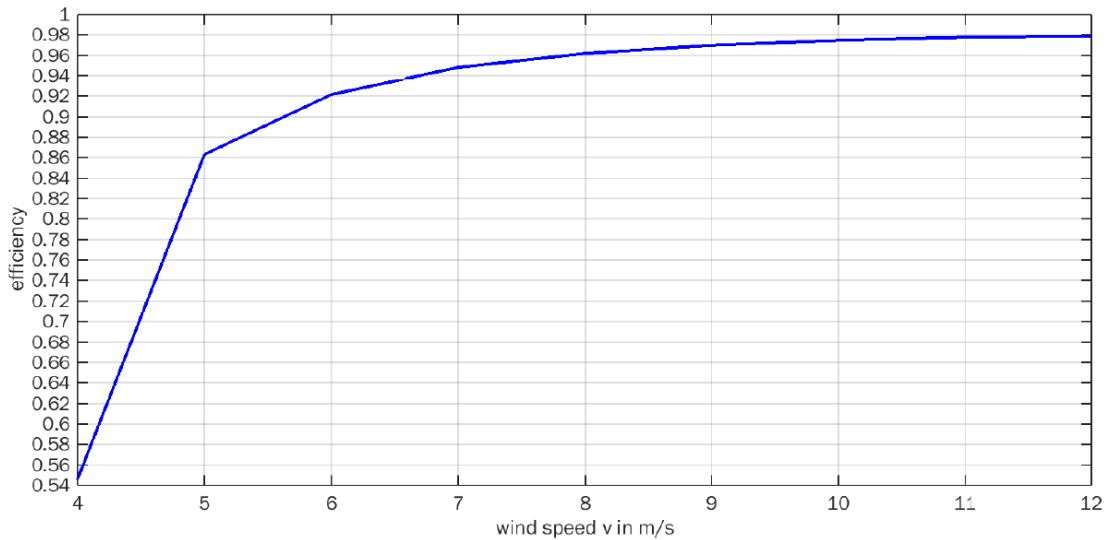


Figure 3-22: Converter efficiency for the 20 MW PDD generator.

3.5 Costs and CoE due to PE

The cost estimation in this report is done based on the cost estimation in report D3.31. One difference is that the estimation at hand uses actual semiconductor devices and their ratings/price instead of a price over rated current characteristic.

For the total cost six different factors are considered:

- Semiconductors
- DC link capacitors
- Grid side filters
- Generator side inductor
- Cooling
- Mechanical construction

The semiconductor costs are simply calculated from the number of IGBTs and clamping diodes with their corresponding prices. Enquired quotations from distributors provide the prices listed in Table 3-5.

Table 3-5
Semiconductor prices from distributors

	Price per single IGBT module (5SNA1200G450300)	Price per half bridge diode module (RM800DG-90F)
Quantity: 1	1964.00 €	881.30 €
Quantity: 50	1174.00 €	810.80 €

To get a more realistic cost estimation, prices for a quantity of 50 devices are used.

Regarding the DC link capacitors and the filter capacitors, Table 3-6 lists prices available from online distributors. Prices for a quantity of 48 and 500 are used.

Table 3-6
Capacitor prices from online distributors

	Price DCP6K07119EP00KS0F link)	per (DC	Price per MKP1847630354Y5 (Filter)
Quantity: 1	150.40 €		22,35 €
Quantity: 50	125.18 €		-
Quantity: 500	-		15.29 €

Similar to D3.32, the filter inductor prices are not obtained from a distributor, the prices are estimated based on copper and iron volume. The cost of material is calculated from these volumes (assumed prices: copper 9.0 €/kg, iron 1.5 €/kg) and then multiplied by the factor 3 to represent manufacturing costs and profit margins of the manufacturer.

The cost of the cooling system is estimated from the maximum losses and a cost per loss factor of 0.8 €/W from report D3.32

Because the mechanical cost and cost for other components is difficult to calculated without designing the real converter, these costs are estimated with 40 % of the components (semiconductors, inductors, capacitors) cost of the converter.

In conclusion, the resulting costs of the different parts and the estimated total costs are given in Table 3-7.

Table 3-7
Converter cost splitted in categories and total converter cost

	10 MW PDD converter	20 MW PDD converter
Number of IGBT modules (single switch)	72	144
IGBT modules (single switch) cost	85 k€	169 k€
Number of Diode modules (half bridge)	18	36
Diode modules (half bridge) cost	15 k€	29 k€
Total semiconductor cost	100 k€	198 k€
DC link capacitor	66 k€	132 k€
Filter capacitor	78 k€	183 k€
Converter side filter inductor	110 k€	242 k€
Grid side filter inductor	83 k€	184 k€
Generator side inductor	62 k€	123 k€
Total passive component cost	399 k€	864 k€
Cooling system cost	160 k€	336 k€
Mechanical construction cost	200 k€	425 k€
Total cost	859 k€	1823 k€

For representing the cost of energy (CoE) caused by the converter, an IEC wind distribution based on a wind turbine class 1A from [3-11] is used, Figure 3-23. Combined with the efficiency characteristic in Figure 3-21 and Figure 3-22, the power for different wind speeds in Figure 3-20, and a postulated lifetime of 25 years, the resulting CoE caused by the converter (without maintenance) for the 10 MW PDD generator and the 20 MW PDD generator are presented in Table 3-8.

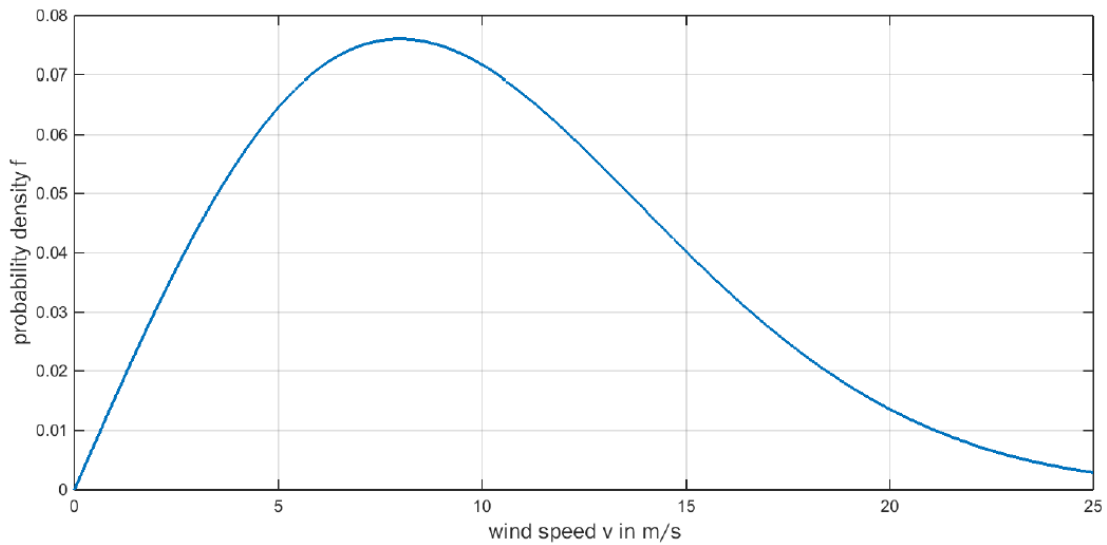


Figure 3-23: IEC Rayleigh wind distribution based on wind turbine class 1A.

Table 3-8

Cost of energy caused by the converter without maintenance and annual energy only considering converter efficiency

	10 MW PDD converter	20 MW PDD converter
Cost of energy caused by the converter without maintenance	0.731 €/MWh	0.777 €/MWh

3.6 Size and Weight

As already explained in report D3.32, an accurate estimation of the converter size and mass is not possible without exactly planning the converter realization with all necessary components (especially the mechanical realization). That is why the converter size and mass is estimated based on existing converters on the market. In case of medium voltage NPC inverters with roughly the same power rating, there are several converters available on the market. An existing converter which has a very similar rating is the Siemens SINAMICS SM150 with HV-IGBT air cooling [3-12]. It is rated for 3.3 kV output voltage and a power of 3.4-4.6 MVA which fits the requirements of the investigated converters quite good. The size and weight of the SINAMICS SM150 (including back to back NPC converter and cooling) is given in Table 3-9.

Table 3-9

SINAMICS SM150 (with HV-IGBT air colling) size and weight

Width	Height	Depth	Weight
3020 mm	2570 mm	1275 mm	2850 kg

Based on the SINAMICS SM150 data and the number of parallel converters, the size and weight for the 10 MW PDD converter and 20 MW PDD converter are calculated and presented in Table 3-10.

Table 3-10

Estimated converter size and weight

	Volume	Weight
10 MW PDD converters	29.69 m ³	8550 kg
20 MW PDD converters	59.37 m ³	17100 kg

3.7 Control

The control of the converter can be divided into different parts. One controller (per segment) is used on the generator side. On the grid side, each of the parallel 3-level NPC converters is controlled separately.

The grid side controller structure is presented in Figure 3-24. On the left side, the DC link voltage controller is shown. The set point value and the actual value of the total DC link voltage are used to calculate the error of the stored energy in the DC link capacitors. Then, this energy is controlled by a PI controller. Based on the output of this controller, a feed forward term for the power, the set point reactive power, and the d-component of the generator voltage the set point values for the dq-components of the positive sequence currents are determined. The currents are controlled via positive and negative sequence controllers. The positive sequence controller is shown in Figure 3-26 and the negative sequence controller is built up analogously.

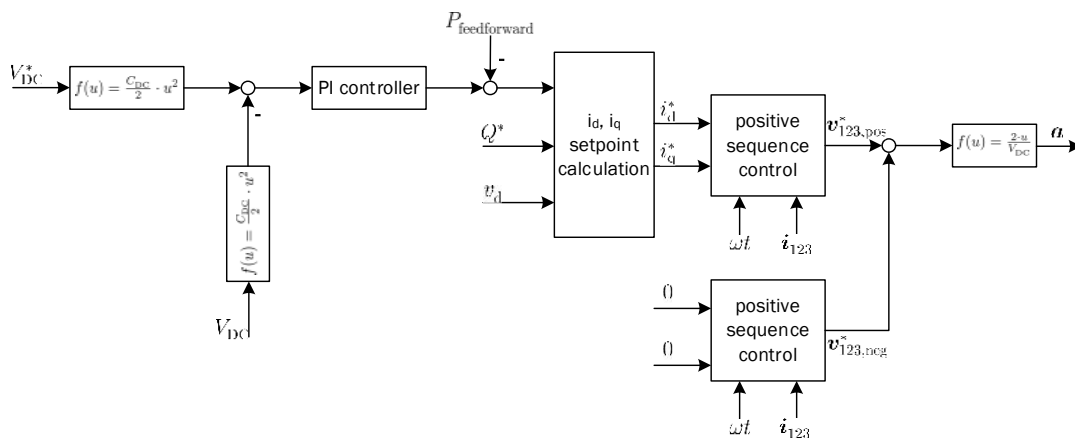


Figure 3-24: Grid side controller including DC link voltage control and grid current control.

Figure 3-25 displays the generator side control structure. The speed is controlled with a PI controller. The set point value for the speed must be calculated based on the operating point of the wind turbine. Because the simulations in this report all only address operation in one operating point, this part of the control structure is not included. Besides, the output of the speed controller is used as the set point value for the q-component of the generator current control (build up based on Figure 3-26).

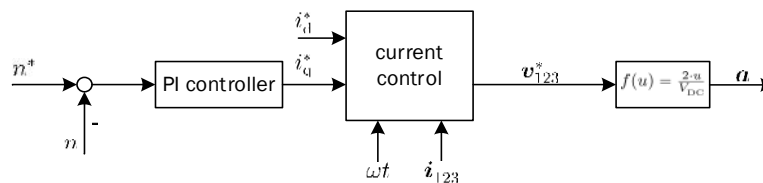


Figure 3-25: Generator side controller including speed control and generator current control.

All used dq-component current controllers are built up identical or analogue to Figure 3-26. The currents are controlled via PI controllers and voltage feedforward terms are implemented. Besides, cross coupling between d- and q-component is compensated.

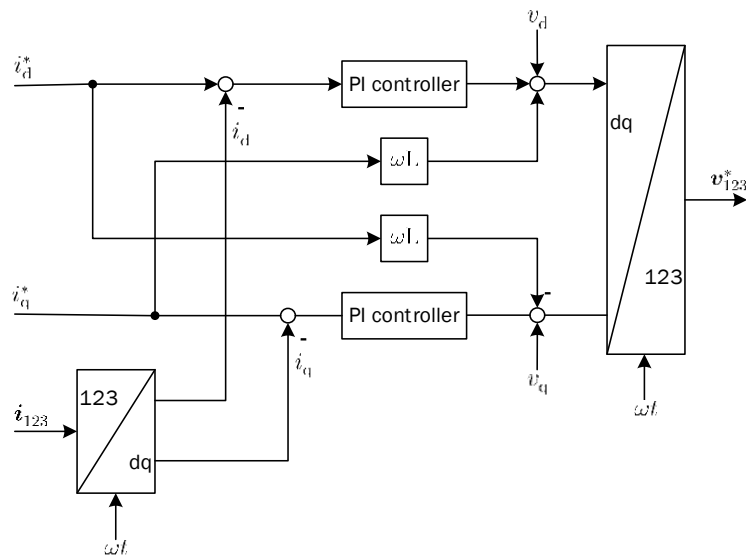


Figure 3-26: dq-component current controller.

For the ideal simulations in this report, no neutral point balancing of the DC link and no control of possible circulating currents between the converters is necessary. For realizing the converter, these aspects have to be addressed as well. Additionally, grid requirements like fault ride through behaviour must be fulfilled. This can be addressed analogously to Section 2.6.2 or several publications investigating fault ride through for the NPC converter, e.g. [3-13].

3.8 Simulation

A simulation with Matlab/Simulink and the PLECS Blockset toolbox is used to test the converter design. The IGBTs and diodes in the model behave like ideal switches regarding their electrical characteristics. The control concept is implemented as a digital controller. The PDD generator is modeled via a permanent magnet synchronous machine with parameters fitted to the known 10 MW and 20 MW PDD parameters. For the 10 MW PDD converter, all three parallel connected three-level NPC converters are simulated. To reduce the computation effort and because the two segments of the 20 MW PDD can be investigated separately, only one of the segments is simulated.

Figure 3-27 shows the machine currents at operation with nominal power for the 10 MW PDD. The machine side currents of the first of three parallel NPC converters are presented in Figure 3-28. For the sake of simplicity only the machine side currents of one of the NPC converters are shown. The currents of the other two converters behave analogously. Figure 3-29 and Figure 3-30 display the grid current and the grid side currents of the first of three parallel NPC converters. The THD of the grid current is lower than 2%.

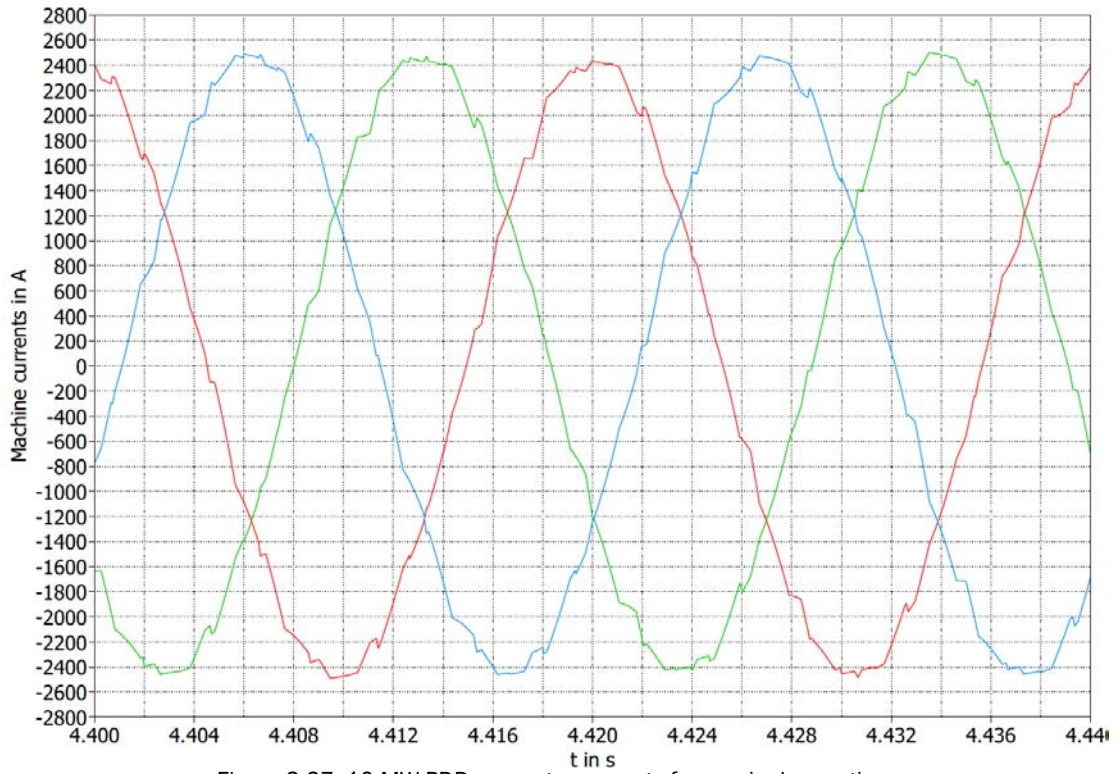


Figure 3-27: 10 MW PDD generator currents for nominal operation.

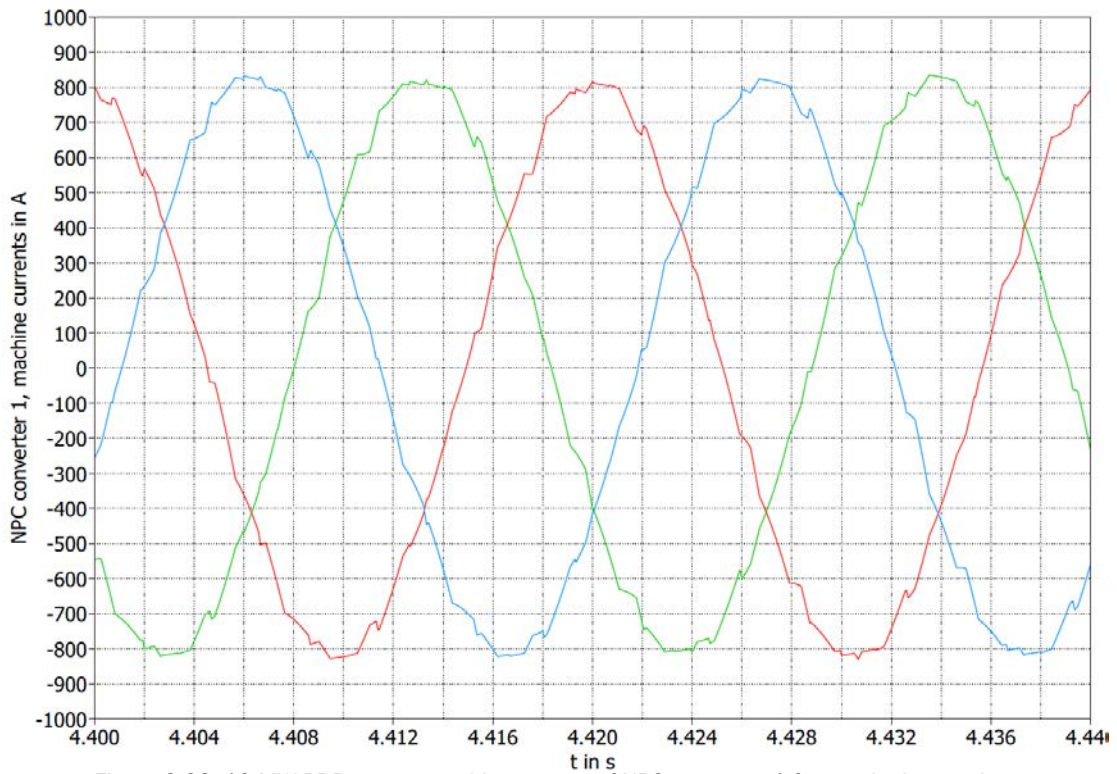


Figure 3-28: 10 MW PDD generator side currents of NPC converter 1 for nominal operation.

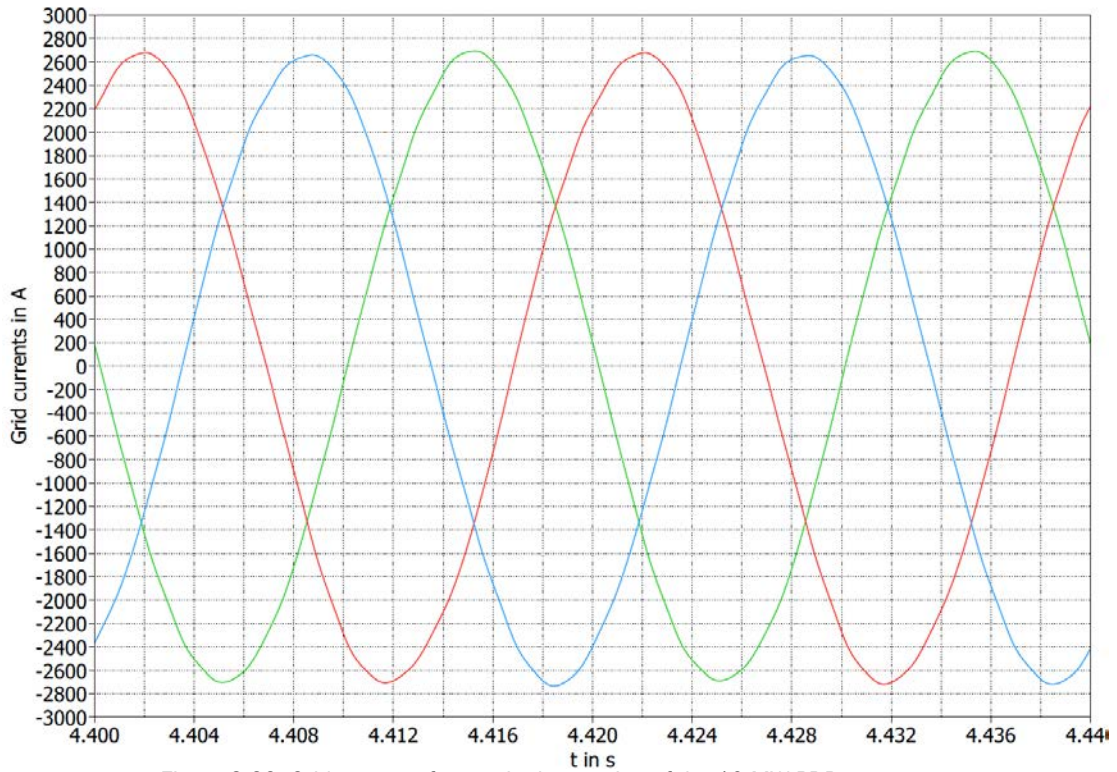


Figure 3-29: Grid currents for nominal operation of the 10 MW PDD generator.

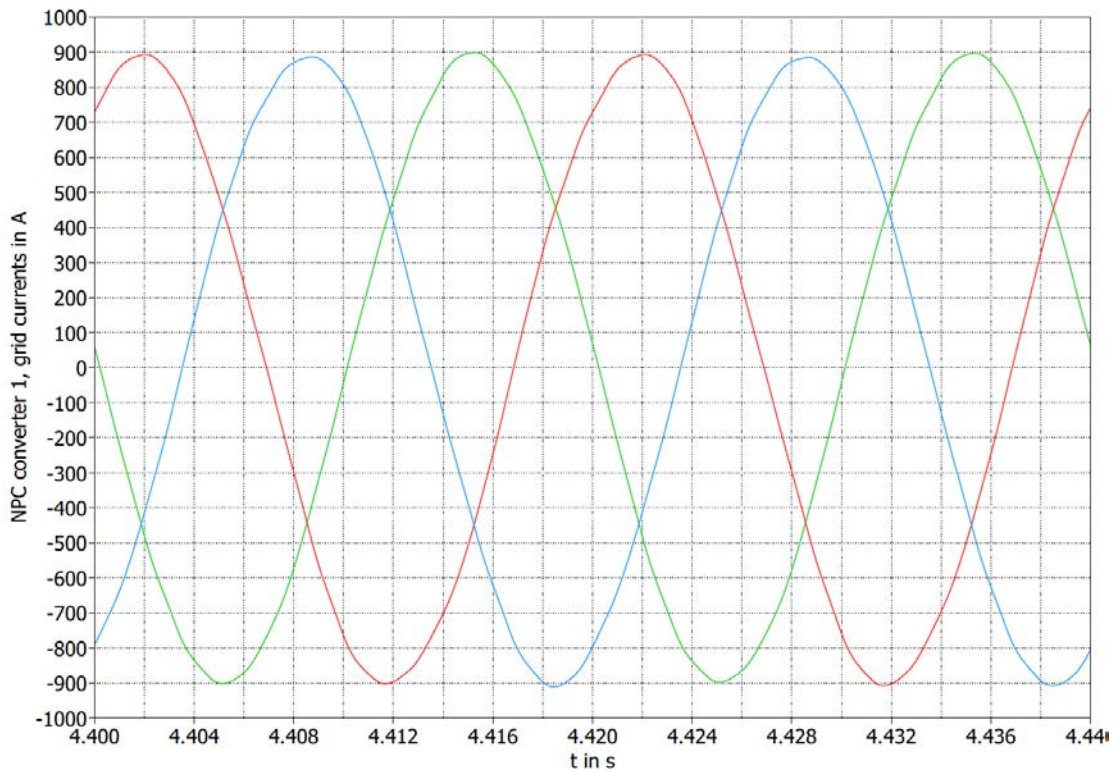


Figure 3-30: Grid side currents (after filter) of NPC converter 1 for nominal operation of the 10 MW PDD generator.

The results for one segment of the 20 MW PDD generator look similar, because of the high similarity of the two converter designs. Only the electrical frequency of the generator at the nominal operating point is different.

Figure 3-31 shows the PDD generator currents and Figure 3-32 the machine side currents of the first of three NPC converters. The grid currents and the grid side currents of NPC converter 1 are displayed in Figure 3-33 and Figure 3-34. Again, the THD of the grid current is lower than 2%.

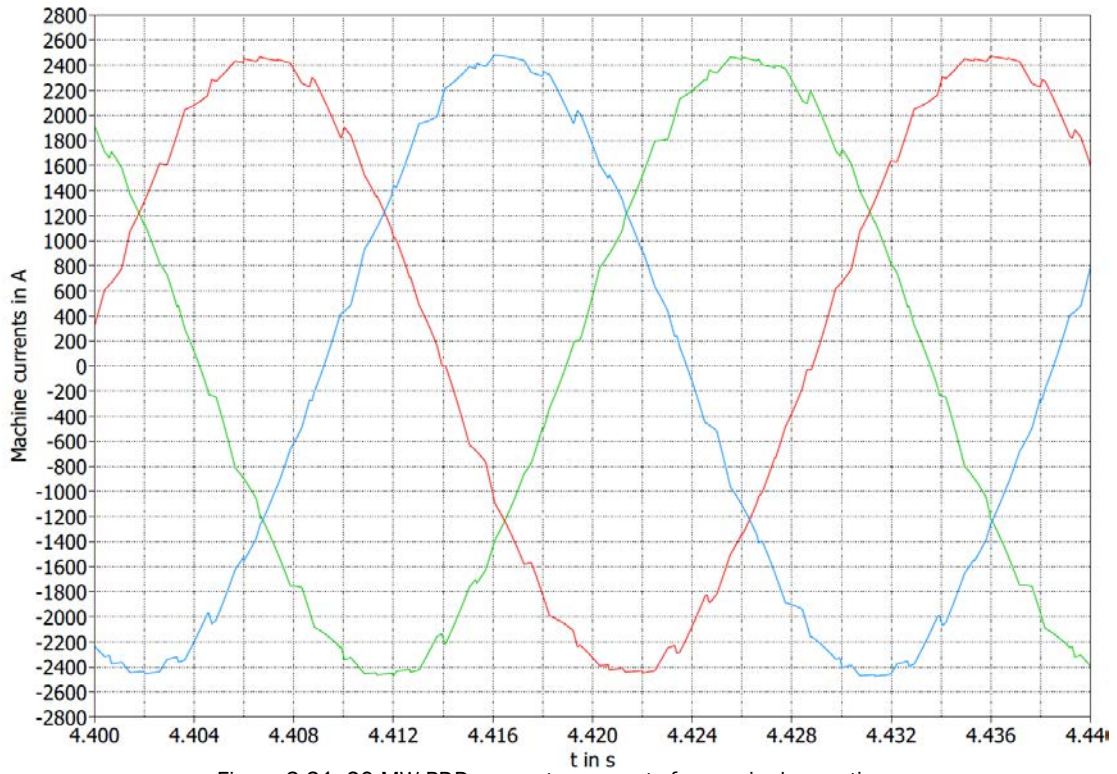


Figure 3-31: 20 MW PDD generator currents for nominal operation.

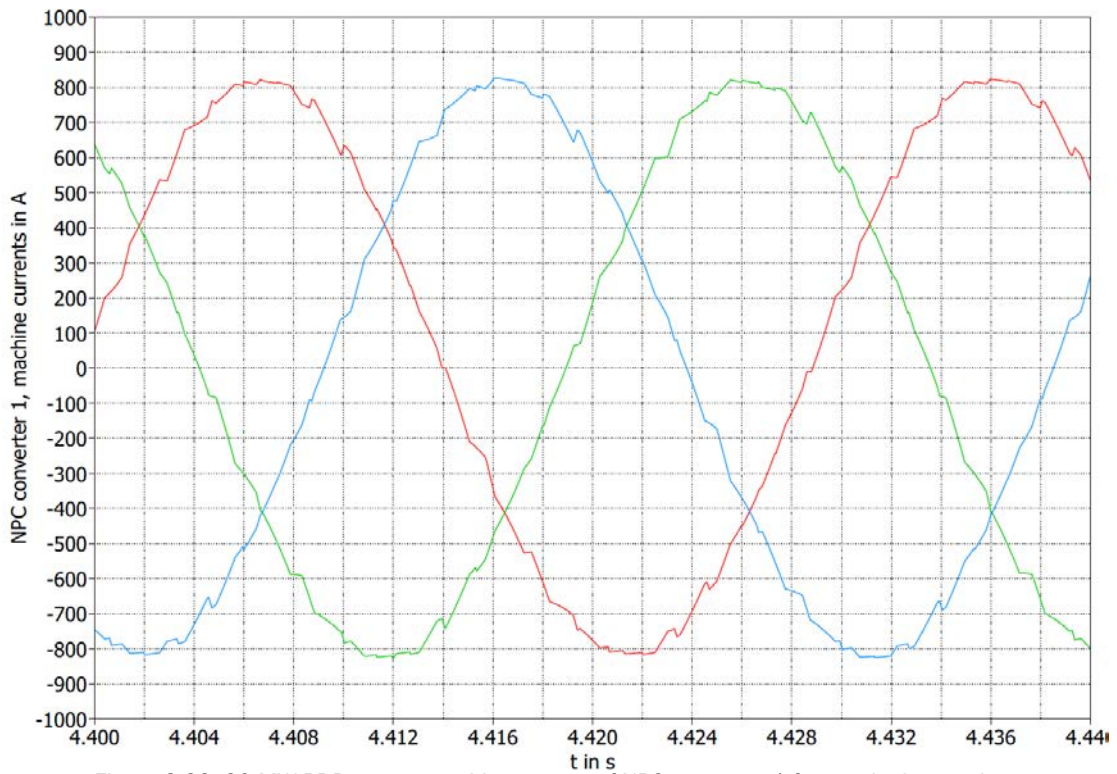


Figure 3-32: 20 MW PDD generator side currents of NPC converter 1 for nominal operation.

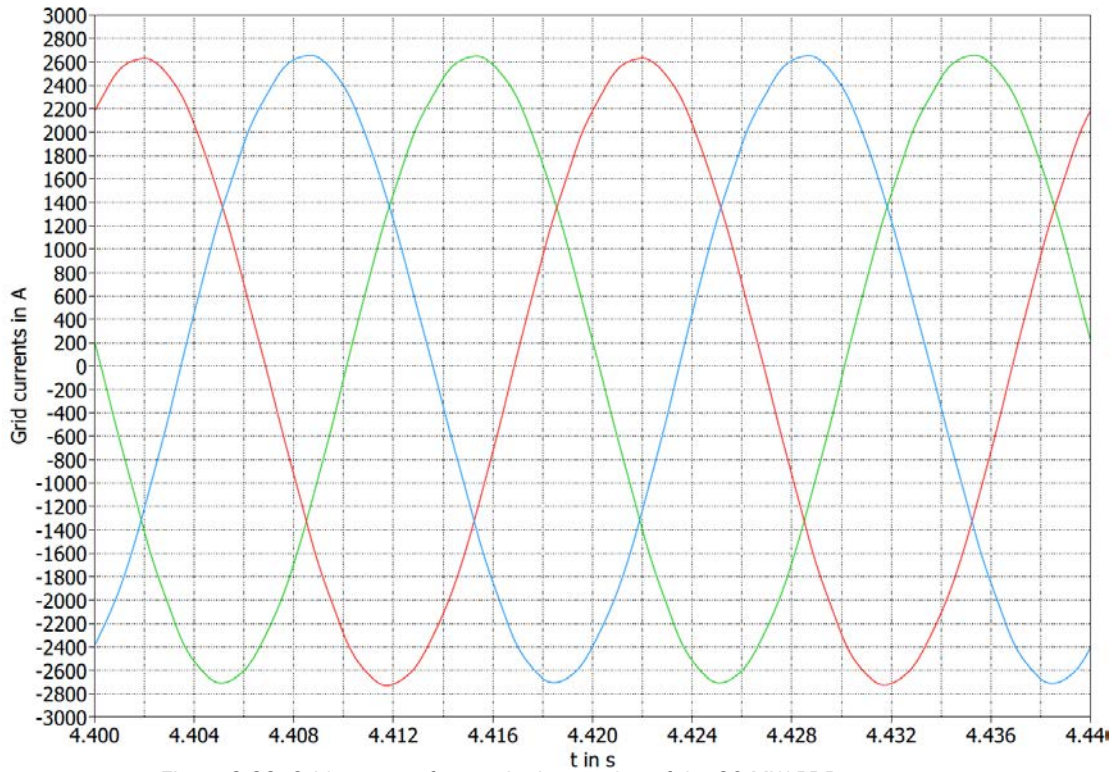


Figure 3-33: Grid currents for nominal operation of the 20 MW PDD generator.

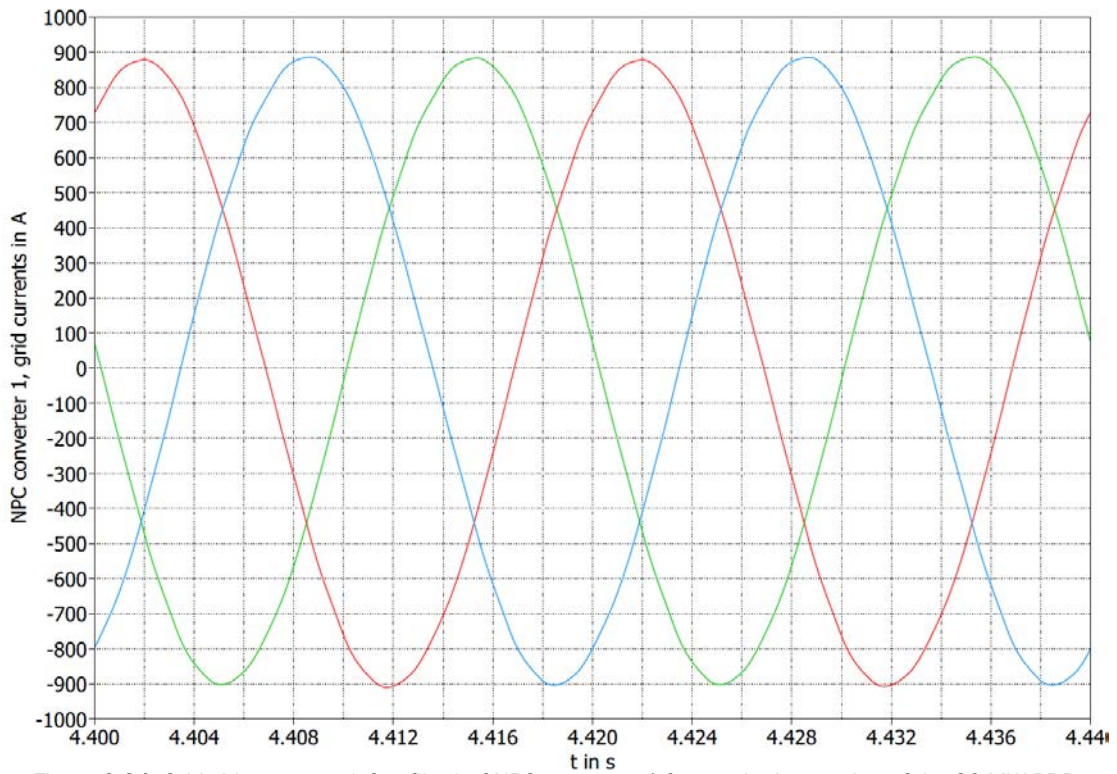


Figure 3-34: Grid side currents (after filter) of NPC converter 1 for nominal operation of the 20 MW PDD generator.

3.9 Conclusions

This chapter presented the converter design tailored to the 10 MW PDD generator and the 20 MW PDD generator. Due to the possibility of generator segmentation, new (compared to report D3.32) converter concepts were possible. A brief investigation indicated no significant advantages by these topologies. That is why a parallel NPC converter based concept was chosen. The 20 MW PDD generator was divided into two segments to reduce the maximum blocking voltage of the switching devices, simplifying the design.

Resulting from the semiconductor, DC link capacitor, and filter design the cost of the two converters had been calculated. These costs showed no unexpected high discrepancy to the costs estimated in report D3.31. Based on the efficiency obtained with a simulation model, the cost of energy due to the converter was calculated. This can be used to estimate the total cost of energy for the wind turbines.

The control concept of the NPC converters was presented, which is based on standard control approaches. The proper function of the converters with this control concept and the component design was shown by a detailed simulation model.

3.10 References

- [3-1] WIMA, „WIMA DC-LINK MKP 6,“ datasheet, 2014.
- [3-2] N. Kaminski and A. Kopta, “Failure Rates of HiPak Modules Due to Cosmic Rays,” ABB Switzerland Ltd, Semiconductors, 2011.
- [3-3] ABB Switzerland Ltd, Semiconductors, „ABB HiPak IGBT Module 5SNA 0800J450300,“ datasheet, 2012.
- [3-4] ABB Switzerland Ltd, Semiconductors, „ABB HiPak IGBT Module 5SNA 1200G450300,“ datasheet, 2014.
- [3-5] Mitsubishi Electric Corporation, „<High Voltage Diode Modules> RM800DG-90F,“ datasheet, 2012.
- [3-6] Mitsubishi Electric Corporation, „<High Voltage Diode Modules> RM1200DG-90F,“ datasheet, 2012.
- [3-7] R. Meyer und A. Mertens, „Design and Optimization of LCL Filters for Grid-Connected Converters,“ in *15th International Power Electronics and Motion Control Conference (EPE-PEMC ECCE Europe)*, Novi Sad, Serbia, 2012.
- [3-8] R. Meyer und A. Mertens, „Design of LCL Filters in Consideration of Parameter Variations for Grid-Connected Converters,“ in *IEEE Energy Conversion Congress & Exposition (ECCE)*, Raleigh, NC, USA, 2012.
- [3-9] BDEW, „Generating Plants Connected to the Medium-Voltage Network – Guideline for generating plants’ connection to and parallel operation with the medium voltage network,“ Technical Guideline, Berlin, Germany, 2008.
- [3-10] Vishay Roederstein, „MKP1847 AC Filtering - Metallized Polypropylene Film Capacitor AC Filtering Radial Type,“ datasheet, 2014.
- [3-11] IEC, „IEC 61400-1 - Wind turbines - Part 1: Design requirements,“ International Standard, 2005.

[3-12] Siemens AG, „SINAMICS drives - SINAMICS GM150 and SINAMICS SM150 Medium-Voltage Drive Converters with HV-IGBT technology,“ product brochure, 2009.

4 CURRENT SOURCE CONVERTER DESIGN TAILORED TO SCG AND PDDG

4.1 Introduction

Current-source converters have been proposed for use in wind energy applications [4-1], and one study has shown that costs could be considerably lower than equivalent voltage-source converters [4-2]. Unfortunately the load-commutated converters under consideration have difficulty complying with grid codes in terms of harmonics and grid fault ride-through, and can require generators modified for lower synchronous reactance.

These issues could be solved by the addition of voltage-source active filters, making a tandem converter [4-3]. The current-source converter handles the main power flow, with low cost and losses, while the active filter ensures a smooth current waveform. The rating for the active filter is about a quarter that of the current-source converter, so the overall converter cost compares favourably with more conventional NPC converters.

4.2 Current Source Converters Topologies

Topologies for the non-segmented generators are shown in Fig.4.1. For each picture the current source converter is at the top, with the active filters underneath. The active filters are cascaded H-bridge converters, and are connected using a small coupling inductance L_f , which limits the di/dt rate during thyristor commutation. The multilevel active filter means that the generator and transformer inductances are sufficient to provide low current harmonics. The coupling inductances in combination with R-C snubbers on the thyristors control the dv/dt experienced by the generator and transformer. As can be seen, the difference between the topologies for the superconducting and pseudo-direct drive generators is that the latter does not use an active filter on the generator side, as the generator is able to tolerate the non-sinusoidal current from the converter.

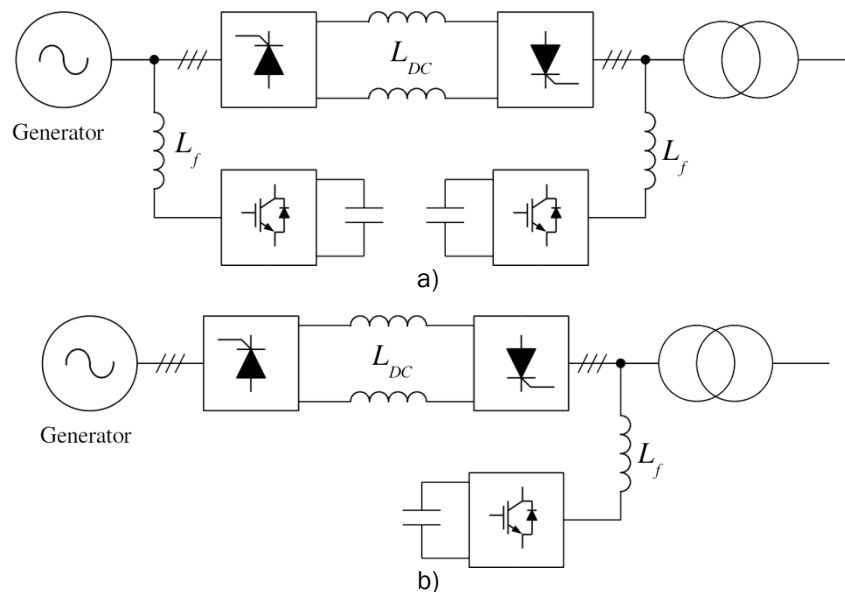


Fig.4.1 Current-source topologies for non-segmented generators: a) Superconducting generator, b) Pseudo-Direct Drive generator.

For the 20MW generator the number of series thyristors is increased, to allow for the 6.6kV output voltage, and the number of series modules in the active filter is also increased.

Topologies for the segmented generators are shown in Fig.4.2. Unlike a voltage-source converter, in which the rectifiers are connected in parallel to a common DC link, the rectifiers here are connected in series, using a lower voltage. This means that each segment of the

superconducting generator requires its own active filter. The inverter side of the converters is identical to that used for the non-segmented generators. The 20MW generator doubles the voltage, using a different active filter topology and higher thyristor voltage ratings. On the grid side, the 20MW system increases the number of series thyristors and series active filter modules.

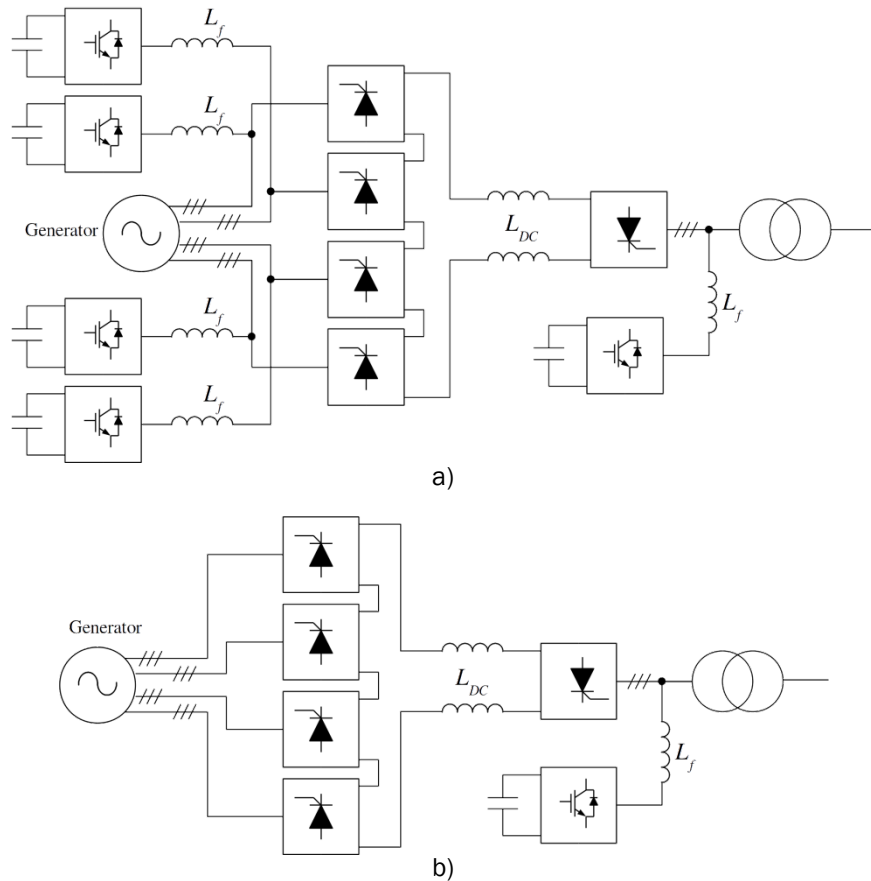


Fig.4.2 Current-source topologies for segmented generators: a) Superconducting generator, b) Pseudo-Direct Drive generator.

Active filter topologies are shown in Fig.4.3. The converters for non-segmented generators and the grid side of the segmented generator converters use a cascaded H-bridge converter shown in Fig.4.3a, where the voltage rating can be increased by increasing the number of series modules. The converters for the segmented superconducting generator are shown in Fig.4.3b and c, where a 2-level converter is used for 10MW and a 3-level NPC converter for 20MW to double the voltage rating.

Fault-tolerance or redundancy is a feature of all the converters. For the main current-source converter, an extra redundant thyristor is added in each stack, except for the rectifiers of the segmented generator converters, where the segmentation allows fault-tolerance. The press-pack thyristors are designed to fail in a short circuit, continuing to conduct. For the segmented SCGs, the multiple independent generator-side active filters allow fault-tolerance, with a fault reducing the DC voltage, requiring a slightly higher inverter firing angle. For the non-segmented SCGs, the failure of a filter module will reduce the overall voltage capability of the filter, although the angle between the phases can be adjusted to maximise the voltage [4-4]. The result of this is that a module fault will require the turbine speed to be reduced, to keep the voltage within limits, although alternatively the current could be reduced to limit the DC voltage ripple in the filter, which will have a similar effect. For the grid-side active filters, DC voltage ripple is considerably lower, and the grid voltage is fixed, so an additional redundant module is added to each phase string.

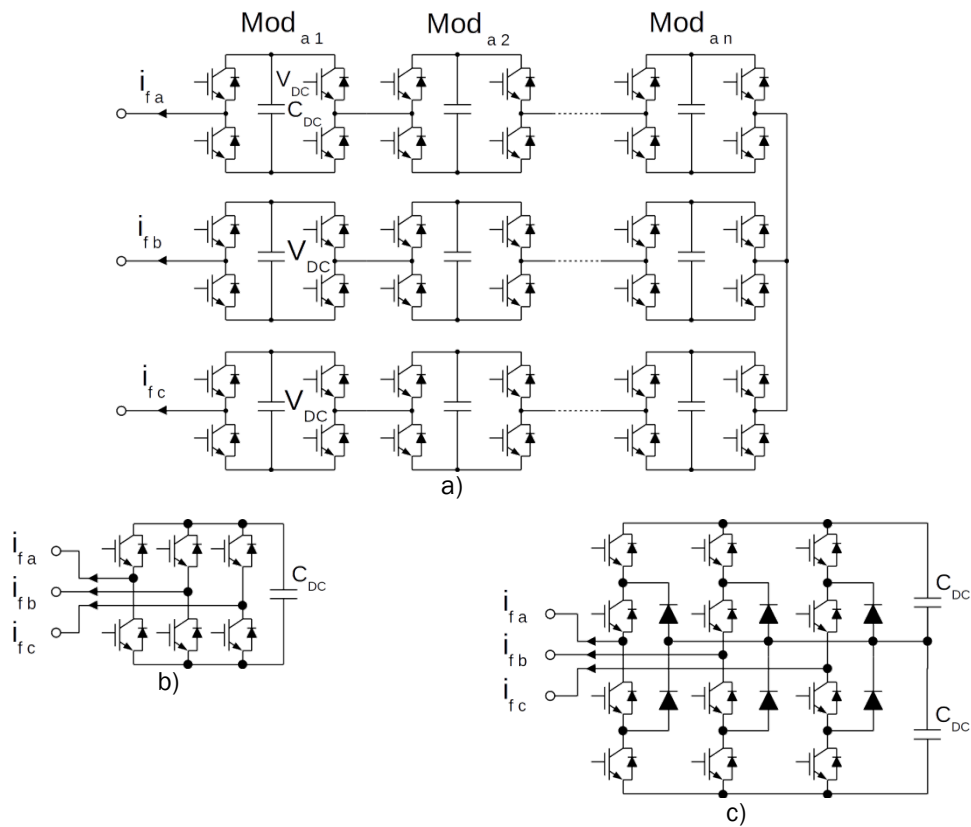


Fig.4.3 Active filter topologies: a) Cascaded H-bridge for non-segmented generators and AC side for segmented generators, b) 2-Level for 10MW superconducting generator, c) 3-Level NPC for 20MW superconducting generator.

Generator and converter parameters for superconducting the generators are given in Table 4.1, and the PDD generators in Table 4.2. The voltage of the segments for the 10MW segmented superconducting generators are set to 690V, to allow the use of conventional 690V converters using 1700V IGBTs for the active filters. For the 20MW segmented generators the generator voltage is doubled, and the same 1700V IGBTs are used in 3-level NPC active filters. For the PDD generator, where no active filter is used, the non-segmented generator voltage is simply divided by the number of segments to obtain the segmented generator voltage.

Generator voltages were based on parameters provided by the generator designers. In the case of the SCG, parameters were given for a 3,300V 10MW generator and a 6,600V 20MW generator, and it was assumed that the required voltages for the segmented generators could be achieved. For the PDD, parameters are given per coil of the generator, and are thus limited by the need for an integer number of coils per stator slot, which is the reason for the 7,046V for the 20MW PDD.

The grid voltage is set so that the inverter is operating with a firing angle of around 20 degrees at rated power, which minimises the reactive power which must be supplied by the active filter while keeping the firing angle a reasonable distance from zero, where instability will occur.

Table 4.1
Superconducting generator and converter parameters

Generator	Rating	Frequency (Hz)	Segments	Generator Voltage (V)	Grid Voltage (V)	DC-Link Current (A)
T5,6	10MW	1.93	1	3,300	3,500	2,300
T8,9	10MW	3.22	1	3,300	3,500	2,300
T5,6	10MW	1.93	4	690	2,900	2,750
T8,9	10MW	3.22	4	690	2,900	2,750

T10	20MW	4.09	1	6,600	7,000	2,300
T11	20MW	2.73	1	6,600	7,000	2,300
T10	20MW	4.09	4	1,380	5,800	2,750
T11	20MW	2.73	4	1,380	5,800	2,750

Table 4.2
PDD generator and converter parameters

Rating (MW)	10	10	20	20
Segments	1	4	1	4
Frequency (Hz)	48.25	48.25	34.1	34.1
Generator Voltage (V)	3,300	825	7,046	1,762
Grid Voltage (V)	2,800	2,800	6,100	6,100
DC-Link Current (A)	2,850	2,850	2,630	2,630
Segment Resistance (mΩ)	3.94	0.984	8.86	2.21
Segment Inductance (mH)	1.21	0.302	3.59	0.896

It was found in simulation that for the PDD generators the relatively large reactance for a diode rectifier system (around 0.34 P.U.) led to a large commutation overlap, which significantly reduces the DC voltage and increases the DC current. Commutation overlap is not a problem for the SCGs, as the rectifier commutates through the active filter, with a relatively small coupling inductance.

The use of non-standard grid voltages means that non-standard grid-coupling transformers will be required, which could add to the overall cost. Standard transformer voltages could be used, but would require either the inverter or rectifier to be operated at a larger firing angle at rated wind speed, increasing the requirements for reactive power compensation from the active filters. This is undesirable, as it will increase losses and ratings for the filters. One study has found that non-standard transformer windings add around 6% to the transformer cost [4-2], although in this case the added cost was for zig-zag windings rather than non-standard voltages. Because of this, and the transformer cost not being included in this study, it was decided to use the non-standard grid voltages.

4.3 Costs

Costs are updated compared with those given in Deliverable 3.32 to reflect the addition of the segmented generators, the removal of the generator-side active filter for the PDD generator and the modified active filter DC-link capacitance requirements from the controller design.

4.3.1 Active Filter Costs

For the active filters, the DC-link energy ripples were re-calculated based on the revised generator frequencies, using the methodology described in Deliverable D3.32. The IGBTs and capacitors used in D3.32 were again used here, and are listed in Table 4.3, with capacitors connected in parallel to achieve the desired capacitance. The generator-side active filter parameters and cost are given in Table 4.4. Previously 4 and 7 series modules per phase were chosen for the 10 and 20MW generators, but this is increased to 5 and 8 series modules. This increases the level of tolerance to module faults – a module fault will reduce the capability for voltage ripple in the remaining modules, which will reduce the maximum power output of the turbine.

Table 4.3
Components for generator-side active filters for non-segmented generators

IGBT	FZ1600R17HP4	1600A RMS	1700V	€762.29
Capacitor	AVX FFL16U0537K	530μF	1100V	€92.6

Table 4.4
Generator-side active filter costs for non-segmented superconducting generators

Generator	Rating	Energy ripple (J)	Series modules/phase	Capacitors per module	Total cost
T5,6	10MW	80,900	5	62	€131,000
T8,9	10MW	48,500	5	38	€98,300
T10	20MW	76,300	8	42	€166,000
T11	20MW	114,000	8	63	€213,000

The energy ripples and capacitor requirements for the capacitors in the segmented generator filters were calculated in a similar manner, based on a 10% peak to peak voltage ripple. An average DC-link voltage of 1100V was used, for a modulation depth of 0.9, with 1400V capacitors. The components used are shown in Table 4.5, and two diodes are used in parallel in the NPC active filter to achieve the required current rating. Filter costs and parameters are shown in Table 4.6, where it should be noted that the energy ripple and capacitance requirement is for each DC-link. The NPC filters used with the 20MW generator has two DC-links, so the number of capacitors is doubled.

Table 4.5
Components used for generator-side active filters for segmented generators

IGBT	FZ1600R17HP4	1600A RMS	1700V	€762.29
Diode	DZ800S17K3	800A Avg	1700V	€133.83
Capacitor	AVX FFL16Q0507K	500µF	1400V	€121.18

Table 4.6
Generator-side active filter costs for segmented superconducting generators.

Generator	Rating	Capacitor energy ripple (J)	Capacitance (mF)	Capacitors per filter	IGBTs per filter	Diodes per filter	Total cost
T5,6	10MW	3,900	27.1	54	6	0	€44,500
T8,9	10MW	2,300	16.2	32	6	0	€33,800
T10	20MW	6,110	42.4	170	12	12	€125,000
T11	20MW	9,150	63.6	254	12	12	€166,000

Costs for these active filters are significantly lower than for the non-segmented generators, as the effects of the low AC frequency are reduced when the DC link is shared between three phases, although this is less significant with the NPC converters.

For the grid side filters the ripple energy was calculated as before. The additional ripple from the transferring of the rectifier ripple with the SCG converter to the grid side, ΔE , was calculated using (4.1). ω is the generator frequency, V_g is the generator rated line voltage and I_{DC} the rated DC-link current.

$$\Delta E = \sqrt{2}V_g I_{DC} \int_{-a/\omega}^{a/\omega} \sin \omega t - \frac{3}{\pi} dt, \quad (4-1)$$

$$a = \cos^{-1} \frac{3}{\pi}$$

$$\Delta E \approx \frac{0.02557 V_g I_{DC}}{\omega}$$

For the grid side, the minimum number of series modules to achieve the grid voltage rating was calculated, and the required number of capacitors for the ripple current calculated. For the grid filter there must always be sufficient modules to meet the grid voltage requirements, so an additional module was added to each string for redundancy. In addition, the grid side filter has a higher current due to compensating for the active power from the main converter operating at a firing angle larger than zero. To handle this, the FZ2400R17HP4 IGBT is used, which has a rating

of 2400A and costs €1056 each. The grid side filter costs for the different generators is shown in Table 4.7.

Table 4.7
Grid-side active filter costs

Generator	Energy ripple (J)	Series modules	Capacitors per module	Total cost
SCG T5,6	11,113	4	22	€75,000
SCG T8,9	9,028	4	18	€70,600
SCG T5,6 seg	11,113	4	15	€67,300
SCG T8,9 seg	9,028	4	12	€63,900
PDD 10MW	5,910	4	8	€59,500
PDD 10MW seg	5,910	4	8	€59,500
SCG T10	16,730	7	19	€125,000
SCG T11	19,176	7	21	€129,000
SCG T10 seg	16,730	6	21	€111,000
SCG T11 seg	19,176	6	25	€117,000
PDD 20MW	11,820	7	10	€108,000
PDD 20MW seg	11,820	7	10	€108,000

4.3.2 Semiconductor Costs

Thyristors are selected as in Deliverable D3.32, based on the rated DC-link current as shown in Table 4.1. As before, for the generator side of the SCG the low frequency means that the thyristor thermal inertia will not be sufficient to damp the pulsating loss from the AC waveform. Because of this, the rectifier thyristors are selected to have an average current rating greater than the rated DC-link current. For other applications, the average current is around a third of the DC-link current. The di/dt and dv/dt ratings determine the design of the thyristor snubber and the active filter coupling inductor. The thyristors considered in this study are listed in Table 4.8, in which the 6,000V thyristors are used for the inverter, as well as the rectifier for the non-segmented generators and 20MW segmented generators. The 2,000V thyristors are used for the rectifiers of the 10MW segmented generators.

Table 4.8
Thyristors used in the converter designs

Thyristor	Model	Voltage (V)	Av. Current (A)	di/dt limit (A/ μ s)	dv/dt limit (V/ μ s)	Mass (kg)	Cost
1	K1351VF600	6,000	1351	75	1,000	1.0	€580
2	K2359TC600	6,000	2359	200	1,000	1.7	€870
3	N1718NC200	2,000	1718	500	1,000	0.5	€145
4	N3533ZC220	2,200	3533	150	1,000	1.7	€458

The thyristor configurations and total costs are given in Table 4.9. Conventionally in load-commutated converters 6000V thyristors are used for around 2.2kV AC voltage, and higher AC voltages are achieved by use of series devices [4-5]. In addition, an extra series device is added for fault-tolerance purposes, as the thyristors are designed to fail in a short-circuit mode, bypassing the failed device. For the segmented generators, the segmented generator design with separate rectifiers allows tolerance to rectifier faults.

4.3.3 Passive Components Costs

Since the D3.32 deliverable report, revised generator parameters have become available, as well as the addition of segmented generators, which has means that the calculation of the DC-link inductor parameters can be refined. The grid filter inductor is eliminated, as the grid transformer, with a leakage inductance of around 0.1 P.U. provides sufficient filtering. Finally, the values for the

active filter coupling inductors are calculated, based on the di/dt limits for the thyristors, and RC snubbers designed for the thyristors to comply with their dv/dt limits. These also protect the generator and transformer from high dv/dt .

Table 4.9
Thyristor configurations for each generator

Generator	Rating	Rectifier thyristor	Series devices	Inverter thyristor	Series devices	Total cost
SCG	10MW	2	3	1	3	€26,100
SCG seg.	10MW	4	1	1	3	€21,432
PDD	10MW	1	3	1	3	€20,880
PDD seg	10MW	3	1	1	3	€13,920
SCG	20MW	2	5	1	5	€43,500
SCG seg.	20MW	2	1	1	4	€34,800
PDD	20MW	1	5	1	5	€34,800
PDD seg.	20MW	1	1	1	5	€31,320

DC-link inductances are calculated as in Deliverable D3.32, for a 10% peak to peak current ripple. As before, the inductance required to smooth the rectifier and inverter sides are calculated separately and added together, except for the superconducting generator where the inverter-side inductance is doubled. For the segmented generators, it is assumed that the segments have the same phase, although for the segmented PDD generator a significant reduction in inductance could be achieved if the segments are phase shifted. As the ripple from the rectifier in the SCG converters is transferred to the grid filter, all SCGs of a given rating and segmentation will have the same inductance.

The inductors are designed for a current density of $5A/mm^2$ at rated DC current, but a 50% margin is added for the saturation current, to prevent excessively high currents during transient events. Inductances and costs for the generators are shown in Table 4.10.

Table 4.10
DC-link inductor parameters and cost.

Generator	Rating	Current (A)	Inductance (mH)	Cost
SCG	10MW	2,300	2.48	€39,100
SCG Segmented	10MW	2,750	1.72	€39,100
PDD	10MW	2,860	4.73	€87,600
PDD Segmented	10MW	2,860	4.73	€87,600
SCG	20MW	2,300	4.95	€64,900
SCG Segmented	20MW	2,750	3.43	€64,900
PDD	20MW	2,630	8.84	€125,000
PDD Segmented	20MW	2,630	8.84	€125,000

Coupling inductors between the active filters and the thyristor bridges are necessary to limit the di/dt rate during thyristor commutation. In normal operation, the rectifier thyristors will be switched at a firing angle of zero, so the commutation voltage will be zero, but during grid voltage dips the firing angle will be changed, so the commutation voltage will be higher and a coupling inductor necessary. When a non-zero firing angle is used in the rectifier, and in the case of the inverter, the active filter can be controlled such that the voltage driving the commutation is limited to that of one voltage step of the active filter, which limits the required inductor size.

Inductors were designed to handle the maximum generator current without saturating, with a 50% margin, but conductor cross section area was selected based on the filter RMS current, which is around a quarter of the generator RMS current [4-3]. For the rectifier, the inductors were designed to limit the maximum di/dt to a tenth of the rated maximum for the thyristor. For the inverter, the smaller grid coupling inductance (provided by the transformer) and the lower di/dt rating of the thyristor meant that grid current distortion was significant around the inverter commutations. For this reason, a di/dt of a fifth of the limit was chosen. The coupling inductor

parameters and cost are shown in Table 4.11. RMS current is listed for the inductors, and for the segmented generator the cost is for four inductors on the generator side.

Table 4.11
Active filtering coupling inductors

Generator	Rating	Generator			Grid		
		Inductance (μH)	Current (A)	Cost	Inductance (μH)	Current (A)	Cost
SCG	10MW	27.5	437	€1,020	36.7	412	€1,150
SCG seg	10MW	46.7	523	€7,640	36.7	498	€1,480
PDD	10MW			n/a	36.7	515	€1,090
SCG	20MW	27.5	437	€930	36.7	412	€1,430
SCG seg	20MW	35.0	523	€6,020	36.7	498	€1,560
PDD	20MW			n/a	36.7	473	€1,350

R-C snubbers were designed for the thyristors to limit the dv/dt to a tenth of the maximum value for the thyristor, and each thyristor has its own snubber in order to achieve dynamic voltage balancing of the series devices. As well as during switch-off, the thyristors also experience high dv/dt during the switching of the active filter, which occurs far more often than the thyristor commutation. As the thyristors are connected in series in the inverter and rectifier for non-segmented generators, the overall dv/dt can be higher than the device dv/dt . Snubbers were designed to have a damping ratio of 1, and achieve the required dv/dt , but this is regarding the capacitor voltage. The thyristor voltage, being the sum of the resistor and capacitor voltage, will have a slight overshoot, but well within the ratings of the devices.

Snubber resistor and capacitor values are shown in Table 4.12, along with the dv/dt values per thyristor stack. For the generator side rectifiers of the PDD generator, the resistance and capacitance are calculated based on the generator inductance. Costs are not given as suitable resistors could not be found, and the capacitor cost was found to be in the region of a few euros, and therefore insignificant in relation to other components. The resistance and capacitance values are still important for calculating losses.

Table 4.12
Thyristor R-C snubber components

Generator	Rating	Generator			Grid		
		dv/dt ($\text{V}/\mu\text{s}$)	Resistance (Ω)	Capacitance (nF)	dv/dt ($\text{V}/\mu\text{s}$)	Resistance (Ω)	Capacitance (nF)
SCG	10MW	300	19.7	189	300	26.3	142
SCG seg	10MW	100	26.3	541	300	26.3	142
PDD	10MW	300	237	66.7	300	26.3	142
PDD seg	10MW	100	199	49.9	300	26.3	142
SCG	20MW	500	19.7	114	500	26.3	85.1
SCG seg	20MW	100	19.7	722	400	26.3	106
PDD	20MW	500	336	56.5	500	26.3	85.1
PDD seg	20MW	100	561	35.4	500	26.3	106

4.3.4 Cooling System Costs

As in Deliverable 3.32, a cooling system cost of €0.8 per watt of maximum losses was used, and the cooling system costs are shown in Table 4.13.

Table 4.13
Cooling system costs

Generator	Rating	Maximum Losses (W)	Cooling System Cost
SCG T5,6	10MW	145,000	€116,000
SCG T8,9	10MW	154,000	€123,000
SCG T5,6 seg	10MW	155,000	€124,000
SCG T8,9 seg	10MW	189,000	€152,000
PDD	20MW	208,000	€167,000
PDD seg	20MW	188,000	€151,000
SCG T10	20MW	245,000	€196,000
SCG T11	20MW	237,000	€190,000
SCG T10 seg	20MW	291,000	€233,000
SCG T11 seg	20MW	290,000	€232,000
PDD	20MW	304,000	€243,000
PDD seg	20MW	288,000	€231,000

4.3.5 Conclusions

Total costs are given in Table 4.14, in which the mechanical cost has been calculated as 40% of the component costs. For the superconducting generators, the segmented generators generally have a lower cost, due to the reduced cost for the generator-side active filter, although this is reduced at 20MW. For the PDD generators, segmentation only has a minor effect, and there is little cost benefit to the removal of the active filter at 10MW as the DC-link inductor is larger. At 20MW, the increased active filter costs for the segmented SCG mean that the benefits are increased.

Table 4.14
Total cost and cost breakdown

Generator	Rating	Gen Filter	Thyristors	DC Inductor	Grid Filter	Mechanical	Cooling	Total
SCG T5,6	10MW	€134,000	€26,100	€39,100	€75,000	€110,000	€116,000	€499,000
SCG T8,9	10MW	€99,300	€26,100	€39,100	€70,600	€94,000	€123,000	€452,000
SCG T5,6 seg	10MW	€52,100	€21,400	€39,100	€67,300	€72,000	€124,000	€376,000
SCG T8,9 seg	10MW	€41,400	€21,400	€39,100	€63,900	€66,000	€152,000	€384,000
PDD	10MW	0	€20,900	€87,600	€59,500	€67,000	€167,000	€402,000
PDD seg	10MW	0	€13,900	€87,600	€59,500	€64,000	€151,000	€376,000
SCG T10	20MW	€169,000	€43,500	€64,900	€126,000	€161,000	€196,000	€760,000
SCG T11	20MW	€216,000	€43,500	€64,900	€129,000	€181,000	€190,000	€824,000
SCG T10 seg	20MW	€131,000	€34,800	€64,900	€111,000	€137,000	€233,000	€711,000
SCG T11 seg	20MW	€172,000	€34,800	€64,900	€118,000	€156,000	€232,000	€777,000
PDD	20MW	0	€34,800	€125,000	€108,000	€107,000	€243,000	€619,000
PDD seg	20MW	0	€31,300	€125,000	€108,000	€106,000	€231,000	€601,000

4.4 Converter Size

Converter size and weight for the current-source designs were considered in depth in the D3.32 deliverable, and are updated based on changes to the converter components and the addition of the segmented generators.

All sizes are based around the need for the converter to fit into a cabinet 1200mm deep by 2450mm high, as used by the ABB PCS6000 medium voltage converter [4-6], with the cabinet length adjusted to fit the different components.

4.4.1 Active Filter

Modules used in the modular active filter are shown in Figure 4.4, with the Type 1 module used for the generator-side filter and the Type 2 for the grid-side. The capacitors have a diameter of 100mm and a height of 150mm, and an additional 20mm height is allowed for the electrical connections and mounting. Both modules can have either one or two stacked banks of capacitors, and the depth of the bank can be adjusted to achieve the required number of capacitors. Cabinet layouts are shown in Figure 4.5, where a clearance of 30mm is used between modules in the same phase, and 100mm between phases and between the modules and the cabinet walls.

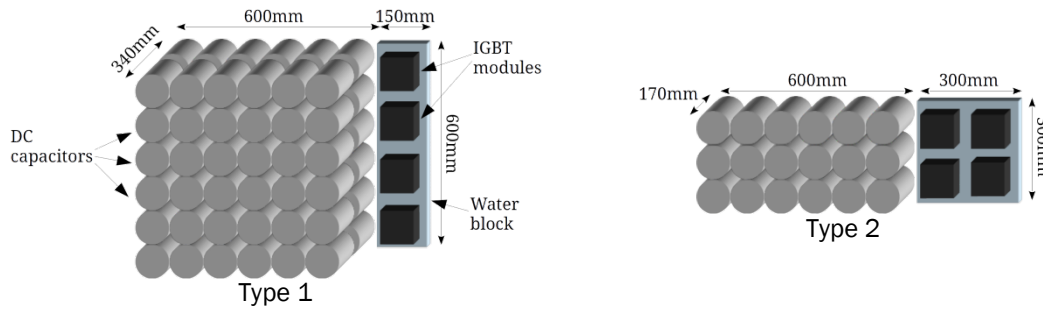


Figure 4.4 Modular active filter module layouts.

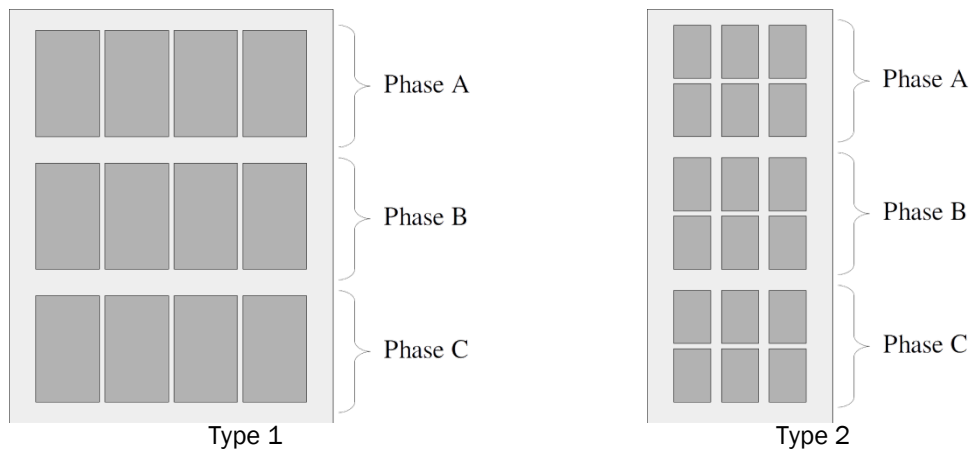


Figure 4.5 Modular active filter cabinet layouts.

Modules used in the segmented active filter are shown in Figure 4.6. The capacitor here has a diameter of 116mm and a height of 155mm, and an additional 25mm height is allowed for electrical connections. The 10MW converters use a vertical layout like the modular converters, and the width of the capacitor bank is adjusted depending on the capacitors required. The 20MW converter has a significantly higher capacitance requirement, as well as a larger number of switching devices, so capacitors are arranged into two banks, for the two DC links, and switching devices are arranged with one half-bridge of 8 devices per heatsink. Depth of the capacitor bank is 8 capacitors, while the width is either 3 or 4. Rather than being constructed as a module, which would be too heavy to handle within a turbine, parts such as the switching device assemblies and capacitor banks will be separately removable. Filters are arranged in the cabinets shown in Figure 4.7, where a clearance of 50mm between adjacent modules is used.

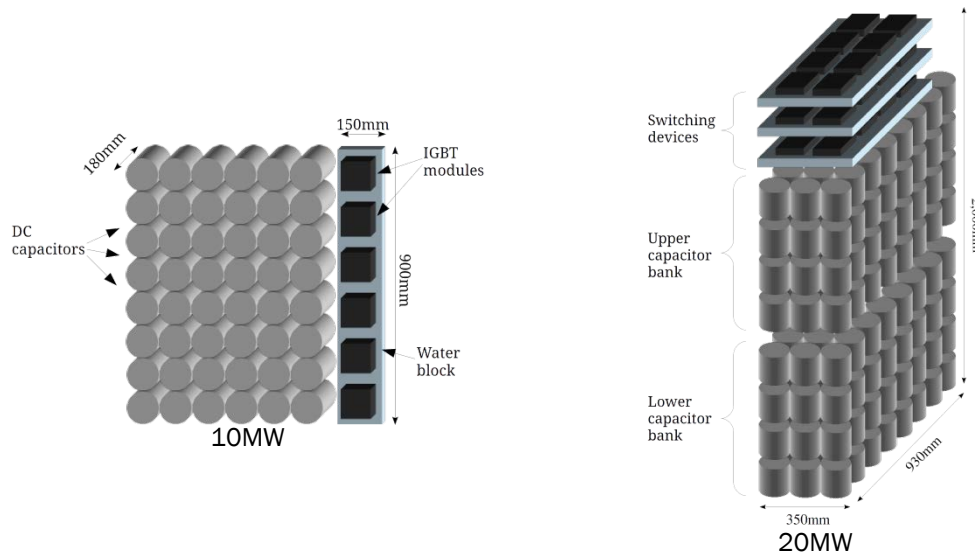


Figure 4.6 Segmented active filter module layouts.

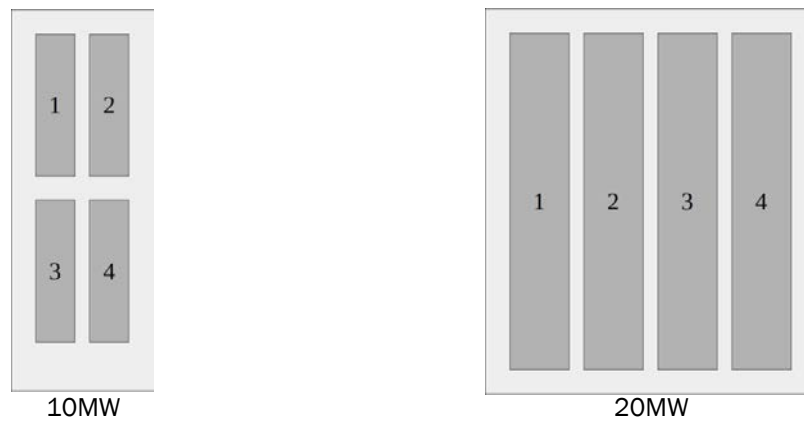


Figure 4.7 Segmented active filter cabinet layouts.

Generator and grid-side modular active filter configurations for the different generators are shown in Table 4.15 and 4.16, with segmented active filters in Table 4.17. The number of stacked capacitor banks (denoted Cap width in the tables) determines the width of the modules, and is selected to keep the module depth below 1,000mm, allowing the required 100mm clearance in the 1,200mm deep cabinets.

Table 4.15
Generator-side modular active filter configuration.

Generator	Modules	Capacitors	Cap width	Cap depth	Mod depth (mm)	Tot width (mm)
SCG T5,6	5	63	2	6	750	2,020
SCG T8,9	5	38	1	7	850	1,170
SCG T10	8	43	1	8	950	1,770
SCG T11	8	64	2	6	750	3,130

Table 4.16
Grid-side modular active filter configuration.

Generator	Modules	Capacitors	Cap width	Cap depth	Mod depth (mm)	Tot width (mm)
SCG T5,6	4	22	2	4	700	910
SCG T8,9	4	18	1	6	900	570
SCG T5,6 seg	4	15	1	5	800	570
SCG T8,9 seg	4	12	1	4	700	570

PDD 10	4	8	1	3	600	570
PDD 10 seg	4	8	1	3	600	570
SCG T10	7	19	1	7	1,000	970
SCG T11	7	21	1	7	1,000	970
SCG T10 seg	6	21	1	7	1,000	770
SCG T11 seg	6	25	2	5	800	1,280
PDD 20	7	10	1	5	700	970
PDD 20 seg	7	10	1	5	700	970

Table 4.17
Generator-side segmented active filter configuration

Generator	Capacitors	Mod depth (mm)	Mod width (mm)	Tot width (mm)
SCG T5,6	54	960	180	610
SCG T8,9	32	614	180	610
SCG T10	170	930	350	1,750
SCG T11	250	930	465	2,260

4.4.2 Main converter switching devices

The main switching devices are arranged in a water-cooled stack layout, similar to that used in commercial line-commutated converters as shown in Figure 4.8 [4-7], in which the thyristors are sandwiched between water blocks. Based on the converter shown in Figure 4.8, a stack height of 18 devices can be achieved, and a width of around 700mm is allowed per stack including gate drivers and snubbers.

The number of devices in the inverter and rectifier can be calculated from the data in Table 4.8, and is given in Table 4.18. A maximum of 18 devices per stack is used, and separate stacks are used for the rectifier and inverter. Width is calculated based on 700mm per stack.



Figure 4.8 ABB Megadrive LCI showing water-cooled thyristor stacks [4-7].

Table 4.18
Converter thyristor stack configuration.

Generator	Rating	Devices		Stacks	Width (mm)
		Inverter	Rectifier		
Non-segmented	10MW	18	18	2	1,400
Segmented	10MW	24	18	3	2,100
Non-segmented	20MW	30	30	4	2,800
Segmented	20MW	24	30	4	2,800

4.4.3 DC-link inductors

Sizes for the DC-link inductors are shown in Table 4.19. In all cases, the width of the inductor is less than the depth of the cabinet, so the inductors are placed in the cabinet lengthwise, and the width of the cabinet is determined by the depth of the inductor. Cabinet width is determined by allowing approximately 100mm on each side of the inductor, but this is less critical as the inductor is electrically insulated, so the cabinet width is rounded to one of two values. The coupling inductors for the active filters are relatively small, and it is expected that they could be fitted behind the thyristor stacks or in the terminal cabinets – they are likely to be relatively rugged so easy access for maintenance is not necessary.

Table 4.19
DC-link inductor sizes

Generator	Rating	Width (mm)	Depth, height (mm)	Cabinet width (mm)
SCG	10MW	868	760	960
PDD	10MW	1,136	994	1,300
SCG	20MW	1,028	900	1,100
PDD	20MW	1,280	1,120	1,500

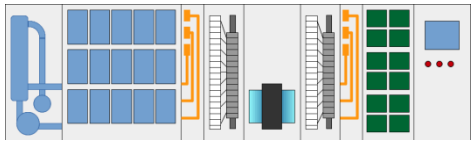
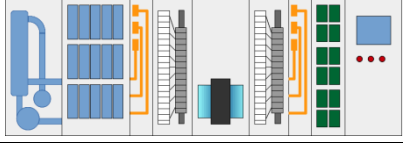
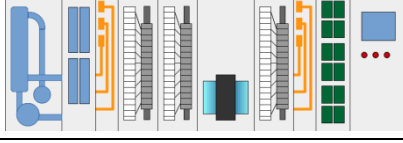
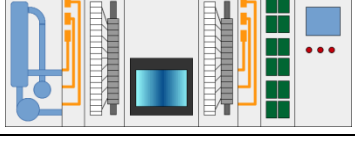
4.4.4 Cooling and other ancillary systems

Based on Figure 4.8, the cooling system, which is the leftmost cabinet, has a width of approximately 1,000mm, so this will be used for the 10MW converters, with two units used for 20MW. The cooling system consists of a water-water heat exchanger, to cool the non-conducting fluid used for the thyristor stacks with bulk cooling water from the turbine, as well as pumps and valves. Additionally a further 1,000mm is allowed for the control cabinet, and two 400mm-wide terminal cabinets are used per converter for the grid and generator terminals.

4.4.5 Overall size

Overall size for the converters is given in Table 4.20, and the key for the converter diagrams is in Figure 4.9.

Table 4.20
Converter size comparison

Generator	Converter	Width (mm)
SCG T5,6 10MW Non-segmented		8,090
SCG T8,9 10MW Non-segmented		6,900
SCG T5,6,8,9 10MW Segmented		7,040
PDD 10MW Non-segmented		6,070

PDD 10MW Segmented		6,770
SCG T10 20MW Non-segmented		10,440
SCG T11 20MW Non-segmented		11,800
SCG T10 20MW Segmented		10,220
SCG T11 20MW Segmented		11,240
PDD 20MW		9,070

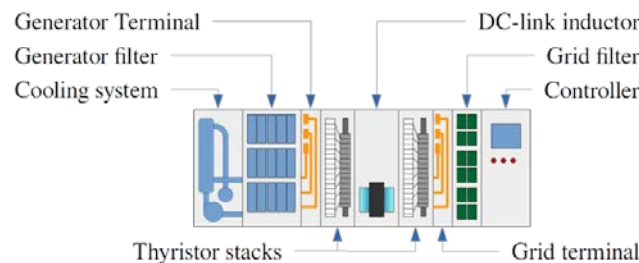


Figure 4.9 Key for converter size comparison

4.5 Converter Weight

Active filter masses are given in Tables 4.21, 4.22 and 4.23, and are obtained by adding up the masses of the individual components. For the cascaded active filters used with the non-segmented generators and on the grid side, the IGBT has a mass of 1.3 kg, and the capacitor 1.5kg, and the water block 2kg. For the segmented generator active filters, the same IGBT mass is used, with the clamping diodes having a mass of 340g. The capacitor has a mass of 2kg, while the water block is 500g per device.

Table 4.21
Generator-side active filter mass for non-segmented generators

Generator	Modules per phase	Capacitors per module	Module mass (kg)	Total mass (kg)
SCG T5,6	5	63	101.7	1,530
SCG T8,9	5	38	64.2	963
SCG T10	8	43	71.7	1,720
SCG T11	8	64	103.2	2,480

Table 4.22
Grid-side active filter mass

Generator	Modules per phase	Capacitors per module	Module mass (kg)	Total mass (kg)
SCG T5,6	4	22	40.2	482
SCG T8,9	4	18	34.2	410
SCG T5,6 Seg	4	15	29.7	356
SCG T8,9 Seg	4	12	25.2	302
PDD 10	4	8	19.2	230
PDD 10 Seg	4	8	19.2	230
SCG T10	7	19	35.7	750
SCG T11	7	21	38.7	813
SCG T10 Seg	6	21	38.7	697
SCG T11 Seg	6	25	44.7	805
PDD 20	7	10	22.2	466
PDD 20 Seg	7	10	22.2	466

Table 4.23
Generator-side active filter mass for segmented generators

Generator	Modules	Capacitors per module	Module mass (kg)	Total mass (kg)
SCG T5,6	4	54	119	475
SCG T8,9	4	32	74.8	299
SCG T10	4	170	372	1,490
SCG T11	4	254	540	2,160

Main switching device mass is given in Table 4.24. For this calculation, the thyristor masses are given in Table 4.6, while a mass of 500g is assumed per water block. The overall mass is doubled to take account of the electrical busbars and clamping system, as well as the snubbers and gate drivers. This is likely to be an under-estimate.

Table 4.24
Main switching device mass

Generator	Rating	Device mass (kg)	Water block mass (kg)	Total mass (kg)
SCG	10MW	48.6	19	130
SCG Seg	10MW	58.8	22	162
PDD	10MW	36	19	116
PDD Seg	10MW	30	22	104
SCG	20MW	81	34	230
SCG Seg	20MW	64.8	28	186
PDD	20MW	60	34	188
PDD Seg	20MW	54	28	164

Inductor masses are given in Table 4.25 for the DC-link inductors and Table 4.26 for the active filter coupling inductors, and are obtained by adding the total iron and copper masses for the inductor designs.

Table 4.25
DC-link inductor mass

Generator	Rating	Inductor mass (kg)
SCG	10MW	2,390
PDD	10MW	5,360
SCG	20MW	3,980
PDD	20MW	7,670

Table 4.26
Filter coupling inductor mass

Generator	Rating	Generator-side			Grid-side Mass (kg)	Total mass (kg)
		Inductors	Mass (kg)	Total (kg)		
SCG	10MW	1	34.8	34.8	39.5	102
SCG Seg	10MW	4	67.4	270	51.1	363
PDD	10MW	0		0	38.5	92.7
SCG	20MW	1	32.3	32.3	50.7	98.3
SCG Seg	20MW	4	53.5	214	54.2	306
PDD	20MW	0		0	47.7	84.3

A commercially-available cabinet of height 2,000mm, width 800mm and depth 800mm has a mass of 137kg. This was multiplied up to the required 2,200mm height and 1,200mm depth, giving a mass of approximately 280kg per m length, which is rounded up to 300kg/m. This gives the cabinet masses shown in Table 4.27 for the different converters.

Table 4.27
Cabinet mass

Generator	Rating	Cabinet Length (mm)	Cabinet Mass (kg)
SCG T5,6	10MW	8,090	2,430
SCG T8,9	10MW	6,900	2,070
SCG Segmented	10MW	7,040	2,110
PDD	10MW	6,070	1,820
PDD Segmented	10MW	6,770	2,030
SCG T10	20MW	10,440	3,130
SCG T11	20MW	11,800	3,540
SCG T10 Segmented	20MW	10,220	3,070
SCG T11 Segmented	20MW	11,240	3,370
PDD	20MW	9,070	2,720

Overall mass is given in Table 4.28, and is generally dominated by the DC inductor and cabinets, with some of the generator-side active filters also having a significant mass. The mass of the cooling system is unknown, and is not included, but is likely to be significant. Despite not having a generator-side filter, the PDD converters have a higher mass than the SCG due to the larger inductors.

Table 4.28
Overall mass

Generator	Mass (kg)					
	Generator filter	Thyristors	DC Inductor	Grid Filter	Cabinets	Total
SCG T5,6	1,560	130	2,390	522	2,430	7,040
SCG T8,9	998	130	2,390	450	2,070	6,040
SCG T5,6 seg	745	162	2,390	408	2,110	5,820
SCG T8,9 seg	569	162	2,390	354	2,110	5,590
PDD 10MW	0	116	5,360	285	1,820	7,590
PDD 10MW seg	0	104	5,360	285	2,030	7,780
SCG T10	1,750	230	3,980	788	3,130	9,880
SCG T11	2,510	230	3,980	851	3,540	11,100
SCG T10 seg	1,700	186	3,980	747	3,070	9,680
SCG T11 seg	2,370	186	3,980	855	3,370	10,800
PDD 20MW	0	188	7,670	514	2,720	11,100
PDD 20MW seg	0	164	7,670	514	2,720	11,100

4.6 Efficiency, Energy capture and wind energy cost

Losses were calculated at different wind speeds between the cut-in and the rated wind speed using a Matlab script, using the standard methods. For the calculation, the DC voltages in the filters were assumed to be constant, as was the main converter DC current. The filter DC voltage will have a significant ripple at higher power levels, while the DC current ripple will be significant at lower power levels, which will affect the losses. It may also be necessary to keep the DC current above a minimum value in order to maintain a continuous current, which will increase losses at low wind speeds.

Snubber loss was calculated analytically, based on the current in the snubber resistors, and depends mainly on the filter switching. Because the filter switching amplitude is constant at all wind speeds, snubber loss will be constant. Total loss was less than 400W for the non-segmented SCG and the PDD, but around 5kW and 3.5kW for the 10 and 20MW segmented SCGs. This is due to the active filters having a high voltage ripple compared with the multilevel active filters in the non-segmented generators. Losses are slightly lower in the 20MW converter due to the use of a 3-level active filter. The overall loss could be reduced by reducing the active filter DC-link voltage at lower wind speeds, lowering the switching voltage magnitude and hence loss, but this was not implemented in the simulation.

Efficiencies for the different generators are shown against wind speed in Figure 4.10. For clarity, only one superconducting generator is considered for each power rating, with generator T5 used for 10MW and T10 for 20MW. In general, the segmented SCG converters have a lower efficiency than the non-segmented, but this is reversed for the PDD. The PDD has a greater efficiency at low wind speeds, but lower at high wind speeds. This can be explained by investigating the sources of the losses, which are shown in Figure 4.11 for the 10MW generators.

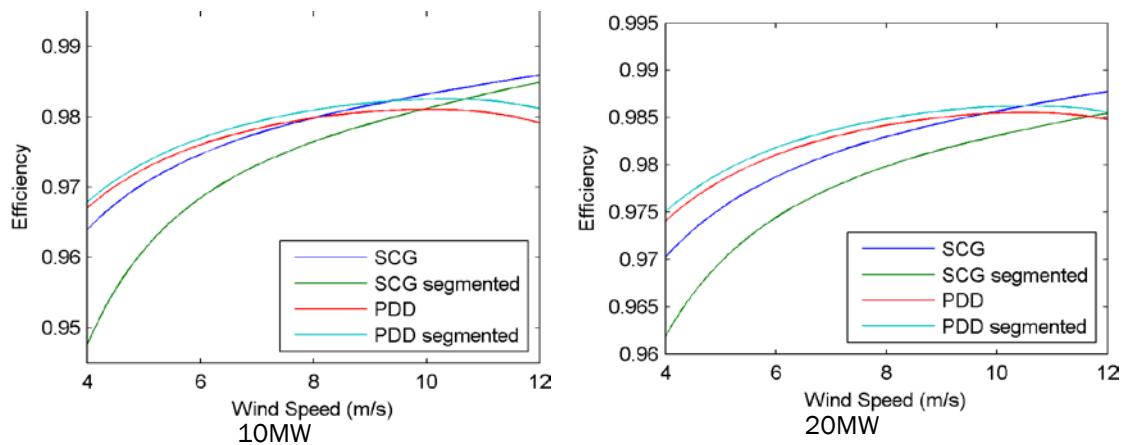


Figure 4.10 Converter efficiency comparison.

In all cases it can be seen that the main converter (including snubbers) and DC inductor losses increase with the wind speed, as both are related to the DC current, which is proportional to the generator current. For the SCG, the grid filter loss is around the largest proportion of losses at low wind speeds, as the inverter is operating at a large firing angle, which requires significant reactive power compensation. At high wind speeds the firing angle is lower, and less reactive power compensation is required so losses reduce. For the PDD, the higher commutation delay at higher wind speeds reduces the DC voltage, so the firing angle maintains a more constant value at higher wind speeds.

For the segmented SCG, the generator filter losses are lower than the non-segmented due to the reduced number of switching devices, but main converter losses are higher due to the higher current from the lower output voltage. Main converter losses are especially higher at low wind speeds due to the addition of the snubber loss. The segmented PDD has the same overall voltage as the non-segmented, so most losses are the same but main converter losses are lower for the segmented generator due to lower loss rectifier thyristors.

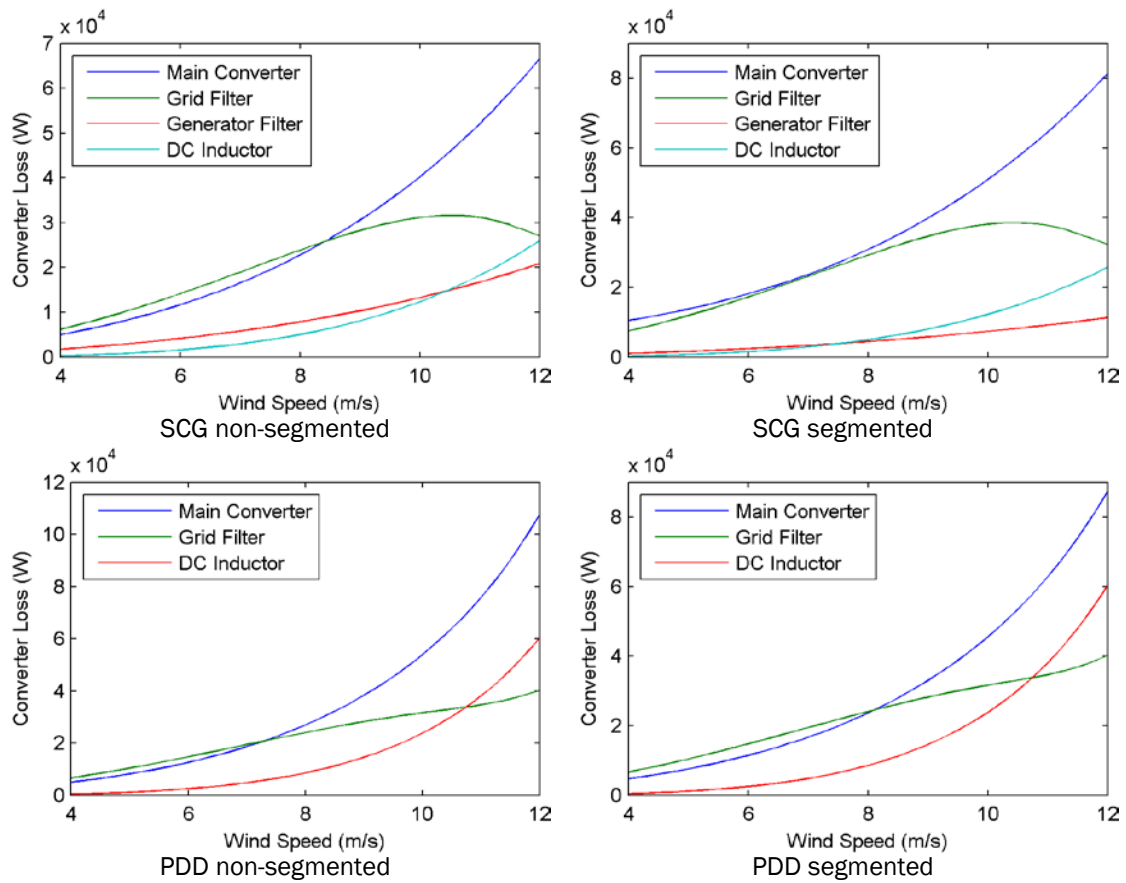


Figure 4.11 Breakdown of losses for 10MW converters.

The converter losses and the wind speed distribution can be used to calculate the annual energy, and this can be used with the converter cost to calculate the cost of energy attributed to the converter. This is calculated using the same method and wind distribution as the other converters. This is shown in Table 4.29, with the cost of energy broadly following the converter cost, due to the annual losses being similar for all converters and small in comparison with the total annual energy.

Table 4.29
Converter cost of energy

Generator	Rating	Converter Cost	Annual Cost	Annual Losses (MWh)	Annual Energy (MWh)	Cost of Energy (€/MWh)
SCG T5,6	10MW	€499,000	€20,000	745	47,688	€0.419
SCG T8,9	10MW	€452,000	€18,100	797	47,635	€0.380
SCG T5,6 seg	10MW	€376,000	€15,000	821	47,612	€0.316
SCG T8,9 seg	10MW	€384,000	€15,400	968	47,594	€0.323
PDD	10MW	€402,000	€16,100	996	47,436	€0.339
PDD seg	10MW	€376,000	€15,000	908	47,524	€0.317
SCG T10	20MW	€760,000	€30,400	1286	95,580	€0.318
SCG T11	20MW	€824,000	€33,000	1255	95,606	€0.345
SCG T10 seg	20MW	€711,000	€28,400	1527	95,335	€0.298
SCG T11 seg	20MW	€777,000	€31,700	1491	95,370	€0.326
PDD	20MW	€619,000	€24,700	1477	95,388	€0.259
PDD seg	20MW	€601,000	€24,000	1403	95,458	€0.252

4.7 Control Design

Control of the converters consists of control for normal operation and control during grid faults. There are also additional modifications to be made to the control system when the segmented generators are used. The main control modification for fault ride-through control is to use the active filter to assist the commutation of the thyristors, which is inhibited by drops in grid voltage. The active filter can also be used to force-commutate the thyristors, which is used in fault ride-through control. During normal operation, the active filter is controlled to limit the magnitude of voltage transitions experienced by the thyristors during commutation, preventing excessively high dv/dt , and this will be covered in the fault ride-through section.

4.7.1 Control for Normal Operation – SCG

The overall control structure for the SCG is shown in Figure 4.4. In order to minimise losses, the rectifier thyristors are operated with a conduction angle of zero degrees during normal operation, functioning as a passive rectifier, so the control of the rectifier firing angle is not shown in the diagram. As is conventional in wind turbine control, the converter is given a generator torque demand for the power-tracking or power-limiting region, which is used to determine the current demand I^* .

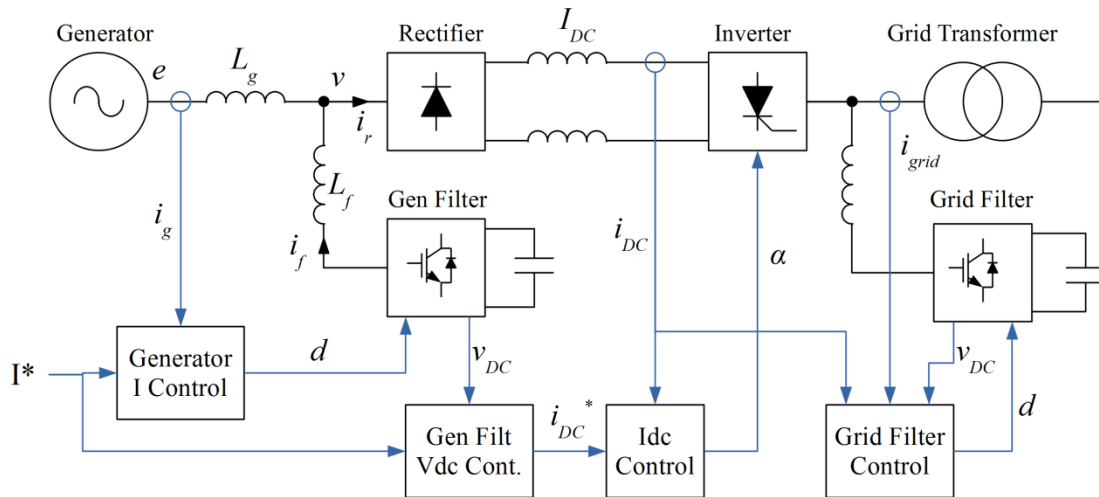


Fig.4.4 SCG control for normal operation

For a diode rectifier with a current-source DC link, the relationship between the fundamental frequency component of the rectifier current $I_{r,0}$ and the DC current I_{DC} is given by (4-2). If the active filter is not providing any reactive power then the generator current I_g is equal to $I_{r,0}$, and the active filter supplies the harmonics of the rectifier current. As the generator- and grid-side active filters are not connected, no real power can flow, so any mismatch between the power flowing from the generator and the power flowing into the rectifier will result in the active filter capacitor voltage either increasing or decreasing.

$$I_{r,0} = \frac{\sqrt{6}}{\pi} I_{DC} \quad (4-2)$$

The generator current is directly controlled by the active filter, and the DC-link current of the CSC controlled through the inverter firing angle to regulate the power balance between the main converter and generator-side filter according to (4-2), and hence the filter DC-link voltage. The grid filter is controlled to maintain a sinusoidal current, with the magnitude of the grid current controlled to regulate the grid filter DC-link voltage, with feedforward from the main converter DC-link current. Due to time constraints, regulation of the DC-link voltage of the grid-side active filter was not considered in detail or simulated.

The generator current controller is relatively simple, and is based on a calculation of the applied voltage to achieve the required current in the steady state, calculated in the rotating reference frame. This is combined with a proportional controller operating in the fixed reference frame, which speeds up changes in current demand and ensures the current path is properly diverted between the main converter and active filter during main converter commutations.

The structure of the current controller is shown in Fig.4.5, where the EMF angle and frequency θ, ω are either estimated from the generator applied voltage and resulting current, or calculated from an encoder. From the desired d- and q-axis currents i_d^*, i_q^* the feedforward voltage V_{ffd}, V_{ffq} is calculated using (4-3), where L and R are the generator inductance and resistance, and k is the EMF constant. The feedforward voltage is over-modulated using third harmonic injection.

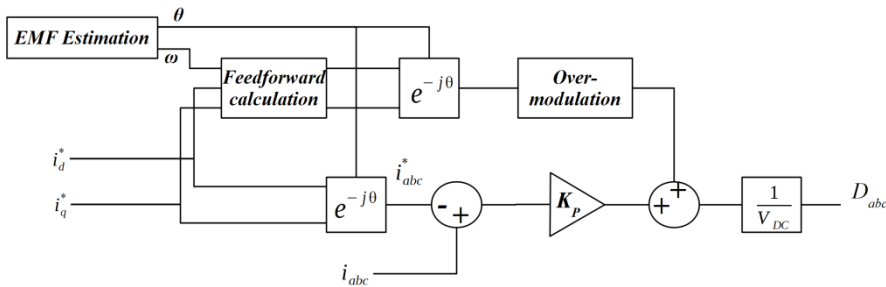


Fig.4.5 Generator current controller structure

$$\begin{bmatrix} V_{ffd} \\ V_{ffq} \end{bmatrix} = \begin{bmatrix} 0 \\ k\omega \end{bmatrix} + \begin{bmatrix} R & 0 \\ 0 & R \end{bmatrix} \begin{bmatrix} I_d^* \\ I_q^* \end{bmatrix} + \begin{bmatrix} 0 & -\omega L \\ \omega L & 0 \end{bmatrix} \begin{bmatrix} I_d^* \\ I_q^* \end{bmatrix} \quad (4-3)$$

Control of the DC-link current is as shown in Fig.4.6, which covers the determining of the desired inverter DC-side voltage v_D^* , used to set the inverter firing angle α based on the relationship given in (4-4). One aim of this controller is to regulate the low frequency ripple from the rectifier at 6 times the generator AC frequency, in order to minimise the size requirement for the DC-link inductor. In order to achieve this, the current is controlled by regulating the voltage drop across the inductor using a PI controller. The voltage from the rectifier side of the converter is estimated by subtracting the lowest generator line voltage from the highest and dividing by $\sqrt{3}$, which also acts to feed forward the rectifier ripple voltage. The ripple due to the grid-side inverter is filtered from the DC current signal using a moving average filter.

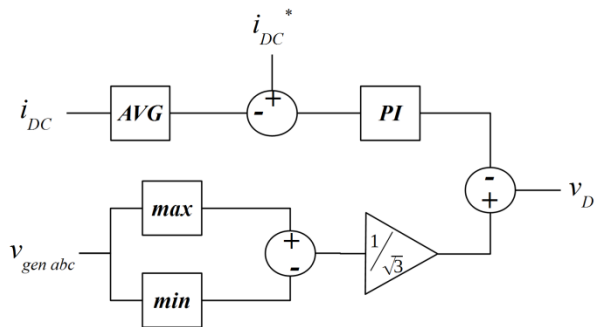


Fig.4.6 DC-link current controller structure for SCG

$$V_D = V_{LL} \frac{3\sqrt{2}}{\pi} \cos \alpha \quad (4-4)$$

Control of the DC-link voltage for the generator-side active filter has three aspects: control of the overall voltage, voltage balance between phase strings and voltage balance between modules in each phase string. The last of these is an established problem with well-documented solutions, and will not be considered here [4-8], [4-9].

Overall DC-link voltage control is shown in Fig.4.7. The DC voltages from the three phase strings are combined using an RMS average, as a conventional mean average will contain ripple at twice

the generator frequency if the cycle average DC voltage is not equal between phase strings. This combined DC voltage is filtered using a moving average filter at 6 times the generator frequency and used with a PI controller to set the DC-link current demand for the CSC. The generator current demand I_{gen}^* is used as a feedforward term.

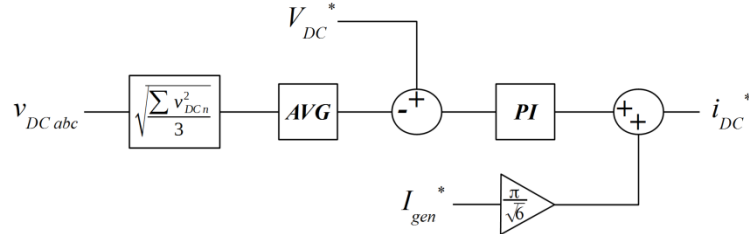


Fig.4.7 Active filter overall DC voltage control

Balancing of the DC voltage between phase strings is achieved by introducing an unbalance into the generator current demand, using the control structure in Fig.4.8. The three overall DC voltages of the phase strings, $v_{DC abc}$ are filtered using a moving average at twice the generator frequency, and converted to orthogonal currents $V_{DC \alpha, \beta}$, which are used with a proportional controller to set the value of a negative phase sequence current which is added to the current demand i_{abc}^* used in Fig.4.5. The fact that the moving average filter must be set at twice the generator frequency, while the one used in the control of the overall DC voltage is at six times the generator frequency, means that the DC voltage balancing must be slower than the overall DC voltage control. This has implications for the required filter DC capacitor size, as will be shown in the next section.

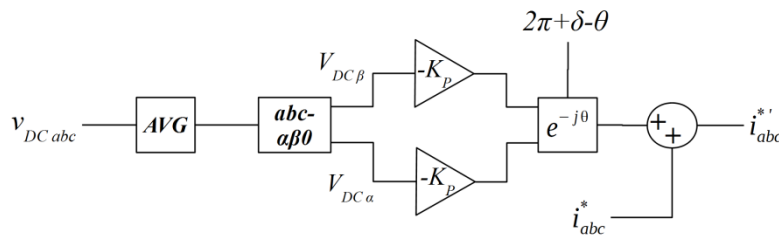


Fig.4.8 Active filter DC voltage balancing

In simulation, it was found that the higher speed of the generator current controller relative to the DC-link current controller caused problems with the filter DC-link voltage regulation. For this reason, the current demand input to the generator current was filtered using a first-order filter to equalise the response speeds.

A simpler method for the active filter control, similar to that used for stand-alone active filters [4-10], is to regulate the generator torque using the DC-link current, and use the generator current demand magnitude in Fig.4.5 to regulate the filter DC-link voltage. This method was not used as the chosen method gives a more direct and accurate control over generator torque, which was felt to be desirable for the chosen application.

The control parameters were tuned to give the best performance at rated power, where it is desirable to minimise any overshoots in filter DC-link voltage in order to limit the capacitor size requirements. As moving average filters are used extensively, these parameters will not be suitable at lower wind speeds where the generator frequency is lower, so the controller will need to switch between different parameter sets depending on the wind speed. At lower speeds, the turbine power will be lower and so the active filter DC voltage ripple lower, and the controller speed less critical.

Control of the grid-side active filter was not developed in detail due to time constraints, but is based around a current controller similar to that shown in Fig.4.5, with the current demands based on the generator power and grid voltage.

4.7.2 Control for Normal Operation – PDDG

For the PDD, the control system for normal operation is shown in Figure 4.9. Generator d-axis current demand, representing the generator torque, is controlled via the main converter DC-link current. Due to the significant commutation overlap from the generator reactance, the d-axis current will be related to the DC-link current and the generator voltage, so a PI controller is used to regulate the d-axis current. This reduces the torque control bandwidth significantly, but further work may allow relatively accurate feedforward values for the DC-link current to be estimated, improving the controller bandwidth.

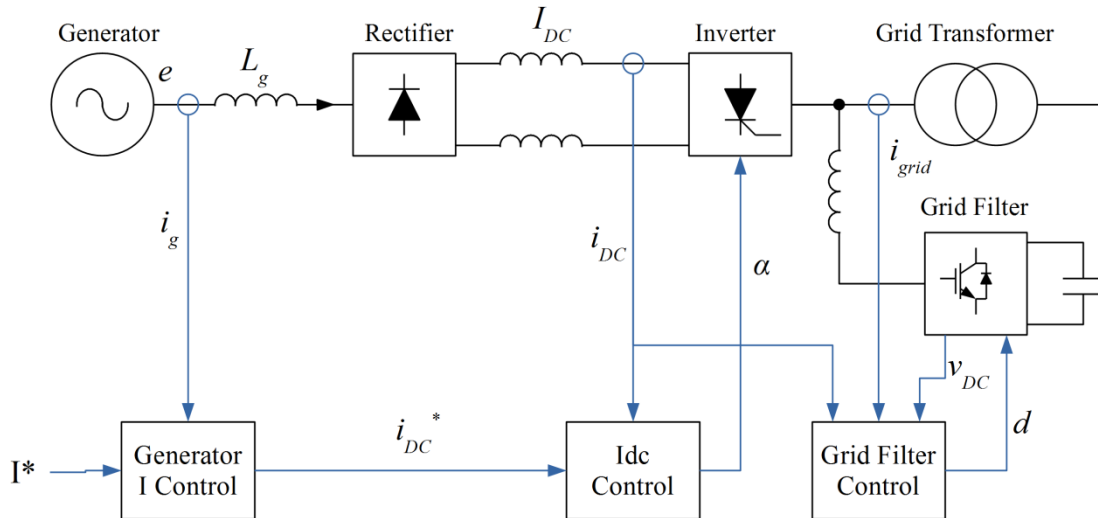


Figure 4.9 PDD control for normal operation

DC-link current control is similar to that used in the SCG, but in this application it is not necessary to regulate the DC current ripple caused by the rectifier. Because of this, the averaging filter is removed from the control system in Figure 4.6, and an average generator voltage is used as a feedforward term as opposed to a continuous estimation of the rectifier voltage ripple.

4.7.3 Fault Ride-Through Control

Control of the converter, particularly the SCG converter, during grid faults is a complex issue due to several aspects of the converter:

- The line-commutated converters used for the main power path require a strong grid in order for the thyristors to properly commute, which will be absent during a significant voltage dip.
- A significant voltage dip will require the rectifier to operate at a high firing angle, which will increase the DC-link current ripple significantly. For the SCG, the ripple cannot be controlled by the inverter as in normal operation, as it is already operating at minimum firing angle.
- The rectifier thyristors can only be naturally commutated within certain intervals, and with the low frequency of the SCG the time before the firing angle can be changed in the event of a grid fault may be significant. This could lead to a large DC-link over-current.

The last two problems could be solved by increasing the size of the DC-link inductor significantly, limiting the rate at which the current can change and the size of the current ripple. However this would significantly increase the converter cost as well as reduce the torque control bandwidth.

The proposed solution is to use the active filters to assist or force the commutation of the thyristors. The grid-side active filter can assist the commutation of the inverter thyristors, while the generator-side filter for the SCG converter can force-commutate the rectifier thyristors to allow instant switching.

The method of assisted commutation is explained using the diagram in Figure 4.10, which represents the commutation of the rectifier between devices 1 and 3, which represent the upper devices connected to phases A and B respectively. During commutation, the large DC-link inductance means that the DC current i_{DC} can be considered constant. The fact that the generator inductance is significantly larger than the filter inductance means that the generator currents i_{ga} , i_{gb} and i_{gc} can also be considered constant, with commutation occurring through the filter inductance. The active filter strings have voltages v_{fa} , v_{fb} and v_{fc} .

Just before the firing pulse is sent to thyristor 3, the voltage across both thyristors is ramped down to zero at time t_1 , at a rate determined by the previously calculated dv/dt . This is achieved using the active filter, by ramping v_{fa} and v_{fb} to the average of both values. To prevent filter switching during commutation, the nearest whole number of levels are activated and PWM switching is temporarily disabled.

After the switching pulse is sent to device 3 at time t_2 , and firing angle α , the voltage between points B and A, v_{BA} , will be zero, and v_{fb} will be raised above v_{fa} by an amount V_{comm} in order to commutate the current between the devices via the active filter and inductor L_f . V_{comm} is kept at one active filter voltage level, which ensures that commutation occurs even with a low generator or grid voltage while keeping the di/dt to the specified limit. This occurs for a specific time after the switching pulse, calculated to allow for commutation to fully occur, with the active filter returning to normal operation at time t_3 .

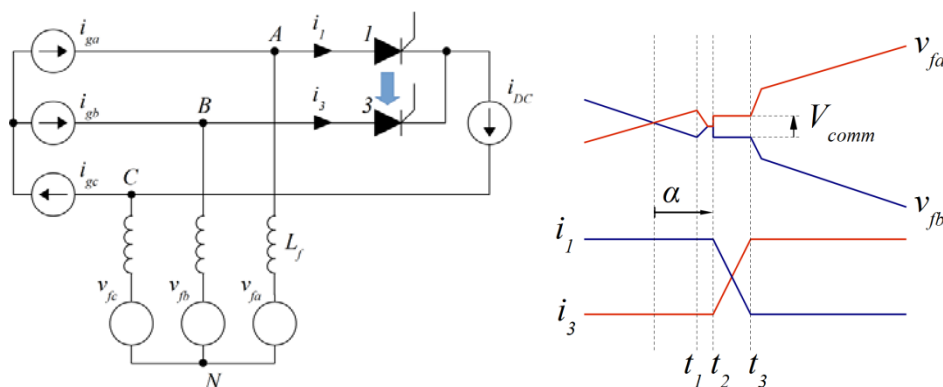


Figure 4.10 Rectifier commutation

This method also allows for force-commutation of the thyristors, allowing the firing angle to be changed instantaneously or the rectifier devices switched off altogether. Force commutation requires the negative voltage across the device which has switched off to be maintained for longer than the turn-off time t_q [4-11], which is around 1.5ms for the medium-voltage devices used in this study.

During severe voltage dips, which would require a large rectifier firing angle and the associated huge DC current ripple, it is proposed that the rectifier only be operated for brief pulses. The remaining time forced-commutation can be used to place it in a shoot-through state, with the top and bottom thyristors from a single phase activated, and the others blocking.

One aspect of grid fault ride-through control which has not been considered is the application of dump resistors. To protect the turbine structure it is desirable to avoid a rapid reduction in generator torque, which would occur when a grid voltage dip reduces the power which can be exported. Because of this, dump resistors are needed to absorb the excess power until the grid voltage can be restored or the turbine is allowed to disconnect and come to a gentle stop. One method of connecting a dump resistor might be to include an additional thyristor bridge connected

to the generator, as shown in Figure 4.11. This will increase the size and cost of the converter, but the increase will be small due to the thyristors making up a small part of the overall size and cost.

Additionally, control of the active filter DC-link voltage during a grid fault has also not been considered. If the generator is de-torqued, then the generator current must be reduced to zero, and the energy stored inductively in the generator coils will be passed into the active filter, causing the DC-link voltages to increase significantly. The use of a dump bridge as described in the previous paragraph will alleviate this problem, but if a dump bridge is not used then dump resistors will need to be included in the active filter modules.

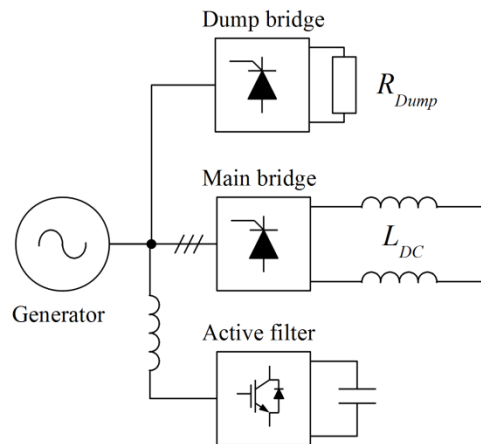


Figure 4.11 Generator dump resistor connection.

4.7.4 Series operation of converters for segmented generators

For the PDD, with each generator segment having the same voltage and each rectifier having the same DC-link current, power will naturally split evenly between segments. For the SCG, each segment has its own active filter which controls the generator current. If the generator current demands for the segments are identical, and the segments produce the same EMF, then power will be evenly split between segments.

An issue with adapting the non-segmented controller for the segmented SCG is that the main converter DC-link current is controlled to regulate the active filter DC-link voltage. As there are now four separate active filters each with their own DC-link, then it is not possible to regulate the separate DC-link voltages independently. One solution would be to have the overall generator torque demand control the main converter DC-link current, with the active filters regulating their own DC-link voltages through the individual segment current demands, but this reduces the directness of the torque control.

Instead it is proposed that the main converter DC-link current is controlled to regulate the average DC-link voltage of all four filters, with the segment torque demand for each filter modified depending on the deviation of that filter's DC-link voltage from the average. In this case, the sum of the torque demands for each segment will equal the overall torque demand, and in the steady state all segment torque demands will be equal.

4.8 Modelling and Simulation Studies

The converter for the 10MW non-segmented superconducting generator was simulated in Simulink. The segmented generator was also simulated, but found to be relatively similar in performance but without the issue of balancing the DC voltages of the different phase strings. All simulations were carried out based on rated wind speed, with a constant wind speed. For the generator-side filter, the filter capacitance is increased by a factor of three over the minimum in order to prevent instability due to issues of voltage balancing between phases. It will be shown in

this section that voltage balancing issues limit the controller bandwidth, which will either require a reduced control bandwidth or increased capacitor sizes.

Figure 4.14 shows the response of the converter to a generator torque demand, at 0.1s. Response speed is relatively fast, but a slight dip in the overall filter DC voltage is evident.

Figure 4.14 shows the overall filter DC voltage, but if this is decomposed into the voltages of the individual phase strings then the resulting response is shown in Figure 4.15, in which the inter-phase balancing is not activated. It is clear that the step response causes an unbalance in the DC voltage of the phase strings, with the final average voltage dependent on the trajectory of the DC voltage at the time of the current demand step.

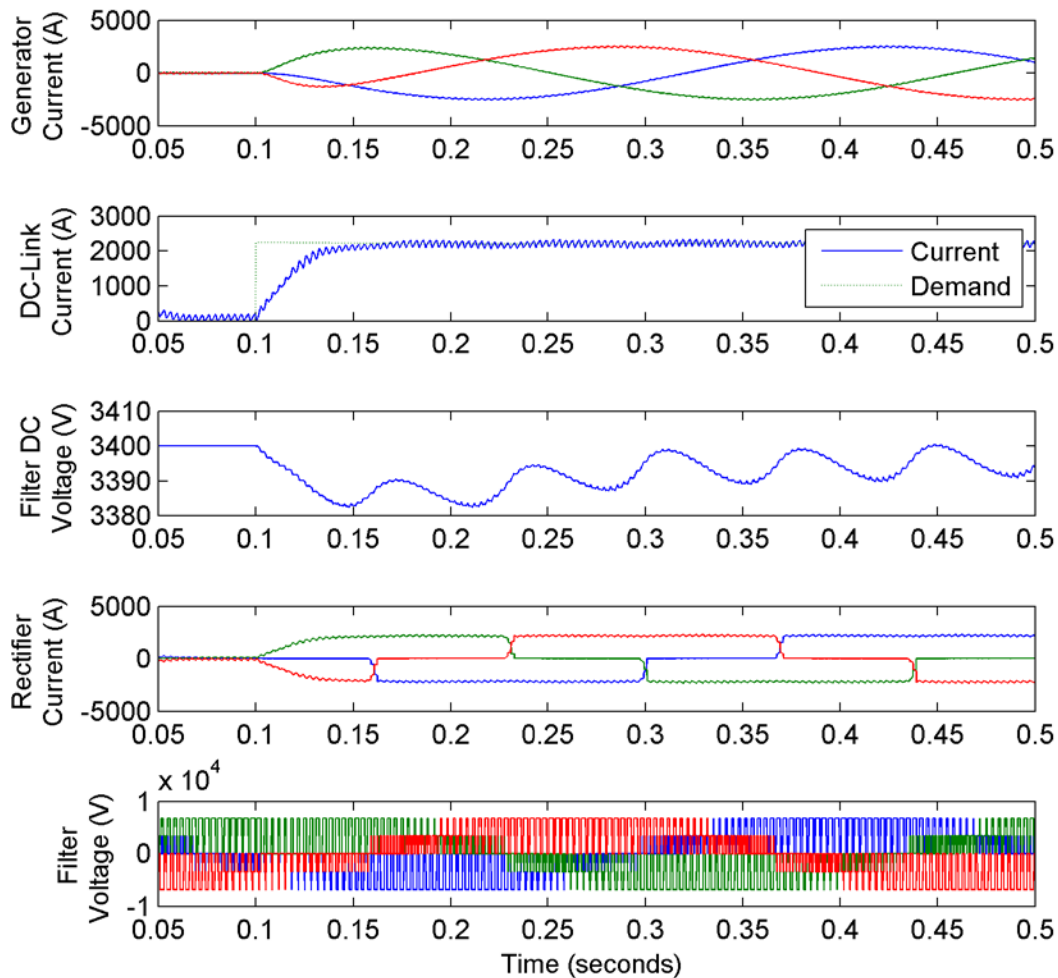


Figure 4.14 Generator torque step response.

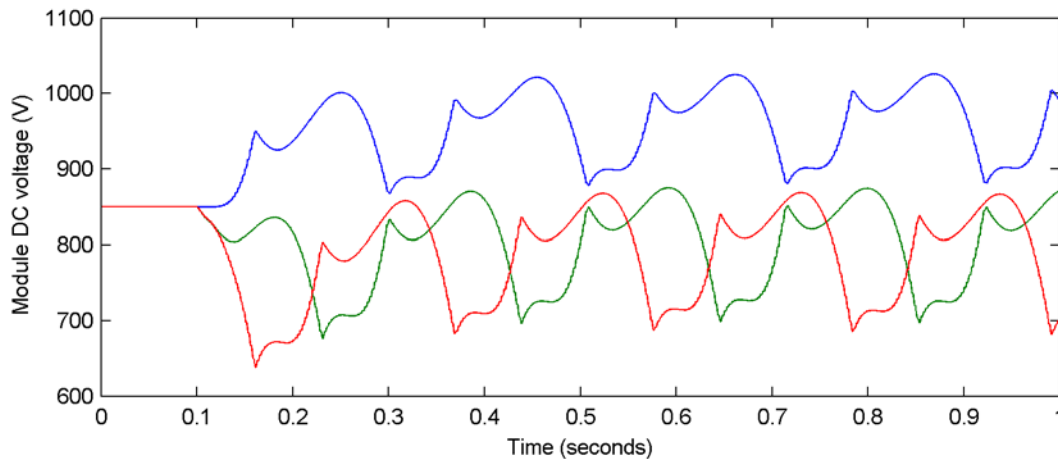


Figure 4.15 Generator active filter DC-link voltage for the three phase strings.

The DC voltage balance with the voltage balancing controller activated is shown in Figure 4.16, along with the generator current and torque. The balancing controller can be seen to eliminate the unbalance within 0.4s, which is a comparatively long time, and also causes a minor ripple to the generator torque while the unbalance exists. If the torque control bandwidth is severely reduced then inter-phase DC voltage balance can be maintained, but this may be undesirable in terms of the turbine control. Otherwise, the filter capacitance will need to be doubled to accommodate the overshoot, greatly increasing cost.

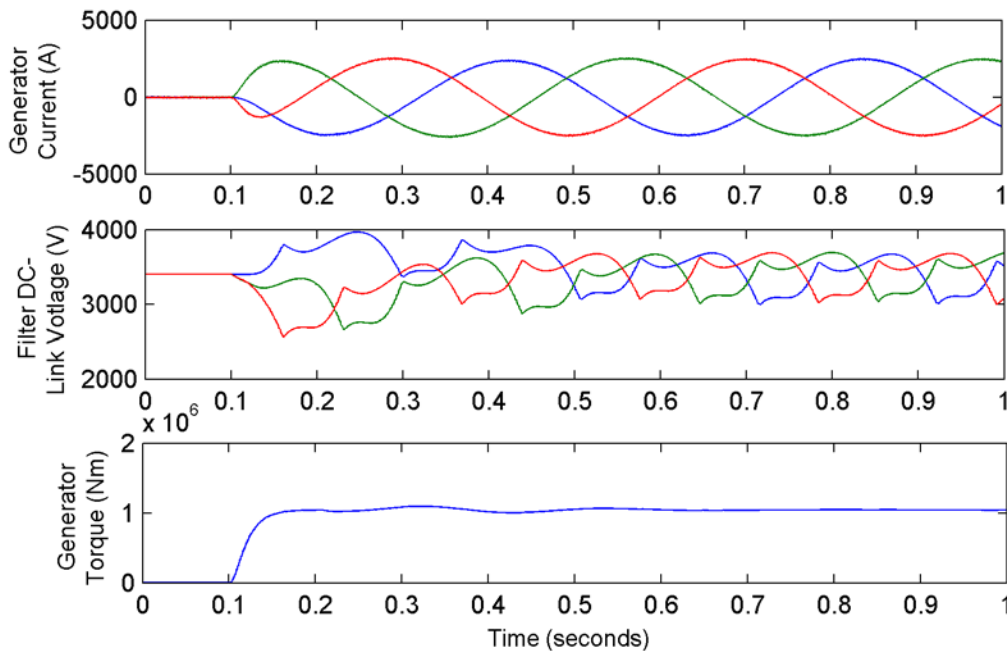


Figure 4.16 Generator active filter inter-phase DC voltage balancing.

Operation of the inverter side of the converter is shown in Figure 4.17, in which the grid impedance is assumed to be much smaller than the 0.1 P.U. leakage reactance of the grid transformer, and is therefore ignored. The operation of the commutation assistance system can be seen in the filter voltage, with the phase voltages briefly becoming equal around the time of the thyristor switching instants. Distortion in the grid current can be seen around the thyristor commutations. This is due to the relatively high inductance of the filter coupling inductor, despite it being around 10 times smaller than the main grid coupling inductance. The distortion could be reduced by increasing the switching frequency, allowing a higher controller gain, which would increase losses, or by choosing a thyristor with a higher di/dt rating, allowing a smaller filter coupling inductance but increasing cost.

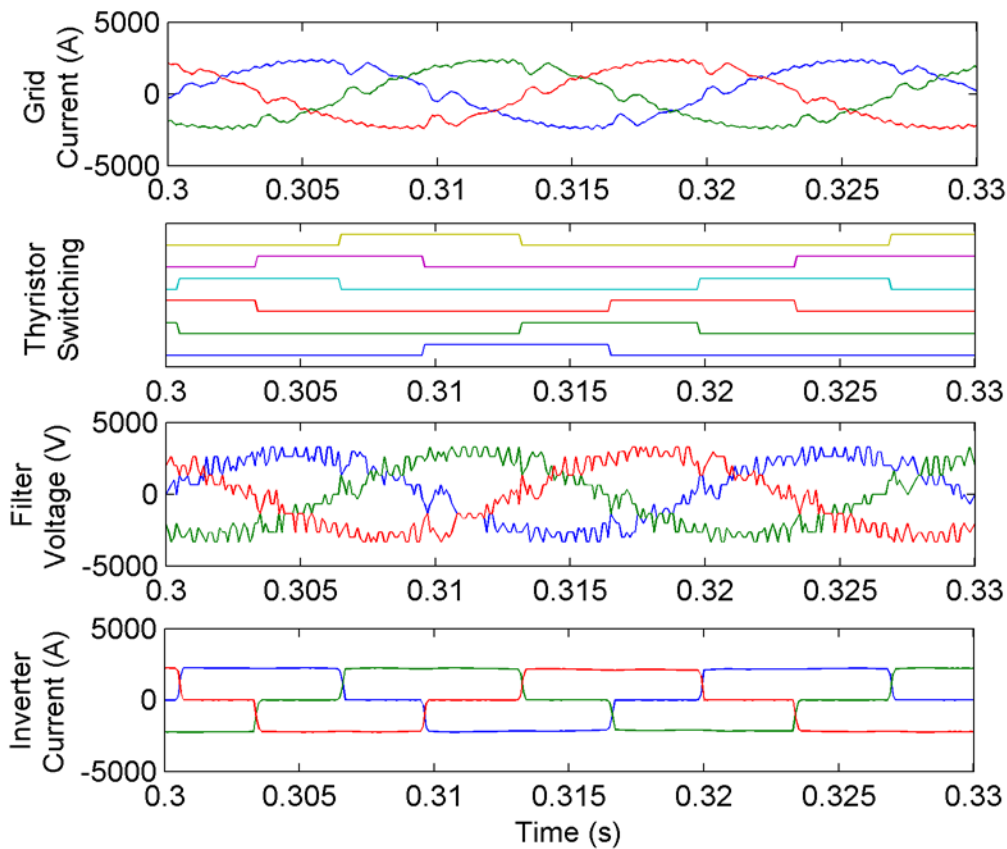


Figure 4.17 Inverter commutation in normal operation.

Response to a grid fault is shown in Figure 4.18. At 0.5s, the grid voltage is reduced to 10V, which triggers the converter to enter a fault ride-through mode. In this case, the rectifier thyristors are force-commutated so one phase leg is in a shoot-through state and the others are off, disconnecting the generator. The active filter forces the generator voltage to zero, and the DC-link current free-wheels, with a slow decrease. The grid-side active filter maintains the grid current, and assists commutating the inverter thyristors.

Not shown is the generator-side filter DC voltage, which increases significantly due to having to absorb the energy stored in the generator inductance. For this reason, dump resistors will be required even if it is not required to maintain the generator torque.

It is expected that at very low grid voltages, the rectifier will switch on for brief pulses in order to transfer energy into the DC inductor and maintain the current. For less significant voltage dips the rectifier may continue operating at a high firing angle.

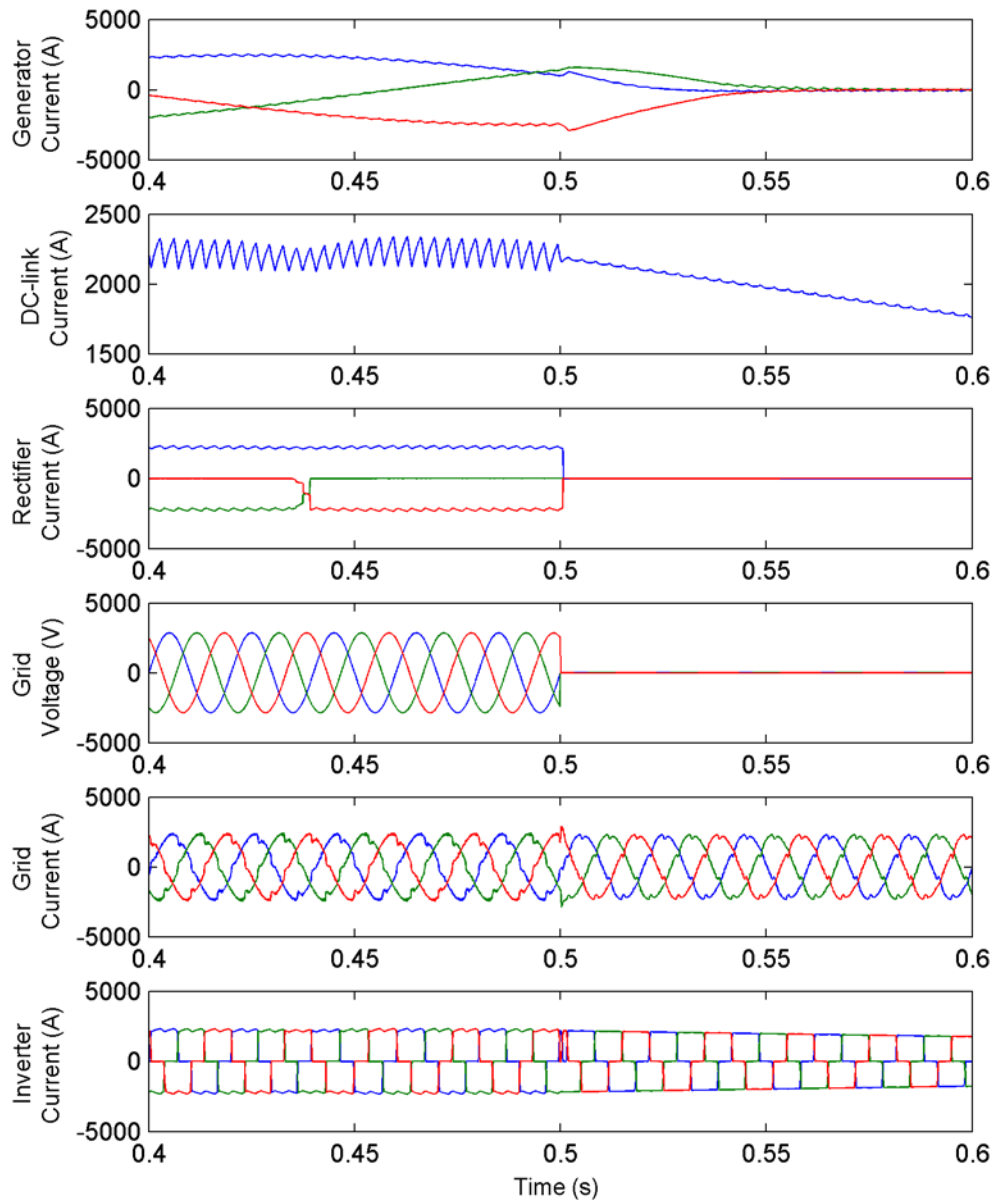


Figure 4.18 Response to grid fault.

The PDD generator converter was simulated on the generator side, with the rest of the converter represented using a current source. Generator current and torque are shown in Figure 4.19, with the significant commutation overlap evident in the generator current. The generator current waveform also leads to a significant torque ripple.

One method of reducing the torque ripple may be to phase shift the individual segments of the segmented generator, and if four segments are used then a phase shift of 15° between segments will offer the greatest reduction in torque ripple. Such a system would give the torque ripple shown in Figure 4.20, which shows a greatly reduced torque ripple compared with the ripple from the individual segments.

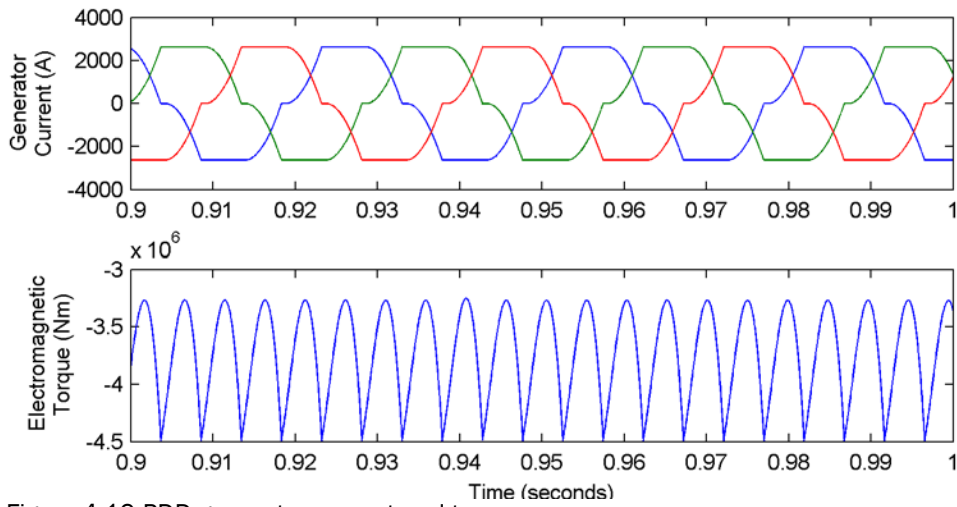


Figure 4.19 PDD generator current and torque.

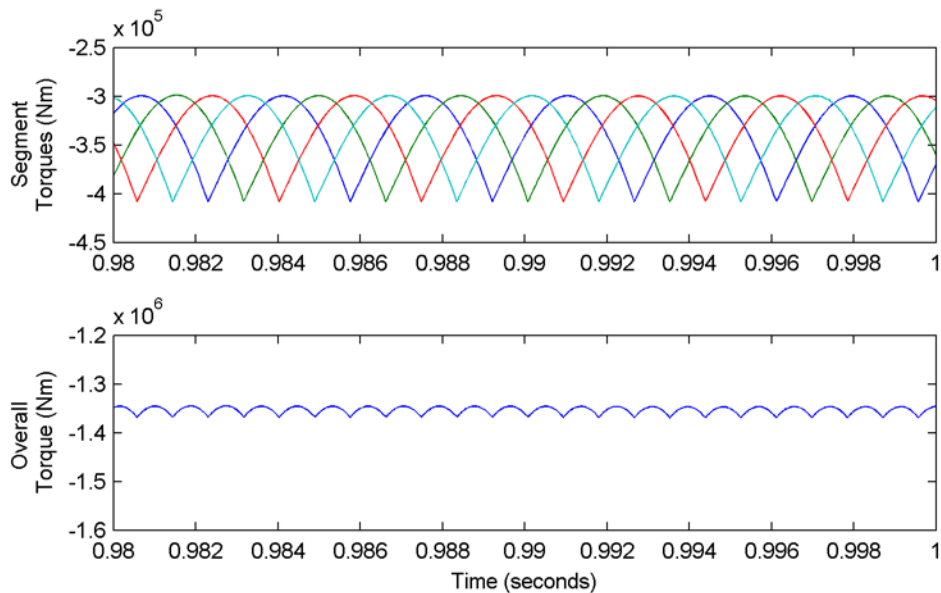


Figure 4.20 PDD multi-phase generator torque.

4.9 Discussion and Conclusions

Converters based on current-source topologies have been evaluated for use with superconducting and pseudo direct-drive generators. Voltage-source active filters are used to reduce grid-side current harmonics and ensure thyristor commutation during grid faults, and to provide a low current distortion to the superconducting generator.

Compared to Deliverable 3.32, converter designs are updated for the more recent generator parameters and segmented generators are added. Additionally the active filter is eliminated for the PDD generator, as the current distortion is considered not to be a problem. Finally, the coupling inductors for the active filters have been designed, based on the di/dt ratings of the thyristors, and thyristor snubbers designed based on the dv/dt limit.

The segmented SCG allows the use of more conventional 2- and 3-level active filters, compared with the cascaded active filter for the non-segmented generator, which reduces the DC capacitance requirement considerably, resulting in a significant cost reduction particularly at 10MW. However, losses in the generator-side thyristor snubbers are greatly increased, which is

significant at low wind speeds. Overall losses are also increased due to the higher currents from operating at a slightly lower voltage. For the 10MW SCG, segmentation also significantly reduces the physical size of the active filter, reducing the overall converter size and mass, although mass is largely dominated by the DC-link inductor. This is less significant for the 20MW generator, as the 3-level converter requires a significantly higher DC capacitance leading to a higher relative size, cost and mass.

Operating the PDD without an active filter results in a significant commutation overlap in the rectifier, due to the inductance of the generator, which has the effect of reducing the generator terminal voltage and increasing the current. This raises the losses in the converter, and will also increase losses in the generator, which was not considered in this study. Due to the relatively high frequency of the PDD generator, an active filter would not be particularly large or expensive, and the cost may be worthwhile to increase efficiency. Another option may be to use a smaller active filter which only operates to assist commutation. Finally, if the generator reactance can be reduced with minimal additional expense, then this would significantly increase the generator and converter efficiency.

Another consequence of operating the PDD without an active filter is that the current distortion results in a significant generator torque pulsation, which may be an issue for the turbine structure. Phase shifting the segments of the segmented generator can significantly reduce this pulsation. It has also been suggested that the PDD produces a trapezoidal EMF, which would result in lower torque pulsation, but simulation of a generator with trapezoidal EMF showed that the rectifier would not commute, so the generator reactance would need to be reduced.

Control of the converter has been simulated at rated wind speed. A particular issue for the non-segmented SCG is in maintaining the balance of DC-link voltage between the three phase strings of the generator-side active filter. By nature, the control system is slow, and a sudden step change in generator current demand will result in a significant unbalance in DC voltage. This means that either the DC-link capacitance must be increased, significantly increasing cost, or large and rapid torque increases must be avoided, although these are undesirable in any case.

Control of the SCG converter during severe voltage dips has also been simulated. In this case, the generator-side active filter is used to force commute the rectifier thyristors, allowing instant switching outside of the normal commutation window, while the grid-side active filter assists in commutation of the inverter thyristors. This addresses most of the problems associated with using current-source converters in renewable energy applications. A limitation in the grid fault operation presented here is that it has only considered a severe voltage dip, and has not considered operation when the voltage dip is less significant.

In all converter designs here the converter is designed to be fault tolerant. An extra thyristor is added to each stack of the inverter and in the rectifier of the non-segmented generators in order to provide redundancy, while failure of individual rectifiers in the segmented system are tolerated. The modular active filters are capable of fault-tolerance, with extra modules added to the grid-side active filter. On the rectifier side, module faults will reduce the maximum voltage output, limiting the turbine speed, although the exact response of the converter to module faults has not been simulated [4-12], [4-4].

A major uncertainty is related to current control of the main current-source converter, particularly during less severe voltage dips and at lower wind speeds when the average current is lower and the inverter firing angle is higher. At these points, the DC current ripple will be higher while the average current is lower, and at low wind speeds it may be necessary to increase the rectifier firing angle to increase the DC current, which would increase all losses. Alternatively it may be necessary to increase the size of the DC inductor, increasing the cost, although the inductor designs presented in this report may not be representative of a real-world inductor, so the existing costs may not be accurate. It should be noted that due to the active filters a low DC current ripple is not strictly necessary, although a higher ripple will lead to higher losses due to the higher peak current.

4.10 References

- [4-1] Z. Chen, E. Spooner, "Grid interface options for variable-speed permanent-magnet generators," IEE Proc. Electr. Power Appl., Vol. 145 (4), 1998.
- [4-2] R. Poore, T. Lettenmaier, "Alternative Design Study Report: WindPACT Advanced Wind Turbine Drive Train Designs Study," National Renewable Energy Laboratory (NREL), 2002.
- [4-3] A. M. Trzynadlowski, F. Blaabjerg, J. K. Pedersen, and N. Patriciu, "The tandem inverter: Combining the advantages of voltage-source and current-source inverters," in Thirteenth Annual Applied Power Electronics Conference, APEC, 1998.
- [4-4] B. Wu, "High Power Converters and AC Drives," Wiley-Blackwell, 2006.
- [4-5] ABB PCS6000 Wind data sheet, found at: <http://www.abb.co.uk/product/seitp322/8cb6b0fde98c9ca6c1256dfa002bcda9.aspx>
- [4-6] ABB Megadrive LCI datasheet, found at: <http://new.abb.com/drives/medium-voltage-ac-drives/megadrive-lci>
- [4-7] H. Sepahvand, J. Liao, and M. Ferdowsi, "Investigation on capacitor voltage regulation in cascaded H-bridge multilevel converters with fundamental frequency switching," IEEE Trans. Ind. Electron., vol. 58, no. 11, Nov. 2011.
- [4-8] L. Tarisciotti, P. Zanchetta, A. Watson, S. Bifaretti, J. C. Clare, and P. W. Wheeler, "Active DC voltage balancing PWM technique for high-power cascaded multilevel converters," IEEE Trans. Ind. Electron., vol. 61, no. 11, pp. 6157–6167, Nov. 2014.
- [4-9] F. Peng, "Application Issues of Active Power Filters," IEEE Industry Applications Magazine, 1998.
- [4-10] N. Mohan, T. Undeland, W. Robbins, "Power Electronics: Converters, Applications and Design," John Wiley & Sons, Inc., 2003.
- [4-11] M. A. Parker, C. H. Ng, and L. Ran, "Fault tolerant control for a modular generator-converter scheme for direct-drive wind turbines," IEEE Trans. Ind. Electron., vol. 58, no. 1, pp. 305–315, 2011.
- [4-12] P. Lezana, J. Pou, T. A. Meynard, J. P. Rodriguez, S. Ceballos, and F. Richardeau, "Survey on fault operation on multilevel inverters," IEEE Trans. Ind. Electron., vol. 57, no. 7, pp. 2207–2218, Jul. 2010.

5 CONCLUSIONS

In this report, the power converters are designed for the 10 and 20 MW wind turbines based on the SCG and PDD concepts, where the unsegmented and the segmented SC and PDD generators are both considered. The Chapter 2 designs the power converter based on VSC for the wind turbine tailed for SC generator. The Chapter 3 designs the power converter based on VSC for the wind turbine tailed for PDD generator. The Chapter 4 designs the power converter based on CSI for the wind turbine tailed for SC and PDD generators. In this report, the passive components and the active components for the power converters are designed and the total cost for the power converters are investigated. In addition, the size and the weight of the power converters are assessed. The efficiency, energy capacitor and wind energy cost contributed by power electronic system is also investigated. Finally, the control systems for the power converters are designed and the simulations have been performed for both normal operation and for ride-through grid faults Table 5-1 lists the cost, size, weight, and CoE of the designed power converters in this report.

Table 5-1
Comparison of the designed power converters

Power Converter	Gen.	Power (MW)	Seg.	Gen. type	Total cost (k€)	Size (m ³)	Weight (kg)	AEP (MWh)	CoE (€/MWh)	
VSC	SCG	10	non-seg.	T8	841.9	30.4	10710	47588	0.71	
			Seg.	T8	861.1	46.4	19308	47423	0.73	
		20	non-seg.	T10	1508.7	34.3	12822	95171	0.63	
			Seg.	T10	1595	60.8	21420	95018	0.67	
	PDDG	10	non-seg.			859	26.69	8550	47020	0.731
		20	Seg.			1823	59.37	17100	93799	0.777
CSI	SCG	10	non-seg.	T5,6	499	23.8	7040	47,668	0.419	
				T8,9	452	20.3	6040	47,635	0.380	
			Seg.	T5,6	376	20.7	5820	47,611	0.316	
				T8,9	384	20.7	5590	47,464	0.323	
		20	non-seg.	T10	760	30.7	9880	95,580	0.318	
				T11	824	34.7	11100	95,607	0.345	
			Seg.	T10	711	30.0	9680	95,335	0.298	
				T11	777	33.0	10800	95,370	0.326	
	PDDG	10	non-seg.			402	17.8	7590	47,436	0.339
			Seg.			376	19.9	7780	47,524	0.317
		20	non-seg.			619	26.7	11100	95,388	0.259
			Seg.			601	26.7	11100	95,458	0.252

The current-source converters have a considerably lower cost than the equivalent voltage-source converters, which is similar to the findings in the WindPACT study in the US [4-11]. Compared with the load-commutated converters in that study, the converters under consideration here add active filters on the grid side of the converter, and the generator side for the superconducting generator. This is necessary in order to comply with regulations on grid harmonics and grid fault ride-through, as well as limiting harmonics in the superconducting generator. The additional cost for the active filter is somewhat compensated by the reduction in passive filtering and reactive power compensation components.

The voltage-source converters considered in this study have a considerable cost for the passive filtering components, which is not required with the tandem converter as the multilevel active filter leads to a low current ripple using just the generator and transformer inductances, leading to a significant cost saving on passive components.

However, the tandem converter has a significant uncertainty, as it is there has been relatively little research on its design and control, with the converter control in particular being complex due to the use of two parallel converters. This, however, could be solved with further research and development.

The cost of CSI option may be significantly influenced by the rating of active filters which are voltage source converters. If the active filters are required to support the operation of thyristor converters during a grid fault, such as fault ride through, significant larger current ratings would be necessary than that required for only harmonic compensation. Further investigations are needed to determine the required rating of the active filters and the cost, as well as the operation and control strategies under both normal situation and disturbance conditions.

A more significant problem is that while the tandem converter may be suitable for 10 and 20MW wind turbines, such devices will represent a small part of the wind turbine market and the power electronics market as a whole. Hence a converter dedicated to this application will have a low production volume, and be expensive by its novelty. The increased flexibility of the 3-level NPC converter, and its use in multiple multi-MW industrial applications, means that in reality this converter design may be cheaper overall due to increased production volumes.